

# RCA REVIEW

*a technical journal*

Published quarterly by

RCA LABORATORIES

*in cooperation with all subsidiaries and divisions of*

RADIO CORPORATION OF AMERICA

---

VOLUME XXV

JUNE 1964

NUMBER 2

---

## CONTENTS

	PAGE
Preparation, Optical Properties, and Band Structure of Boron Monophosphide .....	159
C. C. WANG, M. CARDONA, AND A. G. FISCHER	
Free-Space Microwave Techniques for Plasma Measurements .....	168
M. P. BACHYNSKI AND G. G. CLOUTIER	
A Photoconductive Thermoplastic Recording System .....	200
N. E. WOLFF	
A New Surface Phenomenon in Thermoplastic Layers and Its Use in Recording Information .....	209
F. H. NICOLL	
The NASA Relay I Experimental Communication Satellite .....	232
J. D. KIESLING	
Analysis of Gate-Controlled Space-Charge-Limited Emission Processes in Semiconductors .....	262
R. C. WILLIAMS	
Stable Divalent Rare Earths in Alkaline Earth Halides by Solid-State Electrolysis .....	303
F. K. FONG	
Wide-Temperature-Range Ferrite Cores for Computer Memories ....	308
H. P. LEMAIRE, H. LESSOFF, AND E. FORTIN	
CORRECTION .....	319
RCA TECHNICAL PAPERS .....	320
AUTHORS .....	323

---

© 1964 by Radio Corporation of America  
All rights reserved

---

RCA REVIEW is regularly abstracted and indexed by *Abstracts of Photographic Science and Engineering Literature*, *Applied Science and Technology Index*, *Bulletin Signalétique des Télécommunications*, *Chemical Abstracts*, *Electronic and Radio Engineer*, *Mathematical Reviews*, and *Science Abstracts* (I.E.E.-Brit.).

# RCA REVIEW

---

## BOARD OF EDITORS

### Chairman

R. S. HOLMES  
*RCA Laboratories*

E. I. ANDERSON  
*Home Instruments Division*

A. A. BARCO  
*RCA Laboratories*

E. D. BECKEN  
*RCA Communications, Inc.*

G. L. BEERS  
*Radio Corporation of America*

G. H. BROWN  
*Radio Corporation of America*

A. L. CONRAD  
*RCA Service Company*

E. W. ENGSTROM  
*Radio Corporation of America*

D. H. EWING  
*Radio Corporation of America*

A. N. GOLDSMITH  
*Honorary Vice President, RCA*

J. HILLIER  
*RCA Laboratories*

E. C. HUGHES  
*Electronic Components and Devices*

E. O. JOHNSON  
*Electronic Components and Devices*

E. A. LAPORT  
*Radio Corporation of America*

H. W. LEVERENZ  
*RCA Laboratories*

G. F. MAEDEL  
*RCA Institutes, Inc.*

W. C. MORRISON  
*Broadcast and Communications  
Products Division*

L. S. NERGAARD  
*RCA Laboratories*

H. F. OLSON  
*RCA Laboratories*

J. A. RAJCHMAN  
*RCA Laboratories*

D. F. SCHMIT  
*Radio Corporation of America*

L. A. SHOTLIFF  
*RCA International Division*

C. P. SMITH  
*RCA Laboratories*

W. M. WEBSTER  
*RCA Laboratories*

### Secretary

C. C. FOSTER  
*RCA Laboratories*

---

## REPUBLICATION AND TRANSLATION

Original papers published herein may be referenced or abstracted without further authorization provided proper notation concerning authors and source is included. All rights of republication, including translation into foreign languages, are reserved by RCA Review. Requests for republication and translation privileges should be addressed to *The Manager*.

# PREPARATION, OPTICAL PROPERTIES, AND BAND STRUCTURE OF BORON MONOPHOSPHIDE

BY

C. C. WANG, M. CARDONA, AND A. G. FISCHER

RCA Laboratories  
Princeton, N. J.

*Summary*—Microcrystalline BP powder, synthesized by replacement reaction of boron halide and  $Zn_3P_2$ , was converted to single crystals by recrystallization from metal solutions. It was found that BP does not show solid solubility in AlP and GaP, but is soluble to a high degree in BAs. The fundamental absorption edge of BP from transmission measurements is near 2 eV and caused by indirect transitions from the  $k=0$  top of the valence band to a conduction band minimum at the X-point. This small value of the energy gap is attributed to an extremely small ionicity. Reflectivity structure at 5.0, 6.9 and 7.9 eV corresponds to direct interband transitions at high symmetry points of  $k$  space. The band structure of BP is discussed and compared to the band structure of  $\beta$ -SiC.

## INTRODUCTION

AMONG THE group III-V compound semiconductors, the boron-group-V compounds are least known, mainly because of the difficulties involved in their synthesis. BP, a member of this group, shows both physical and chemical properties that differ from the general trend of the III-V family. Due to its high melting point ( $\sim 3000^\circ$  C), high dissociation pressure, and incongruent decomposition<sup>1</sup> at elevated temperatures into phosphorus and a lower phosphide, it would be very difficult to grow BP crystals by conventional methods (such as zone refining and growth from the melt). Thus, many of the important basic physical properties of BP are not yet well established, in spite of the scientific interest in this compound stimulated by its potential as a candidate for solid-state devices. In this paper, a method for the synthesis of BP single crystals and results of some optical measurements on these crystals are presented and described in terms of the energy-band structure. This structure is compared to the band structures of other materials of the zinc-blende and diamond family.

<sup>1</sup> V. I. Matkovich, "Unit Cell, Space Group and Composition of a Lower Boron Phosphide," *Acta Cryst.*, Vol. 14, p. 93, 1961.

## PREPARATION OF BP

Synthesis of BP has been reported in the literature.<sup>2-9</sup> Here we shall describe a new process and technique for preparing it. BP microcrystalline powder of high purity (99.99%, impurity mainly silicon) was synthesized by the replacement reaction of boron halide ( $\text{BCl}_3$  or  $\text{BBr}_3$ ) and  $\text{Zn}_3\text{P}_2$  at  $1000^\circ\text{C}$  in an all-quartz flow system under argon atmosphere. To convert this powder to single crystals, it was dissolved in metal solvents (Ni, Fe, Pt, Ge) which were heated by r-f to  $1300^\circ$  to  $1500^\circ\text{C}$  in closed quartz ampoules under phosphorus pressure of about 1 atm. The saturated solution was then slowly cooled. The crystals so grown are orange-red, several mm in size, polyhedral in shape, hard, and brittle. They have a bulk p-type conductivity. Their room-temperature resistivity is  $10^{-2}$  ohm-cm. Hall measurements showed that the carrier concentration is  $10^{18}/\text{cm}^3$  and  $10^{17}/\text{cm}^3$  at room temperature and liquid nitrogen temperature, respectively. The hole mobility is about  $500 \text{ cm}^2/\text{volt-sec}$  for the crystals at room temperature. Red injection electroluminescence is observed at the anode if the crystals are contacted with metal probes. Small, yellow needle-shaped BP crystals were also grown by vapor phase reaction of boron oxide or boron oxysulfide with phosphorus. The powder x-ray diffraction method was used to identify the BP—it has a zincblende type cubic structure with a unit cell dimension of  $4.538 \text{ \AA}$ , which agrees well with the literature value.<sup>10</sup> The monocrystallinity of many BP crystals grown from solution was revealed by the Laue back-reflection method. The most pronounced impurity in the crystals was the solvent (such as Ni), generally in the order of  $10^{-4}$  as examined by emission spectral analysis.

## OPTICAL MEASUREMENTS

Transmission and specular reflection measurements were made in

<sup>2</sup> H. Moissan, *Comp. Rend.*, Vol. 113, p. 726, 1891.

<sup>3</sup> P. Popper and T. A. Ingles, "Boron Phosphide, a III-V Compound of Zinc-Blende Structure," *Nature*, Vol. 179, p. 1075, May 25, 1957.

<sup>4</sup> K. Vickery, "Synthesis of Boron Phosphide and Nitride," *Nature*, Vol. 184, p. 268, July 25, 1959.

<sup>5</sup> F. V. Williams and R. A. Ruehrwein, "The Preparation and Properties of Boron Phosphides and Arsenides," *Jour. Amer. Chem. Soc.*, Vol. 82, p. 1330, 1960.

<sup>6</sup> B. D. Stone, U. S. Patent 3009.780 (1961).

<sup>7</sup> E. S. Greiner, "The Floating-Zone Melting of Boron and the Properties of Boron and Its Alloys," *Proc. of the Conference of Boron*, Plenum Press, Inc., New York, 1960.

<sup>8</sup> G. V. Samsonov and Y. B. Tithov, "Production of Boron Monophosphite," *Russian Jour. Appl. Chem.*, Vol. 36, p. 669, 1963.

<sup>9</sup> J. L. Peret, "Preparation and Properties of the Boron Phosphide," *Jour. Amer. Cer. Soc.*, Vol. 47, No. 1, p. 44, Jan. 1964.

<sup>10</sup> ASTM Card File (11-119).

order to study the interband transitions in the fundamental absorption region of BP. Also, the absorption of a BP single-crystal specimen lapped and polished with diamond paste was measured in the wavelength ranges of 0.5-1.5  $\mu$  using a Cary model 14 spectrophotometer. Figure 1 shows a plot of optical transmission versus wavelength.

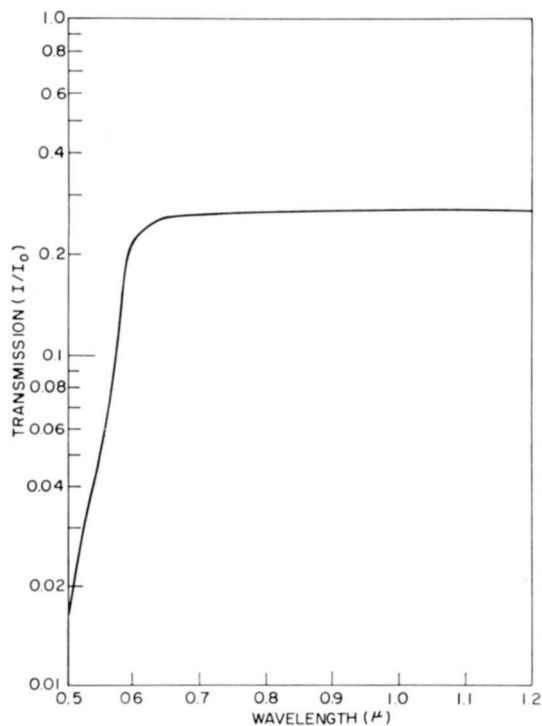


Fig. 1—Optical transmission of BP at room temperature.

Figure 2 is a plot of the square root of the absorption coefficient of BP and  $\beta$ -SiC<sup>11</sup> as a function of photon energy. The absorption of  $\beta$ -SiC has been included for the sake of comparison since, as it will be shown in the discussion, the energy bands of BP and  $\beta$ -SiC are very similar. The lowest energy gap of SiC<sup>11</sup> (2.2 eV) is thought to be indirect. From the similarity of the band structures and absorption coefficients of BP and SiC, we believe that the 2.0 eV absorption edge

<sup>11</sup> H. R. Philipp and E. A. Taft, "Intrinsic Optical Absorption in Single Crystal Silicon Carbide," *Proc. of the Conference on Silicon Carbide*, Pergamon Press, New York, 1960.

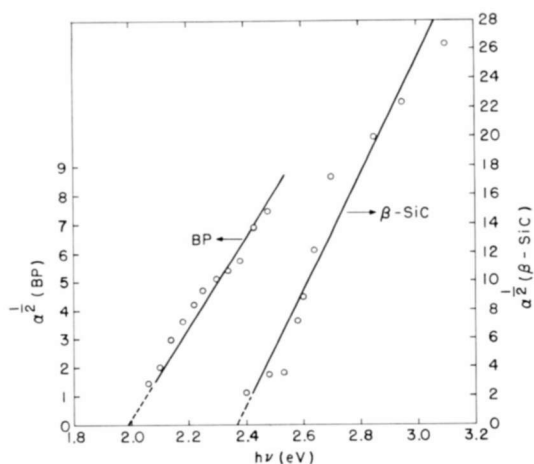


Fig. 2—Square root of absorption coefficient versus photon energy for BP and  $\beta$ -SiC.

shown in Figure 2 for BP is an indirect edge. The nearly linear plot of  $\alpha^{1/2}$  versus photon energy tends to confirm this result.<sup>12</sup>

Reflectivity measurements were made on an as-grown surface of BP in the wavelength range of 0.05-0.6  $\mu$  using a 50-cm Bausch and Lomb grating instrument and a Jarrell-Ash 1-meter Seya-type spectrometer. The results are presented in Figure 3. A main reflectivity maximum was derived at 6.9 eV. By analogy with other materials of

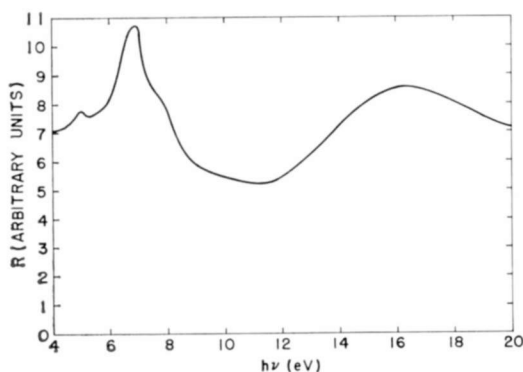


Fig. 3—Optical reflection of BP at room temperature.

<sup>12</sup> J. Bardeen, F. J. Blatt and L. H. Hill, "Indirect Transitions from the Valence to the Conduction Bands," *Photoconductivity Conference*, John Wiley and Sons, Inc., New York, N. Y., 1956.

the same family,<sup>13</sup> the main maximum of 6.9 eV is interpreted as due to transition at the x point of the Brillouin zone. A weak maximum at 5.0 eV could be the  $\Gamma_{15} - \Gamma_{15}$  transitions. The shoulder seen at 8.0 eV seems due to  $L_{3'} - L_3$  transitions. The reasons for these assignments are examined in the discussion.

Transmission measurements in the infrared range, 2.5-25  $\mu$ , on BP single-crystal specimens were also made using a Perkin-Elmer instrument. No positions of strong absorption could be unambiguously located yet, although an attempt was made to determine the Reststrahlen wavelength.

The energy gap of BP was previously reported to be 5.9 eV<sup>14</sup> and 4.5 eV,<sup>8</sup> and a strong absorption of BP polycrystalline thin film at about 12  $\mu$  was observed.<sup>14</sup> Using single-crystal specimens, we find in this work that BP has an energy gap of 2.0 eV and no strong absorption in the infrared range. The low value of the band gap has been found before by one of the authors from the slope of log resistivity versus inverse temperature measurements on sintered BP crusts.<sup>15</sup>

#### SOLID SOLUBILITY WITH ALP, GAP AND BAS

The solubility of BP in AlP and GaP was investigated in the following way. B-Al alloys or B-Ga mixtures were r-f heated in BN crucibles with tungsten susceptors in sealed quartz ampoules under 20 atm of phosphorus pressure (Figure 4). X-ray analysis showed that except for a few percent at the ends of the BP-AlP and BP-GaP phase diagrams, there is no solid solubility. The determination of solubility in the system BP-BAs is more difficult due to the need of a combined P-As atmosphere to prevent decomposition. In preliminary experiments, pellets pressed from mixtures of BP and BAs powder were heated at 700°C in argon for two weeks. X-ray analysis showed solid solubility to at least up to 15% BAs in BP, which is to be expected from the similar lattice constants and electronegativity differences of BP and BAs.

#### DISCUSSION

The band structure of a III-V compound can be obtained by perturbation theory from the band structure of the group IV-IV material

<sup>13</sup> M. Cardona, "Band Parameters of Semiconductors with Zincblende, Wurtzite, and Germanium Structure," *Jour. Phys. Chem. Solids*, Vol. 24, p. 1543, 1963.

<sup>14</sup> B. Stone and P. Hill, "Semiconducting Properties of Cubic Boron Phosphide," *Phys. Rev. Letters*, Vol. 4, No. 6, p. 282, March 15, 1960.

<sup>15</sup> A. G. Fischer, Thesis, *Electroluminescence*, University of Giessen, Germany, 1957.

obtained by moving horizontally in the periodic table from the constituent atoms of the III-V compound.<sup>13</sup> The difference between the crystal potential of the III-V compound and the corresponding group IV-IV material is assumed to be an antisymmetric potential changing like the  $\Gamma_2'$  representation of the full cubic group. If the two constituent

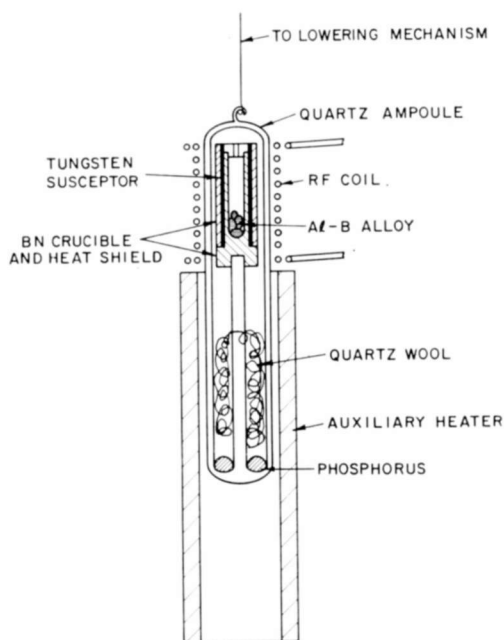


Fig. 4—Apparatus for synthesis of BP alloys.

atoms belong to different rows of the periodic table, the corresponding group-IV material does not have inversion symmetry, and thus its potential can be written as the sum of a symmetric and an antisymmetric component. For group-IV materials composed of Ge, Si, and Sn, the effects of the antisymmetric part of the potential is very small and the band structure is roughly the average of the structures of the two constituent atoms.<sup>13</sup> This result is to be expected in the pseudopotential scheme,<sup>16</sup> because orthogonalization of the plane waves to the core states introduces an effective repulsive potential which cancels the core potentials. However, in carbon this cancellation does not take

<sup>16</sup> L. Kleinman and J. C. Philips, "Crystal Potential and Energy Bands of Semiconductors. II. Self-Consistent Calculations for Cubic Boron Nitride," *Phy. Rev.*, Vol. 117, No. 2, p. 460, Jan. 15, 1960.

place for the  $p$  valence electrons; since the core only has  $s$  states, the  $p$  valence electrons are automatically orthogonal to the core states, as pointed out by L. Kleinman. Hence, in a group IV-IV material with carbon as a constituent, the effective attractive core potential is much stronger around the carbon than around the other constituent. This produces a strong antisymmetric component of the crystal potential and an accumulation of the  $p$  valence electrons around the carbon atom. This is the case of  $\beta$ -SiC, the group IV-IV material corresponding to BP.

Let us first examine the indirect gap of  $\beta$ -SiC, which occurs at 2.2 eV,<sup>11</sup> and is probably due to transitions from the top valence band at  $k=0$  ( $\Gamma_{25}'$  in germanium structures,  $\Gamma_{15}$  zincblende) to the lowest conduction band at X ( $X_3$  if the origin of coordinates is at a carbon atom).<sup>17</sup> This gap is nearly the same as the indirect gap of silicon and diamond except for the fact that the lowest conduction band at X,  $X_1$  in materials with inversion symmetry (silicon, diamond), splits into  $X_1$  and  $X_3$  when the inversion symmetry is lifted ( $\beta$ -SiC). Since gaps are normally larger for polar materials than for the corresponding nonpolar materials, one might expect the indirect gap of  $\beta$ -SiC to be even larger than the average gap of silicon and diamond (3.2 eV). This would be true if no degenerate states, which split to first order under an antisymmetric perturbation, were involved in this gap. However, the  $X_1$  state of the symmetric crystal is such a state, and its splitting ( $X_1$ - $X_3$ ) under the antisymmetric perturbation produces a decrease in the indirect gap approximately equal to 2.2 eV<sup>17,18</sup>, which approximately cancels the increase due to the repulsion of the  $\Gamma_{25}'$  state by the  $\Gamma_{15}$  conduction band (2.5 eV<sup>17,18</sup>). Hence, it is not surprising to find an indirect gap as small as 2.2 eV for  $\beta$ -SiC in spite of its polar nature.

The band structure of BP can be obtained from the structure of  $\beta$ -SiC by adding to the crystal potential of  $\beta$ -SiC another antisymmetric potential produced by the difference in core charges of boron and phosphorus. This potential is attractive around the phosphorus and repulsive around the boron. If we think of BP as derived from  $\beta$ -SiC by replacement of the silicon atom by phosphorus and the carbon by boron, the additional antisymmetric potential of BP must partially compensate

---

<sup>17</sup> S. Kobayasi, "Calculation of the Energy Band Structure of the  $\beta$ -SiC Crystal by the Orthogonalized Plane Wave Method," *Jour. Phys. Soc. Japan*, Vol. 13, No. 3, p. 261, March 1958.

<sup>18</sup> F. Bassani and M. Yoshimine, "Electronic Band Structure of Group IV Elements and of III-V Compounds," *Phys. Rev.*, Vol. 130, No. 1, p. 20, April 1, 1963.

the antisymmetric component of the crystal potential of SiC. Thus, BP would be expected to be *less* polar than SiC. It is easy to show that this compensation is almost complete.

Let us consider for instance the splitting of the  $X_1$  state of the symmetrized crystal into  $X_1$  and  $X_3$  by the antisymmetric potential. We have mentioned that this splitting is about 4.4 eV, the  $X_3$  state being lower in energy if the origin of coordinates is the carbon atom. We can estimate the effect of the difference in core charges on this splitting by assuming this effect is the same as in BN, since the only

Table I—Energies of Reflection Peaks (in eV) and Corresponding Electronic Transitions in Diamond, BP, and Silicon

	Diamond*	BP†	Si‡
$\Gamma_{25}'-\Gamma_{15}$	7.3	5	3.4
$X_4-X_1$	12.6	6.9	4.4
$L_{25}'-L_3$	?	8.0	5.5

\* H. R. Phillipp and E. A. Taft, "Optical Properties of Diamond in the Vacuum Ultraviolet," *Phys. Rev.*, Vol. 127, p. 159, 1962.

† This work.

‡ See Reference (13).

difference in core potentials in BN comes from the difference in core charges. For BN the  $X_1$ - $X_3$  splitting is 4.3 eV<sup>18</sup> and the lowest state is now  $X_1$  if the origin of coordinates is taken to be the boron atom. Therefore, it is clear that the difference in repulsive orthogonalization potential nearly cancels the potential due to the difference in core charges. Hence, the band structure of BP is expected to be the same as the band structure of symmetrized  $\beta$ -SiC (with only the symmetric component of its crystal potential). All energy gaps of BP should be *smaller* than the corresponding gaps of  $\beta$ -SiC except possibly the gaps involving the  $X_1$ - $X_3$  points. From the previous discussion we would expect the lowest indirect gap ( $\Gamma_{25}'-X_1$  for the symmetrized crystal) to be about the same as the corresponding gap of  $\beta$ -SiC.<sup>19</sup> This conclusion is borne out by experiments.

It is easy to estimate by the same technique the  $\Gamma_{15}-X_3$  energy

<sup>19</sup> A band gap of 2 eV was recently reported by R. J. Archer, R. Y. Loyama, E. E. Loebner, and R. C. Lucas, "Optical Absorption, Electroluminescence, and the Band Gap of BP," *Phys. Rev. Letters*, Vol. 12, p. 538, 1964.

gap of AlN, which is probably its smallest energy gap. In this material the effects of the two antisymmetric potentials add and the  $\Gamma_{15} - X_3$  gap would be expected to be about 4.3 eV.<sup>20</sup> The direct gaps observed by reflection in BP should occur approximately at the average energy of the corresponding gaps in diamond and silicon. For the sake of comparison, the energies of the  $X_4 - X$ ,  $\Gamma_{25}' - \Gamma_{15}$  and  $L_3' - L_3$  gaps in diamond, Si, and BP are listed in Table I. The almost completely covalent character of BP may account for our failure to see the Reststrahlen spectrum of this material.

---

<sup>20</sup> E. Kauer and A. Rabenau, "Energy Gaps of Aluminum Nitride and Gallium Nitride," *Z. für Naturforsch.*, Vol. 12a, p. 942, 1957.

# FREE-SPACE MICROWAVE TECHNIQUES FOR PLASMA MEASUREMENTS\*

BY

M. P. BACHYNSKI AND G. G. CLOUTIER†

RCA Victor Company, Ltd.,  
Montreal, Canada

*Summary*—The determination of plasma properties from the transmission or reflection of electromagnetic waves is strongly influenced by the experimental configuration and microwave system used in the measurements. It thus becomes necessary to ascertain the experimental effects in detail in order to either eliminate or minimize their influence and hence to be able to make a quantitative interpretation of the measurements.

Three experimental microwave arrangements — a simple source and receiver, a lens transmitter and lens receiver system, and a lens transmitter with a simple receiver — have been studied at X-band (10 gc) frequencies for application to measurements of the properties of a plasma in the configuration of a finite slab. The effects of stray scattering, diffraction, source directivity, plasma container, and multiple reflections for each arrangement were examined. Based on these measurements, the "optimum" arrangement was used to study transmission and reflection of electromagnetic waves by a slab of plasma in order to ascertain the best arrangement for measuring the properties of the plasma.

Of the three microwave arrangements, only the lens-transmitter-lens-receiver system, if used with suitable precautions, appears to be acceptable for measuring the properties of a plasma in the configuration of a finite slab by free-space propagation of electromagnetic waves.

## INTRODUCTION

THE DETERMINATION of the properties of a plasma from measurements of the phase change and attenuation introduced by the plasma to an incident electromagnetic wave that has either been transmitted through or reflected from the plasma is well known.<sup>1-11</sup> The accuracy of such measurements is limited not only by

\* Performed under Air Force Cambridge Research Laboratories contract AF 19(604)-7334.

† Present address, Department of Physics, University of Montreal, Montreal, Canada.

<sup>1</sup> C. B. Wharton, J. C. Howard, and O. Heinz, "Plasma Diagnostic Development in UCRL Pyrotron Program," 2nd Int. Symp. on Peaceful Uses of Atomic Energy, Vol. 32, p. 388 (1958).

<sup>2</sup> M. A. Heald, "The Application of Microwave Techniques to Stellarator Research," Princeton University Project Matterhorn Report MATT-17, Aug. 1959.

the inability to precisely prescribe the properties of a finite plasma,<sup>12</sup> but also by the inherent characteristics of the measurement system. In order to be able to make a detailed quantitative interpretation of the microwave measurements of the properties of plasmas by this "free-space" propagation technique, it is essential to have a detailed knowledge of the possible influence of various factors. These are determined by the experimental system and include the curvature of the phase front of the incident field, the finite size and directivity of the source and receiver, the possible location of the plasma in the near field of the source, and any multiple interaction that may occur among the source, the plasma container, the plasma, and the receiver.

To date, there does not appear to have been a systematic attempt made to assess the properties of various microwave arrangements for determining the characteristics of finite plasmas using free-space electromagnetic waves. It is the purpose of this paper to show how important the effect of the measurement system may be in various experimental configurations and demonstrate how these effects can be minimized for certain geometries. It is only in this way that the optimum arrangement for a given experimental system can be ascertained and the degree of accuracy of the experimental measurements

---

<sup>3</sup> C. B. Wharton, "International Summer Course in Plasma Physics," Danish Atomic Energy Commission Report No. 18, pp. 579-582 (1960).

<sup>4</sup> R. Motley and M. A. Heald, "Use of Multiple Polarizations for Electron Density Profile Measurements in High Temperature Plasmas," *Proc. Symp. on Millimetre Waves*, pp. 141-154, Polytechnic Press, N.Y. (1960).

<sup>5</sup> C. B. Wharton, "Microwave Diagnostics for Controlled Fusion Research," in *Plasma Physics*, ed. J. Drummond, pp. 307-331, McGraw-Hill Book Company, N.Y. (1961).

<sup>6</sup> R. J. Jahn, "Microwave Probing of Ionized-Gas Flows," *Phys. Fluids*, Vol. 5, p. 678, June 1962.

<sup>7</sup> P. W. Kuhns, "Microwave Measurements of Steady-State and Decaying Plasmas," *Trans. IRE PGSET*, Vol. 8, p. 173, June 1962.

<sup>8</sup> R. Buser and W. Buser, "Determination of Plasma Properties by Free-Space Microwave Techniques," *Jour. Appl. Phys.*, Vol. 33, p. 2275, July 1962.

<sup>9</sup> R. Warder, M. Brodwin, and A. B. Cambel, "Sources of Error in the Microwave Diagnostics of Plasmas," *Jour. Appl. Phys.*, Vol. 33, p. 2868, Sept. 1962.

<sup>10</sup> G. R. Nicoll and J. Baser, "Comparison of Microwave and Langmuir Probe Measurements on a Gaseous Plasma," *Jour. Elect. Cont.*, Vol. XII, p. 23, June 1962.

<sup>11</sup> L. Talbot, J. E. Katz, and C. L. Brundin, "Comparison Between Langmuir Probe and Microwave Electron Density Measurements in an Arc-Heated, Low-Density Wind Tunnel," *Phys. Fluids*, Vol. 6, p. 559, April 1963.

<sup>12</sup> M. P. Bachynski and K. A. Graf, "Electromagnetic Properties of Finite Plasmas," *RCA Review*, Vol. XXV, p. 3, March 1964.

determined. The microwave apparatus and experimental arrangements tested are described first, followed by an account of the experimental effects introduced by the measurement system. Finally, free-space microwave measurements in the presence of plasma for various microwave systems are assessed.

#### EXPERIMENTAL MICROWAVE APPARATUS AND ARRANGEMENTS

The experimental system for the measurement of electromagnetic waves transmitted through a plasma is shown in Figure 1a. Various arrangements of the source, plasma, and receiver are possible and are

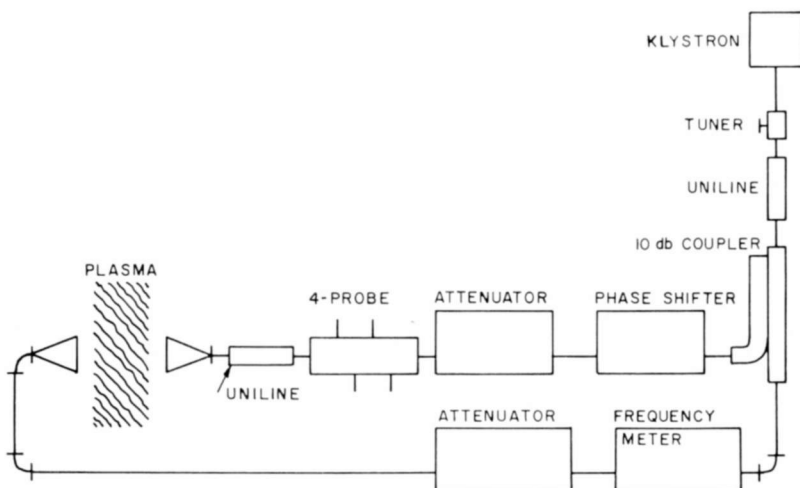


Fig. 1(a)—Microwave arrangement for measurement of transmission of electromagnetic waves through a slab of plasma.

described later in this section. A similar system adapted for reflection measurements is shown in Figure 1b. The measurement of amplitude and phase of either the transmitted or reflected signal (depending on the system—Figure 1a or 1b) is made through use of the multiple-probe microwave unit.<sup>13</sup> This unit is especially convenient for microwave measurements of time-varying plasmas since the output from the four-probe unit can be displayed on an X-Y oscilloscope to give a direct polar display of amplitude (radius vector) and phase (polar angle) at various times so as to trace out a time history of the inter-

<sup>13</sup> F. J. F. Osborne, "A Multiple-Probe Microwave System for Plasma Studies," *Can. Jour. Phys.*, Vol. 40, p. 1620, 1962.

action of the microwave signal with a plasma. Typical displays of the variations of the microwave signal transmitted through and reflected by a time varying plasma are shown in Figure 2. The plasma used in the above and subsequent measurements (to be shown) was generated by an electrical discharge in helium confined in a container with two parallel dielectric faces so that the plasma geometry would approximate a uniform slab. The traces of Figure 2 show the variation of phase and amplitude of the microwave signal for a sampling rate of 10 kc of the 60-cycle repetitive discharge.

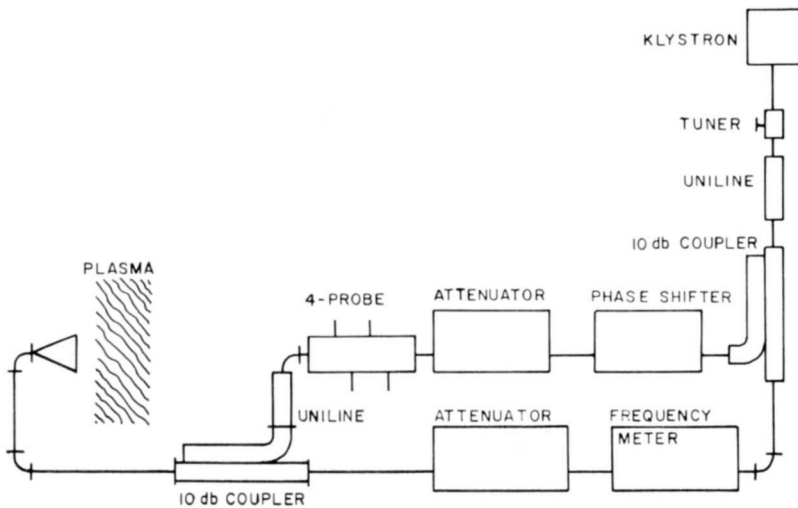


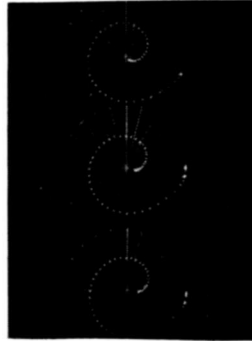
Fig. 1(b)—Microwave arrangement for measurement of reflection of electromagnetic waves from a slab of plasma.

An extensive series of measurements has been carried out on three basic experimental arrangements in order to establish the microwave characteristics of the measuring system in the absence of a plasma. All the measurements have been performed at a frequency of about 10 gc. With no plasma, the signal intensity as a function of position of the geometric arrangement was required, and measurements were then made using an antenna pattern recorder instead of the four-probe unit.

#### EXPERIMENTAL EFFECTS OF MICROWAVE SYSTEM

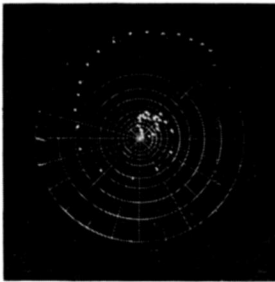
The presence of a plasma in the medium separating the transmitting and receiving antennas has the effect of changing the optical path length of a microwave beam traversing the system. Effectively, a

change in the plasma intensity corresponds, as far as the phase of the wave is concerned, to a displacement of the microwave source along the axis of propagation. Therefore, by changing the distance between the receiver and transmitter in the absence of the plasma, and by



$f = 9.7 \text{ Gc}$

(a)



(b)

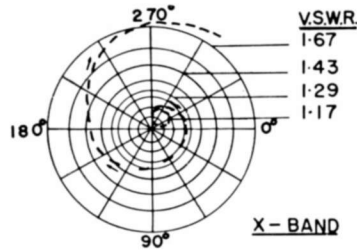


Fig. 2—Multiple-probe displays for (a) transmission through the plasma, (b) reflection from the plasma.

measuring the corresponding variation of the power received, it is possible to examine some aspects of the propagation characteristics of the system as if the plasma were present. As shown later, such an experiment permits the examination of other phenomena (such as refraction, reflection, and diffraction) affecting the characteristics of the microwave system and the determination of the optimum conditions for obtaining meaningful data in a free-space microwave measurement of a plasma.

For the measurements described, the transmitting antenna (microwave horn or lens) was located on the axis of a cylindrical plasma container at a fixed distance from it. The receiving antenna was mounted on an optical bench and could be displaced along the axis of the cylindrical container over a distance of approximately two meters. The signal detected at the receiving antenna was displayed on a logarithmic antenna recorder in such a way that a reading of the relative power as function of the displacement of the receiver could be made.

### ***Microwave System Consisting of Transmitting and Receiving Antennas***

A series of measurements have been performed using the configuration shown in Figure 3a and the following effects studied.

#### *Stray Scattering*

Stray scattering is defined as the energy, emerging from the transmitting antenna, that reaches the receiver after reflection from objects surrounding the plasma container. Stray scattering can be reduced or eliminated by placing a metal screen around the plasma container and by surrounding the antennas and the plasma container with microwave absorbing material. In this way, any energy not directed toward the plasma container is prevented from reaching the receiving antenna. The effect of stray scattering is illustrated in Figure 4, which shows the measurement of received power for a given position of the transmitting antenna as function of receiver position with and without a metal screen around the plasma container. The use of a metal screen greatly reduces the large irregular fluctuations in the received signal.

The use of a metal screen around the plasma container gives rise to a stronger diffraction effect because of the sharp discontinuity in the refractive index at the periphery of the cylindrical container. This is not really a disadvantage since even without the metal screen a certain amount of diffraction takes place which, when mixed with the stray scattering, cannot in general be treated theoretically. The theory of diffraction by an aperture in a metal screen is well known for the case of a circular aperture.

#### *Diffraction Effects*

In most laboratory arrangements, the plasma is located in the "near field" of a diffracting aperture. The major diffraction effect is due to the plasma container, and gives rise to the oscillatory structure of the field along the axis of the experimental system. For distances not

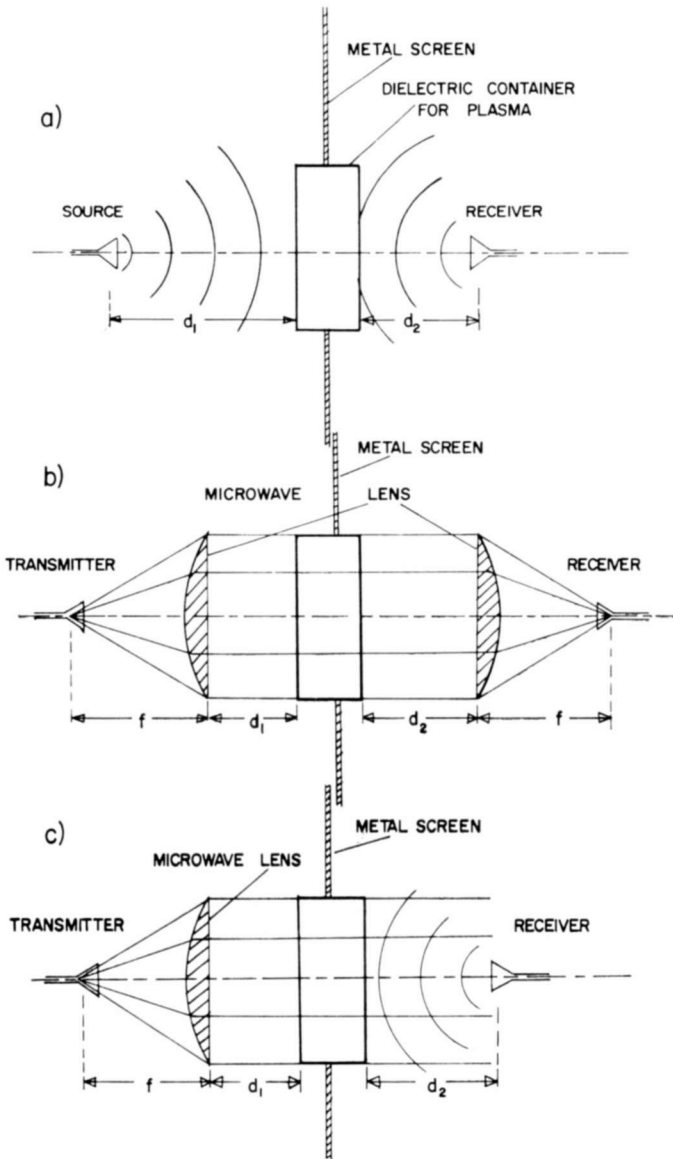


Fig. 3—Basic microwave systems for studying plasma by free-space propagation.

too close to the aperture itself, the diffracted field can be predicted from the Kirchhoff theory.<sup>12</sup> As can be seen from Figure 4, at distances near the plasma container rapid variations in signal intensity can occur for small displacement in position (or small changes in

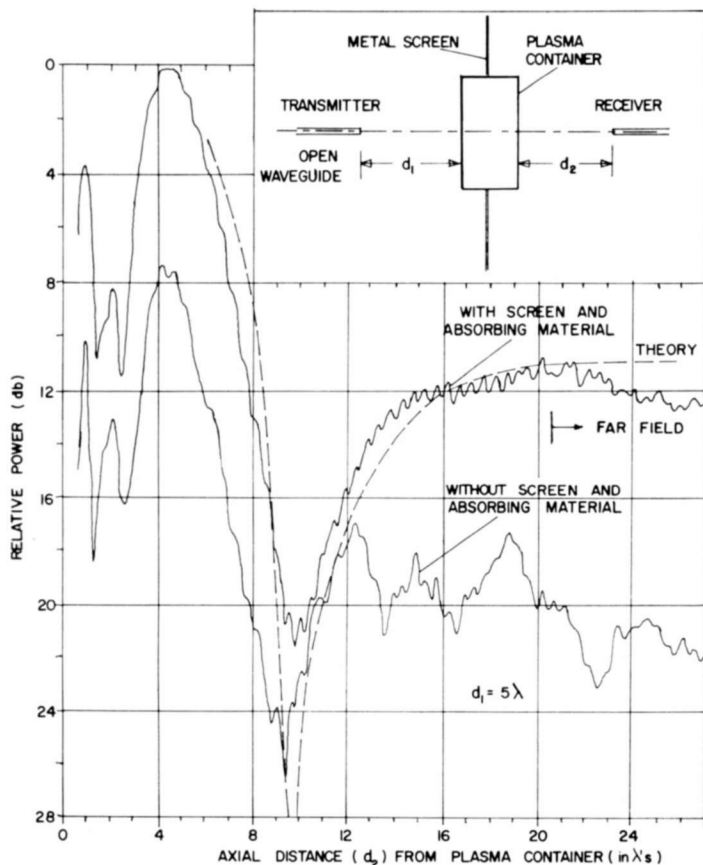


Fig. 4—Variation of power received along the axis of propagation using open waveguides for transmitting and receiving. These measurements illustrate the influence of stray scattering on the axial field.

plasma properties). It is thus essential that the receiver in any experiment designed to measure the properties of plasmas be located sufficiently far from the plasma to be in the "far" diffraction field.

#### Source Directivity

The directivity of the source illuminating the plasma has a pro-

found influence on the field in the transmitted region as shown in Figure 5. With the source located very near the plasma container no diffraction effect occurs, but violent undulations in the received signal, particularly near the container, are apparent. As the source is moved away from the plasma container, a greater illumination of the dif-

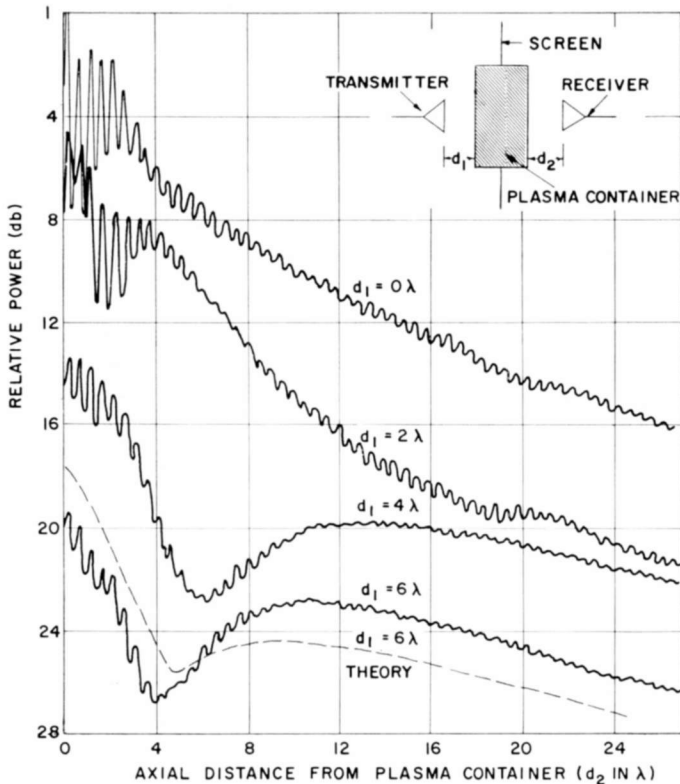


Fig. 5—Microwave power received as function of distance from the plasma container when 15-db-gain horns are used as source and receiver. Each measurement represents a different position of the transmitter with respect to the plasma container.

fracting aperture occurs and the electromagnetic field in the receiving region again exhibits a diffraction pattern. In any case, an arrangement with the transmitter and/or receiver near the plasma container is very sensitive to large variations in signal intensity (due to multiple reflections, as demonstrated later).

(One should note that the degree of stray scattering also depends on the directivity of the transmitting and receiving antennas. If no

diffraction screen is possible because of the experimental arrangement, then directive sources can be used to reduce the stray scattering.)

#### *Influence of Plasma Container on Microwave Measurements*

Tests have been carried out to determine the influence of the

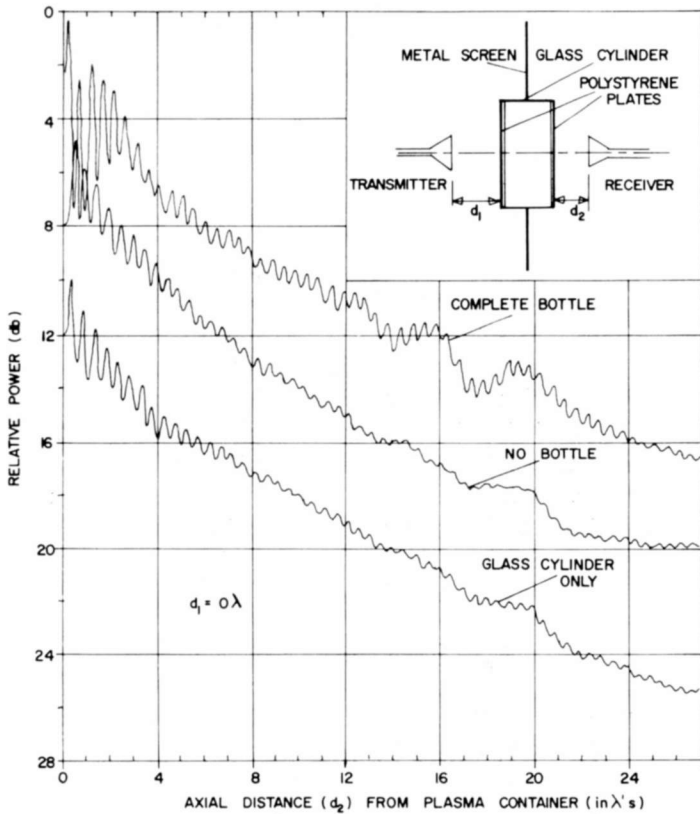


Fig. 6—Influence of the plasma container on the microwave measurements.

plasma (dielectric) container on the microwave measurements. For a given position of the transmitting horn on the axis of the cylindrical bottle, the receiving horn was displaced along the axis of propagation, and the field intensity was plotted as function of the position of the receiver. The cylindrical container was then removed and the same procedure was repeated. Measurements were also obtained by leaving the cylindrical section of the container in position and removing the two flat polystyrene plates. The set of data so obtained is shown in Figure 6. During these measurements the transmitting 15-db-gain

horn was located against the flat face of the dielectric container and kept in the same position when the container was removed. It is interesting to note that, although larger undulations due to multiple reflections are observed when the plasma container is present, the general shape of the curve remains essentially unchanged whether the dielectric bottle is present or not. The curve obtained when only the cylindrical section of the container is in place indicates that the undulations observed are mostly due to the flat faces of the plasma container.

This experiment thus indicates that the plasma container itself does not influence appreciably the microwave measurements in this system.

### *Multiple Reflections*

In order to facilitate the interpretation of the undulations observed in the field intensity, one can use the simple model of an electromagnetic wave propagating through the system and being reflected at various surfaces. When the receiver is perfectly matched to the rest of the system (Figure 7a), no undulations will appear on the plot of power versus position of the receiver. There may be reflections between the transmitting horn and the dielectric slab, but since the resulting wave transmitted through the dielectric slab is not reflected by the receiver, no interference effect takes place as the receiver is displaced, and no undulation will appear in the variation of field intensity with receiver position. If one considers a simple wave traveling through the system, then the electric field ( $E_r$ ) at the receiver is

$$E_r = E_i \exp \{ ik(d_1 + t + d_2) \},$$

where  $E_i$  contains the distance dependence of the fields, i.e.,  $E_i = E_0/f(r)$ , where  $E_0$  is a constant. In the far field, for example,  $f(r) = r$ , while in the near field it may be a more complicated function;

$d_1$  is the distance from the transmitter to the dielectric slab;

$t$  is the optical thickness of the slab;

$d_2$  is the distance from the dielectric slab to the receiver;

$k = 2\pi/\lambda$ , the usual wave number.

Since in the present experiment the field intensity ( $I_r$ ), instead of the amplitude ( $E_r$ ), is measured at the receiver, the output will be

$$I_r = E_r E_r^* = E_i^2.$$

To understand the type of undulations observed when the receiver is slightly mismatched, consider the field incident on the receiver and a reflected component that is attributed to a reflection of the incident field from the receiving antenna with a further reflection at the container (Figure 7b). More reflections can take place, but a reasonable

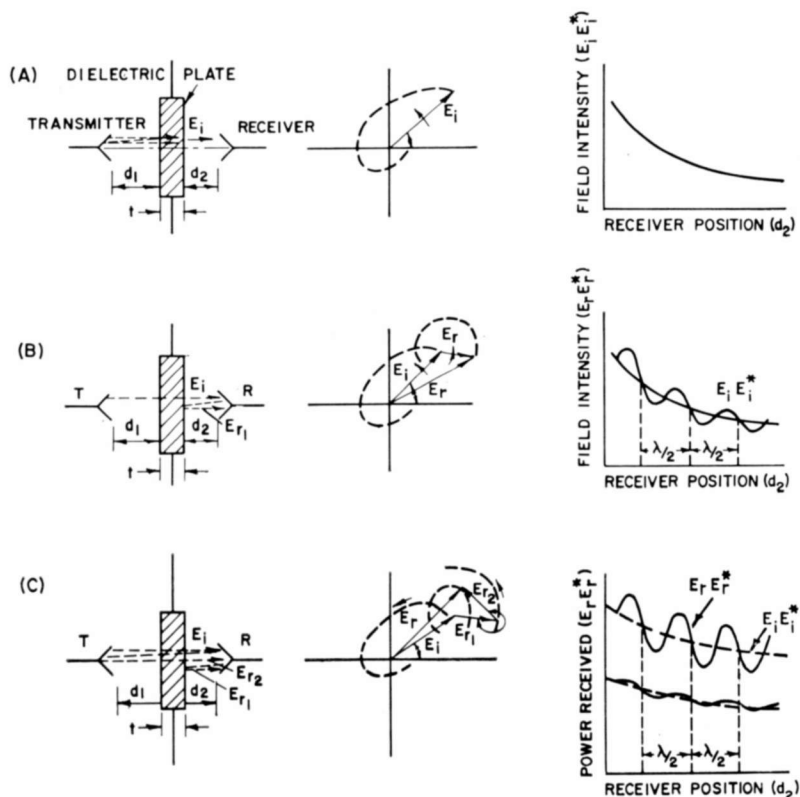


Fig. 7—Diagrams illustrating the models used in the interpretation of the undulations observed in the received power.

assumption (as shown to be the case experimentally) is that the other reflections are small compared with the initial one.

In this case the field seen by the receiver can be expressed as

$$E_r = E_i \exp\{ik(d_1 + t + d_2)\} + E_{r_1} \exp\{ik(d_1 + t + 3d_2)\},$$

where  $E_{r_1}$  is the amplitude of the reflected component of the incident wave reaching the receiver (including the distance dependence).

The signal received is thus regarded as made up of two interfering

signals and the relative phase of these signals depends on the position of the receiver. The power is then given by

$$I_r = E_r E_r^* = E_i^2 + E_{r_1}^2 + 2E_i E_{r_1} \cos 2kd_2.$$

For

$$E_{r_1}^2 \ll E_i^2, \quad I_r = E_i^2 \left( 1 + 2 \frac{E_{r_1}}{E_i} \cos 2kd_2 \right)$$

The power received is composed of a constant term ( $E_i^2 + E_{r_1}^2$ ) and an oscillating term ( $2E_i E_{r_1} \cos 2kd_2$ ) that will undergo a complete cycle when the receiver position ( $d_2$ ) is displaced by a half-wavelength ( $\lambda/2$ ) along the axis of propagation. This is precisely the type of variation that is observed in Figure 6 when the microwave horn is used as the receiver. The magnitude of the undulations depends solely on the reflection coefficient at the receiving antenna and at the face of the dielectric plate. There are, therefore, two ways of reducing these undulations; first, by using a nonreflecting (perfectly matched) receiving antenna and second, by eliminating reflections from the dielectric slab plasma container.

For a more accurate description of the multiple reflections one should consider a model which explicitly contains all the major possible reflections. As an example, examine the model illustrated by Figure 7c. In this case, two separate wave components reaching the receiver after reflection are considered; the first one ( $E_{r_1}$ ) is the wave reflected by the dielectric slab container, and the second ( $E_{r_2}$ ) is the component of the wave reflected at the transmitting horn. The field at the receiving antenna is then given by

$$E_r = E_i \exp\{ik(d_1 + t + d_2)\} + E_{r_1} \exp\{ik(d_1 + t + 3d_2)\} \\ + E_{r_2} \exp\{ik(3d_1 + 3t + 3d_2)\}.$$

The power detected is

$$I_r = E_r E_r^* = E_i^2 + E_{r_1}^2 + E_{r_2}^2 + 2E_i E_{r_1} \cos 2k(d_1 + t) + \\ 2E_i E_{r_2} \cos 2kd_2 + 2E_i E_{r_2} \cos 2k(d_1 + t + d_2).$$

The first four terms of this expression are independent of the receiver position ( $d_2$ ) and thus constitute the constant factor about which the field intensity oscillates as the receiver is displaced along the axis of the propagation. In general,  $E_{r_1}$  and  $E_{r_2}$  are sufficiently small, so that

$$I_r \cong E_i^2 \left[ 1 + 2 \left( \frac{E_{r_1}}{E_i} \right) \cos 2kd_2 + 2 \left( \frac{E_{r_2}}{E_i} \right) \cos 2k(d_1 + t + d_2) \right].$$

The two reflected components of the received wave thus oscillate at the same periodicity as the receiver position ( $d_2$ ) changes along the axis of propagation. A constant phase difference exists between the two waves and is given by  $2k(d_1 + t)$ . If, by changing the transmitter position ( $d_1$ ) with respect to the dielectric plate or by changing the thickness ( $t$ ) of the dielectric slab, the phase difference between the two reflected-wave components is made such that

$$2k(d_1 + t) = (2n + 1)\pi,$$

i.e., 
$$d_1 + t = (2n + 1)\lambda/4,$$

then the power along the axis of propagation is given by

$$I_r = E_i^2 \left[ 1 + 2 \left( \frac{E_{r_1} - E_{r_2}}{E_i} \right) \cos 2kd_2 \right].$$

Furthermore, when the amplitude of the reflected fields ( $E_{r_1}$  and  $E_{r_2}$ ) are equal, no undulations are observed and the transmitting system (transmitter and dielectric slab) is then matched to free-space.

On the other hand, if the position ( $d_1$ ) of the transmitter and the thickness ( $t$ ) of the dielectric slab are such that  $2k(d_1 + t) = 2n\pi$ , i.e.,  $d_1 + t = n\lambda/2$ , then  $E_{r_1}$  is in phase with  $E_{r_2}$  and the expression for the power along the axis of propagation becomes

$$I_r = E_i^2 \left[ 1 + 2 \left( \frac{E_{r_1} + E_{r_2}}{E_i} \right) \cos 2kd_2 \right].$$

Under these conditions the magnitude of the oscillating term is maximum, and large undulations are observed when the receiver is moved away from the dielectric slab. Therefore if  $d_1 + t$  is changed by  $\lambda/4$ , then the undulations should pass from a maximum value to a minimum value or vice versa. This is illustrated in Figure 8, where the thickness ( $t$ ) of the dielectric slab is changed. For these measurements the cylindrical container was replaced by dielectric plates of various thicknesses. It is seen that, as expected, the magnitude of the undulations pass through maxima and minima when the thickness of the dielectric plate is increased by a quarter wavelength. One can thus

eliminate a major portion of the multiple reflections by selecting a container thickness which is an integral number of half-wavelengths in optical thickness.

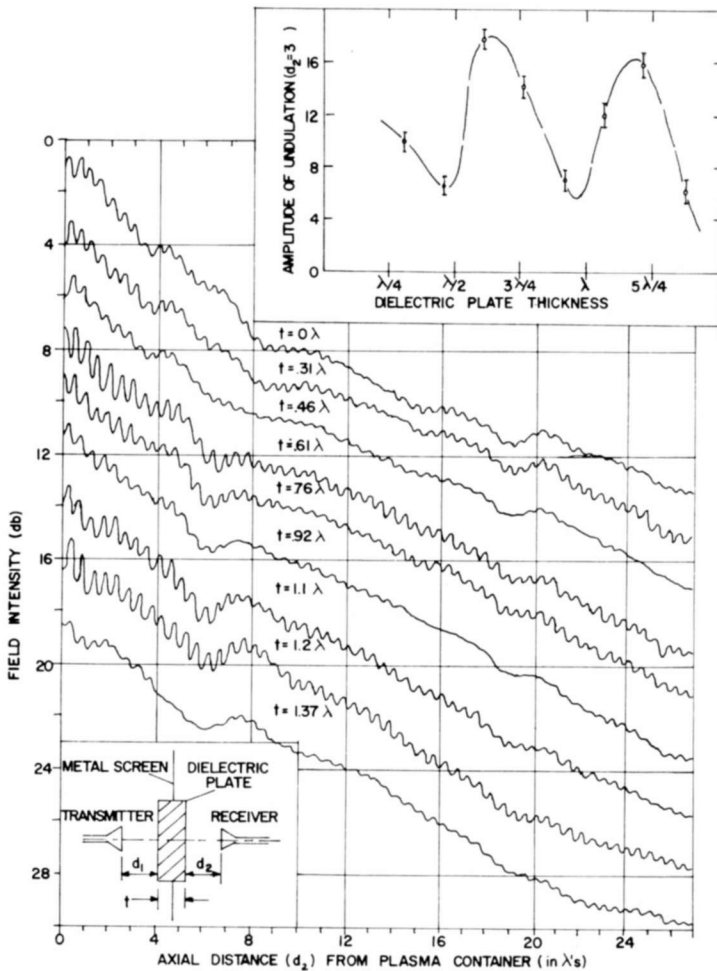


Fig. 8—Series of measurements of power received as function of receiver position illustrating the matching of the transmitting system by changing the thickness of the dielectric slab.

### Microwave System Containing Transmitting and Receiving Lenses

It is possible to achieve the conditions of plane-wave propagation (and thus facilitate the interpretation of microwave measurements in the presence of a plasma) through the use of microwave lenses. For

experiments with such an arrangement the transmitting system was formed by a source located at the focus of an 8-inch-diameter microwave lens. Another lens identical to the transmitting lens was located on the receiving end. Both lenses were located on the axis of the plasma container and 8 inches from the container. The receiving feed

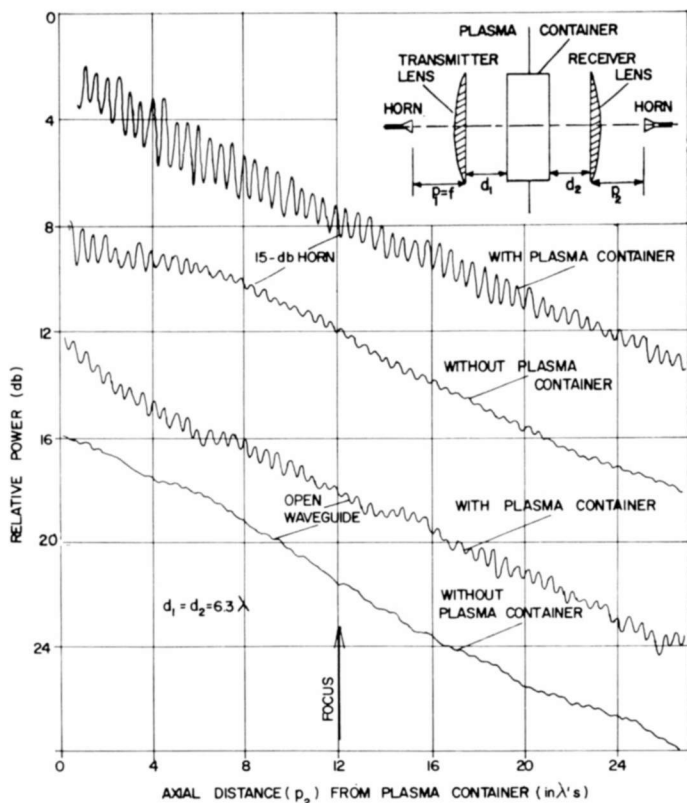


Fig. 9—Axial field intensity around the focus of the receiving lens with and without the plasma container. The two top curves were obtained using the 15-db-gain horn as the receiver, the lower curves were obtained using an open waveguide.

was moved along the axis of propagation of the system and the field intensity was measured as function of the position of the receiving feed.

Figure 9 shows two sets of measurements obtained when using a 15-db-gain horn and an open waveguide as the receiving feed. For each feed type a measurement was obtained with and without the plasma container in the plane (metal screen) separating the transmitting and receiving systems. The same precautions in regards to

avoiding stray scattering apply as before. The diffraction field is of a completely different behavior than in the case with no lenses, and varies only gradually with receiver position. The source directivity does not influence the nature of the diffraction field and only the mismatch of the source, giving rise to multiple reflections, is a major consideration. It is seen that the dielectric container does not appre-

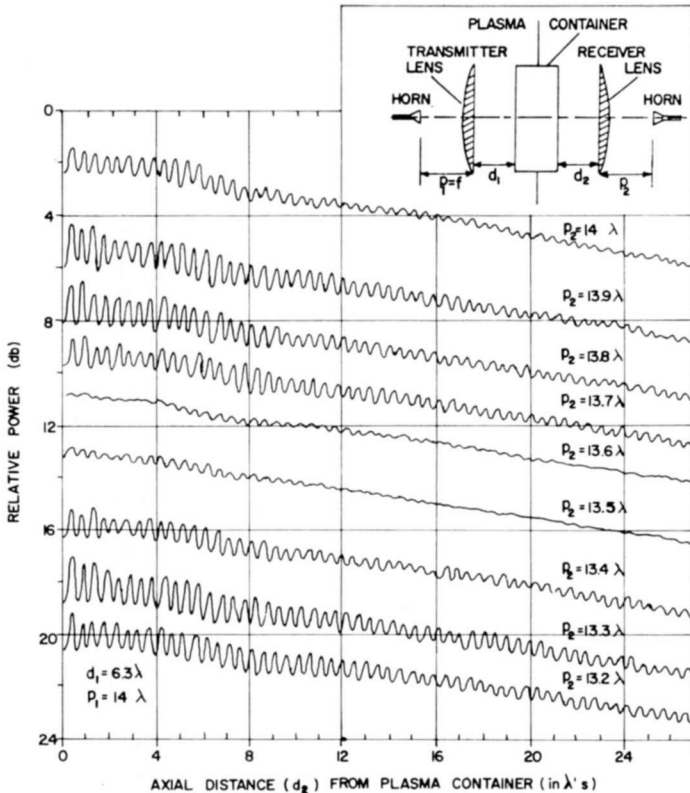


Fig. 10—Field intensity as a function of the axial position of the receiving lens system for various positions of the receiving feed with respect to the receiving lens.

ciably affect the field intensity variation around the focus of the receiving lens except for the multiple reflections that produce the regular undulations.

When using microwave lenses, multiple reflections may be more serious than without lenses since one deals essentially with plane waves and since additional reflecting surfaces are added to the microwave transmission system by the presence of the dielectric lenses. Figure 10 shows a series of measurements of field intensity as function of the

position of the receiving-lens system for fixed distances ( $p_2$ ) between the receiving horn and the receiving lens. It is noted that the amplitude of the undulations passes from a maximum value to a minimum value by changing the distance between the receiving horn and the receiving lens. Also, the amplitude of the undulations passes from a maximum value to a minimum value by changing the distance of the receiver from the lens by a quarter-wavelength.

The interpretation of these results can be demonstrated as before by examining the various components of the incident plane wave reaching the receiver after reflections at different planes in the system. The presence of lenses in the microwave system introduces an additional source of reflection for the sampling signal. It is possible to reduce the reflections at the lens surfaces by adding quarter-wave matching plates to the lenses. Two such matching plates were made of polystyrene, following the design proposed by Morita and Cohn.<sup>14</sup> These plates were placed against the flat face of the semiconvex lenses. The reflections from the curved surface of the lens facing the feed are negligible since the energy emerging is then not reflected back into the feed. The effectiveness of the matching plates is illustrated by the curves of Figure 11, where the field intensity as function of the position of the receiving lens system is shown for the lenses with and without the matching plates. The cases where a 15-db-gain horn and an open waveguide are used for the feeds are illustrated.

When the lenses are properly matched to free space, it is no longer possible to eliminate the undulations due to reflections from the lenses by adjusting the distance  $p_2$  between the receiver and the lens. This situation is illustrated in Figure 12, where the field intensity is plotted as function of the position of the receiving lens system for various values of  $p_2$ . It is seen that changes in the receiver-to-lens distance have little effect on the field measured along the optic axis. These curves should be compared with those of Figure 10, which were obtained without the matching plates against the lenses.

### ***Microwave System Consisting of Transmitting Lens and Receiving Horn***

A third possible arrangement for a microwave system consists of a lens launching a plane wave and a microwave horn acting as the receiver. The alternative arrangement of a transmitting horn and a receiving lens represents an equivalent situation.

---

<sup>14</sup> J. Morita and S. B. Cohn, "Microwave Lens Matching by Simulated Quarter-Wave Transformers," *Trans. IRE PGAP*, Vol. 4, p. 39, 1956.

Some measurements have been carried out to examine the field intensity as determined by a receiving horn when the plasma container was illuminated by a plane wave launched with a microwave lens. The variation of the power received as a function of the position of the receiving horn is shown in Figure 13 for three types of receivers —

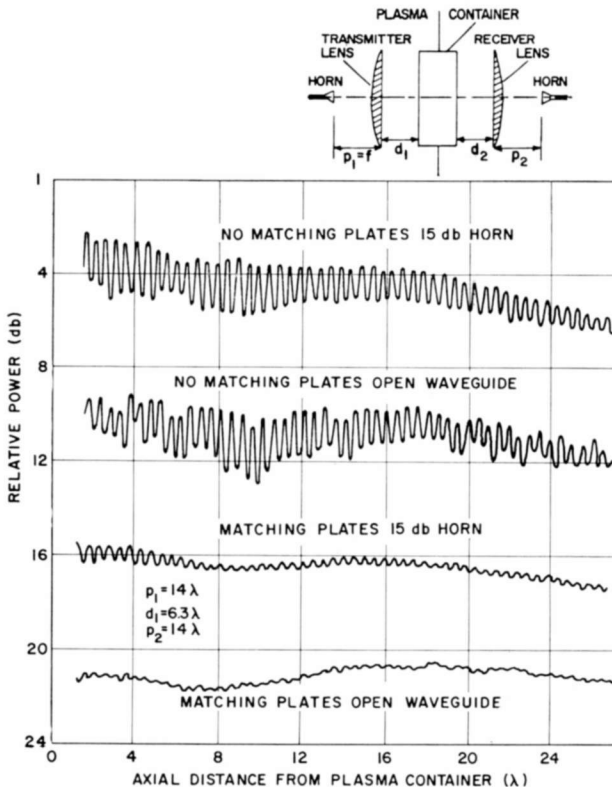


Fig. 11—Field intensity as a function of position of the receiving lens system with and without matching plates on the microwave lenses.

a short 15-db horn, a long tapered 15-db horn, and an open waveguide. The regular undulations due to multiple reflections through the system are seen to decrease in amplitude when using an open waveguide or a well-matched horn instead of the short 15-db horn. The undulations can be reduced by using the technique described above. The variation of the field intensity along the axis can be predicted using diffraction theory.

The power variation observed with a horn as the receiver and a microwave lens as the transmitter is very similar to that obtained above when horns were used both as transmitter and as receiver. In fact the situation discussed here is a limiting case of the two-horn arrangement when the transmitting horn is far removed from the

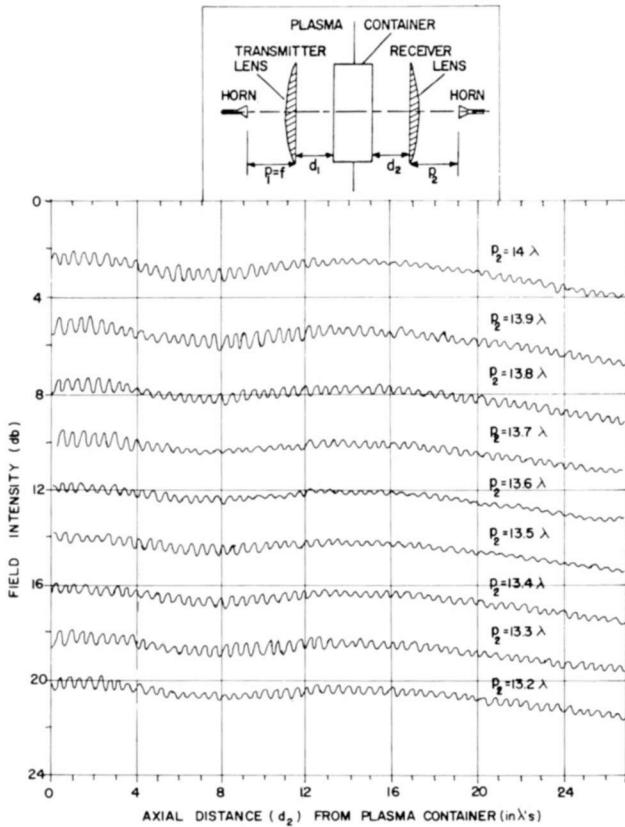


Fig. 12—Field intensity as function of the axial position of the receiving lens (with matching plates) system for various positions of the receiver with respect to the receiving lens.

diffracting aperture ( $R = \infty$ ). In the arrangement discussed here the refractive defocusing when the plasma is present should be small, since an essentially plane wave is propagating through the plasma.

FREE-SPACE MICROWAVE MEASUREMENTS IN THE PRESENCE OF PLASMA

The preceding section describes the effects due to the measurement

systems and the techniques for avoiding or minimizing these effects in order to be able to make meaningful measurements of plasma properties.

The "optimum" arrangements were then used to study the transmission and reflection of electromagnetic waves by a slab of plasma.

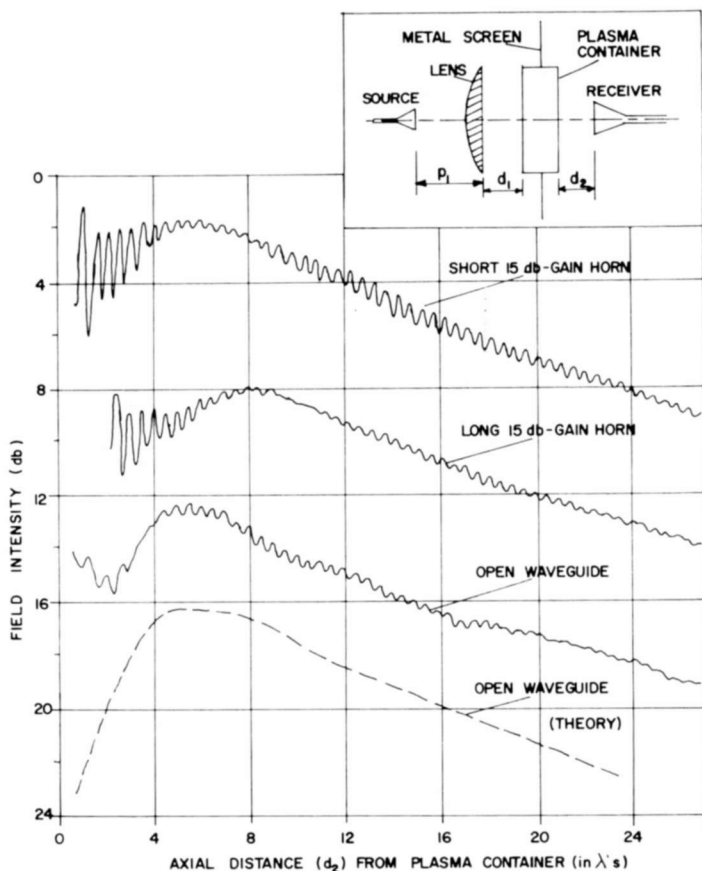


Fig. 13—Field intensity as function of the axial position of the receiver for different types of receiving antennas.

A comparison of the results obtained with each system in the presence of the plasma was made in order to ascertain the best arrangement for determining the properties of the plasma.

#### **System Mismatch in Presence of Plasma**

As indicated earlier, multiple reflections or "matching" has a pro-

found effect on the measurements. It is, therefore, instructive to show some of the "typical" effects of mismatch in the presence of plasma which will assist in the understanding of the measurements made with the various systems. Figure 14a shows the transmission of a wave through a plasma generated in helium at a pressure of 0.85 torr. The signal undergoes the expected phase shift, but the amplitude of

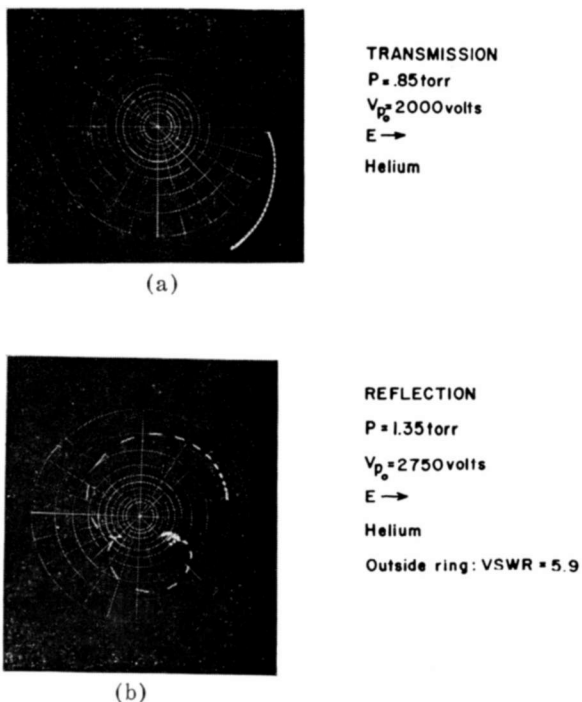


Fig. 14—Typical microwave measurements of plasma properties: (a) transmission of waves through plasma showing enhancement of received signal as plasma builds up, and (b) reflection of waves from a plasma showing cusp behavior.

the transmitted signal *increases* as the plasma density builds up. The plasma thus acts as an apparent amplifying medium. As we shall see, the plasma is *matching* the experimental microwave system to the plasma container and hence the increased signal. A "typical" experimental measurement of reflection of a microwave signal incident on a slab of plasma is shown in Figure 14b. The most noteworthy feature of these reflections are the cusps that occur as the plasma density builds up. These cusps are due to internal reflections within the microwave system that can occur in the presence of the plasma and vary in intensity with the system. From the above two examples, purposely chosen to show pronounced effects, it is apparent that the

interpretation and indeed the measurement of plasma properties by free-space microwave techniques is not as straightforward as it might at first seem. A careful assessment of the measurement system used with respect to the meaningful results that can be interpreted from the experimental values is then vital before any degree of precision

### HELIUM

$$P(\text{torr}) = .86$$

$$f(\text{cps}) = 9.265 \times 10^9$$

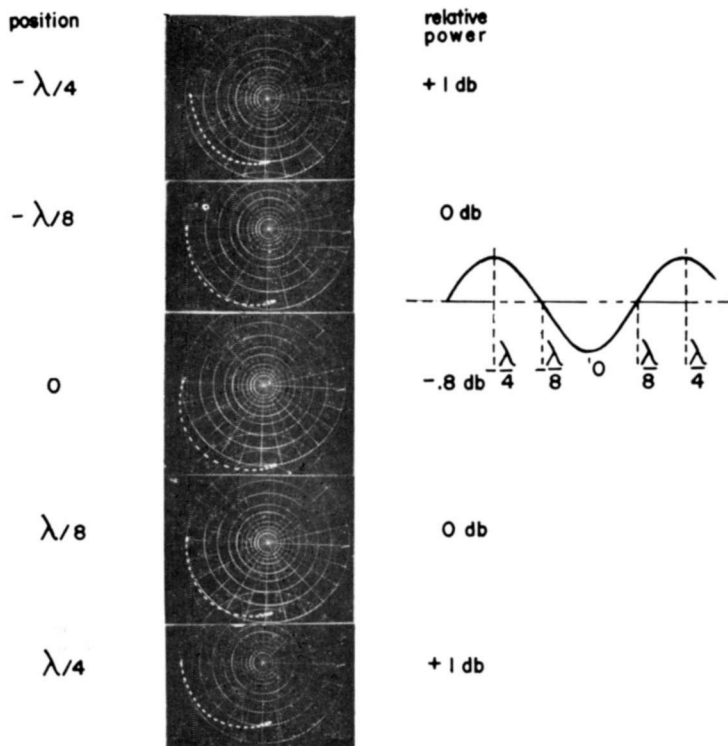


Fig. 15—Microwave transmission measurements made on a helium plasma. The distance between transmitter lens and receiver lens is held fixed, but the plasma container is moved by increments of  $\lambda/8$ . The relative power should be adjusted by the indicated increments to give the total power measured.

can be attributed to the values of plasma parameters determined in this way. A detailed indication of this "matching" problem for transmission of electromagnetic waves through a plasma is shown in Figure 15, in which the same plasma has been generated in each case but the location of the transmitting lens (and horn) and the receiving lens

(and horn) have each been displaced by  $\lambda/8$  in such a way as to keep the distance between transmitting lens and receiving lens fixed. As can be seen, when the system is arranged so that the conditions with no plasma are such that maximum power is received (the  $\pm\lambda/4$  positions), the presence of the plasma causes the attenuation to increase slightly more rapidly than would be the case if the plasma were perfectly matched. Conversely, when the system is arranged so that minimum power is received with no plasma (the 0 position), then the presence of the plasma tends to "match" the system, resulting in an initial increase in power as the plasma builds up. At the intermediate median positions ( $\pm\lambda/8$ ) a more realistic variation is observed. The major point to note is that the system mismatch does *not* affect the phase change introduced by the plasma (and hence has little effect on the determination of total electron density) but it does affect the attenuation and hence any estimate of collision frequency. One must, therefore, ascertain the match of the microwave systems to the plasma container in order to make a proper interpretation of the measurements in the presence of the plasma.

#### ***Comparison of Various Microwave Arrangements for Measurement of Plasmas***

Transmission measurements performed when the transmitting horn is against the plasma container and the receiving horn is  $5\lambda$  from the container are shown in Figure 16a. Large cusps appear in the traces, indicating significant multiple reflections in the presence of the plasma. There is a significant difference between measurements performed when the incident electric vector is parallel to the metal electrodes in the plasma container and measurements performed when the incident electric vector is normal to the electrodes. More will be said of these measurements when they are compared to the results obtained with the other arrangements.

Transmission measurements made with the transmitting horn  $5\lambda$  from the plasma container and the receiving horn  $17\lambda$  from the plasma container are shown in Figure 16b. Less phase shift and greater attenuation than for the previous measurements are apparent. This would be expected on the basis of refractive defocusing<sup>12</sup> by a slab of plasma when a spherical wave is incident on the plasma. Again there is a strong dependence on the orientation of the incident electric field relative to the electrodes. This is attributed to reflections taking place from the electrodes, the phases of which differ by  $180^\circ$  for the two polarizations of the incident field. (An unsymmetric distribution of plasma would produce a similar effect.)

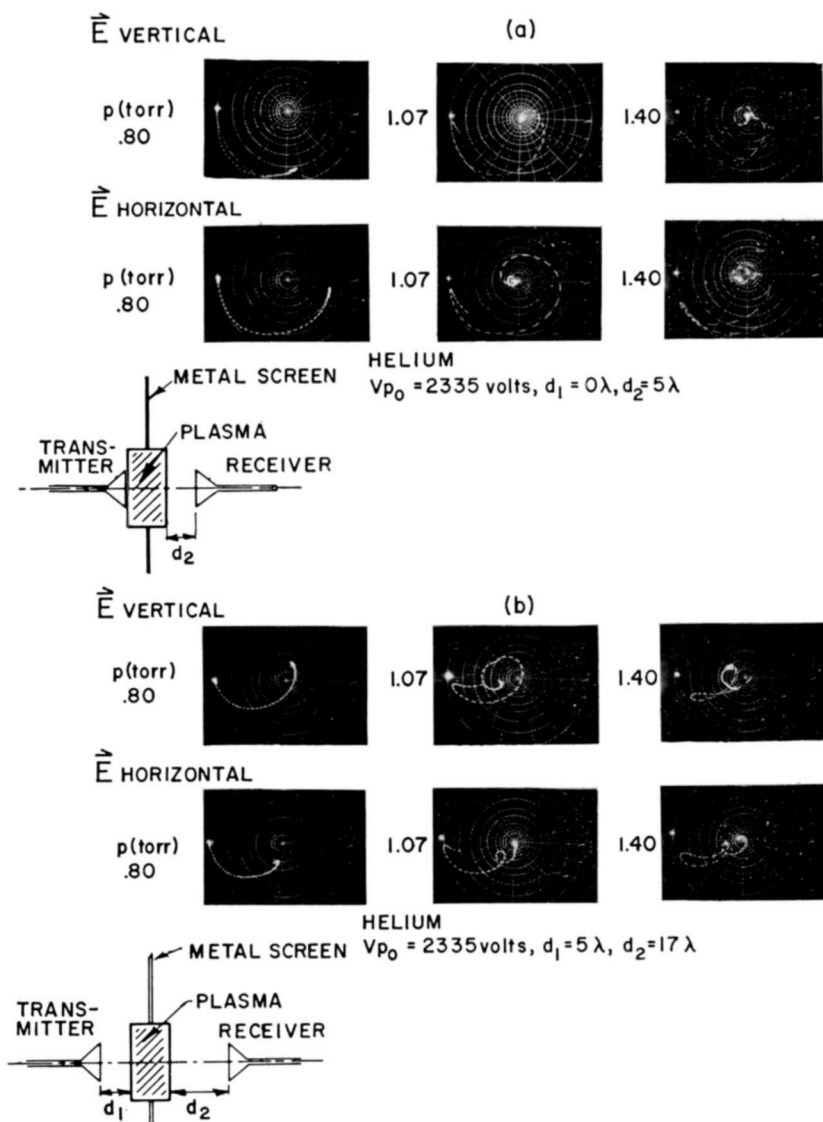


Fig. 16—Series of microwave transmission measurements made on a slab of plasma generated in helium using a microwave system consisting of transmitting and receiving horn antennas located (a) near the plasma container and (b) some distance from the plasma container.

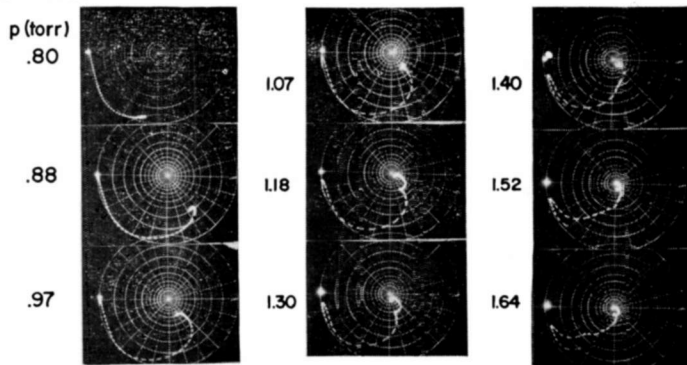
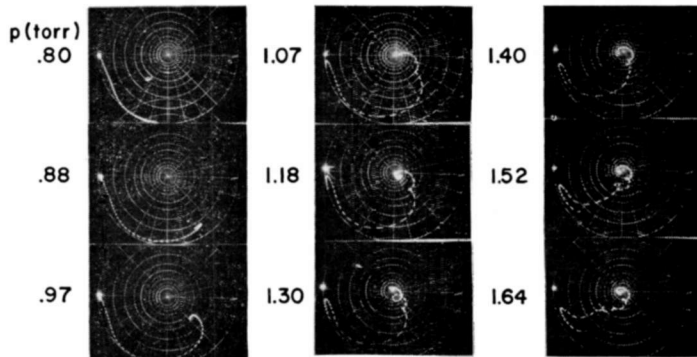
When lenses are used in both the transmitting and receiving portions of the system, then, as shown in Figure 17a, there is no dependence on the incident field orientation or polarization; both series of measurements give essentially the same result. In addition, the appearance of cusps is markedly reduced, and these appear only when the plasma is quite dense (corresponding to multiple reflections originating from the plasma). The flat walls of the plasma container are approximately one wavelength in optical thickness and therefore are matched to free space. However, when a plasma is present, multiple reflections can occur from the plasma boundaries. These reflections depend on the plasma conditions, and increase in amplitude as the plasma density approaches the cutoff condition.

The dependence on the location of the receiving lens was demonstrated by a series of measurements performed with the receiving lens against the plasma container, removed  $6.5\lambda$  from the plasma container and again removed  $12.7\lambda$  from the plasma container. (In each case the receiving horn was located at the focus of the receiving lens.) The results are shown in Figure 17b and show no significant differences between the three distances, indicating that the plasma appears uniform to an incident plane electromagnetic wave over the range of parameters investigated.<sup>12</sup> At the higher pressures ( $p > 1.4$  torr) the attenuation is so great that slight changes in the received power levels would be difficult to ascertain with any degree of precision.

We thus see that different results are obtained for the same plasma, the measurements being strongly influenced by the experimental measurement system. For a horn (or point) source, refractive defocusing effects appear that cause a reduction in the measured amplitude of the fields. Strong multiple reflections result in cusps in the measured traces (particularly when the source and receiver are near the plasma) that significantly alter the measurements. Finally, reflections from the electrodes have a major effect on an incident spherical wave, resulting in a strong dependence of the measurements on the orientation of the incident fields relative to the electrodes.

These effects can be eliminated or minimized by using an incident plane wave through the use of auxiliary lenses on both transmitting and receiving portions of the measurement system. The refractive defocusing (due to a uniform slab of plasma) is eliminated as are the polarization effects of the orientation of the incident fields relative to the electrodes. The effect of multiple reflections, although not completely eliminated, is greatly reduced and is present only as the plasma becomes relatively dense.

These remarks are substantiated by Figure 18, which shows a series

$\vec{E}$  VERTICAL $\vec{E}$  HORIZONTAL

HELIUM

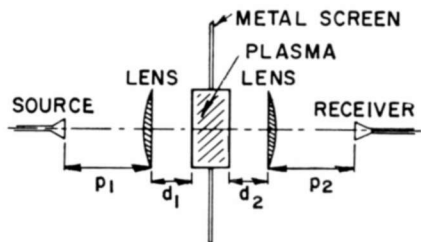
 $V_{p0} = 2335$  volts,  $p_1 = 14.7\lambda$ ,  $p_2 = 14.7\lambda$ , $d_1 = 6.3\lambda$ ,  $d_2 = 6.3\lambda$ 

Fig. 17(a)—Series of microwave transmission measurements made on a slab of plasma generated in helium using a microwave system consisting of transmitting and receiving microwave lenses.

of reflection measurements with the same arrangement of the transmitting sections of the microwave systems as in the previous transmission measurements. In all cases the reflections are small for the discharges at low pressures corresponding to a very dilute plasma. As the electron density increases (corresponding to higher pressures)

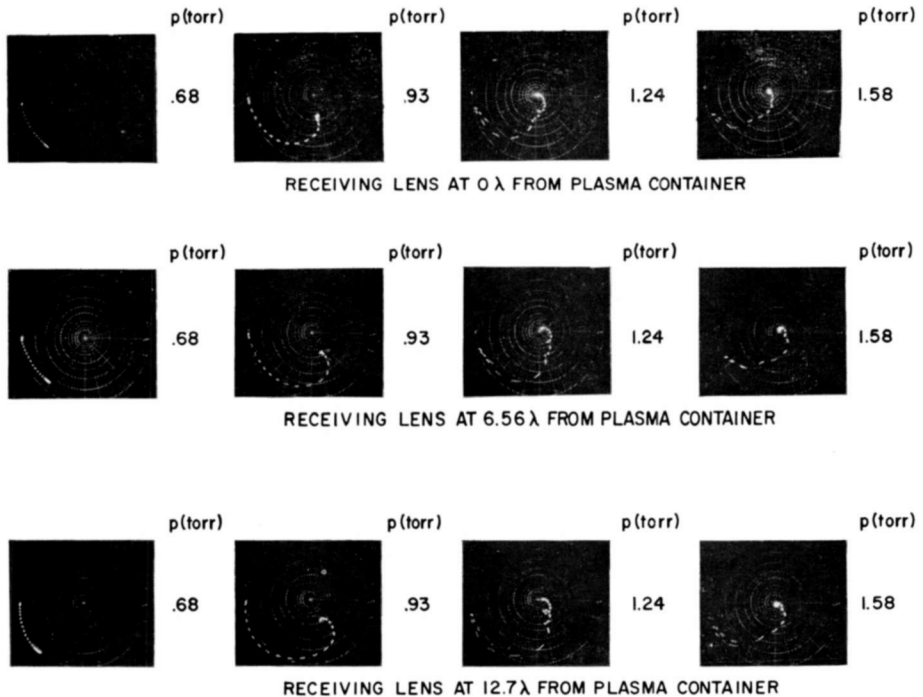


Fig. 17(b)—Microwave transmission measurements made on a helium plasma for various locations of the receiving lens from the plasma container. The outer ring equals 0 db and the calibration between lines is 2 db.

the reflections become more serious. The largest reflections occur for the microwave transmitting horn against the plasma container. Similarly, the appearance of violent cusp configurations of the trace as the plasma builds up is most pronounced for this case. A difference between the two polarizations (incident electric field normal to the electrodes and incident electric field parallel to electrodes) exists although it is not as marked as for the corresponding transmission measurements. When the transmitter horn is moved a distance  $5\lambda$  from the plasma container, the above effects are still present but to a reduced degree. Thus by moving the transmitting antenna away from the plasma the influence of the multiple reflections is somewhat

reduced. The lens system again appears to be most reliable, showing only small differences between the two polarizations and significantly less mismatch than the other microwave arrangements.

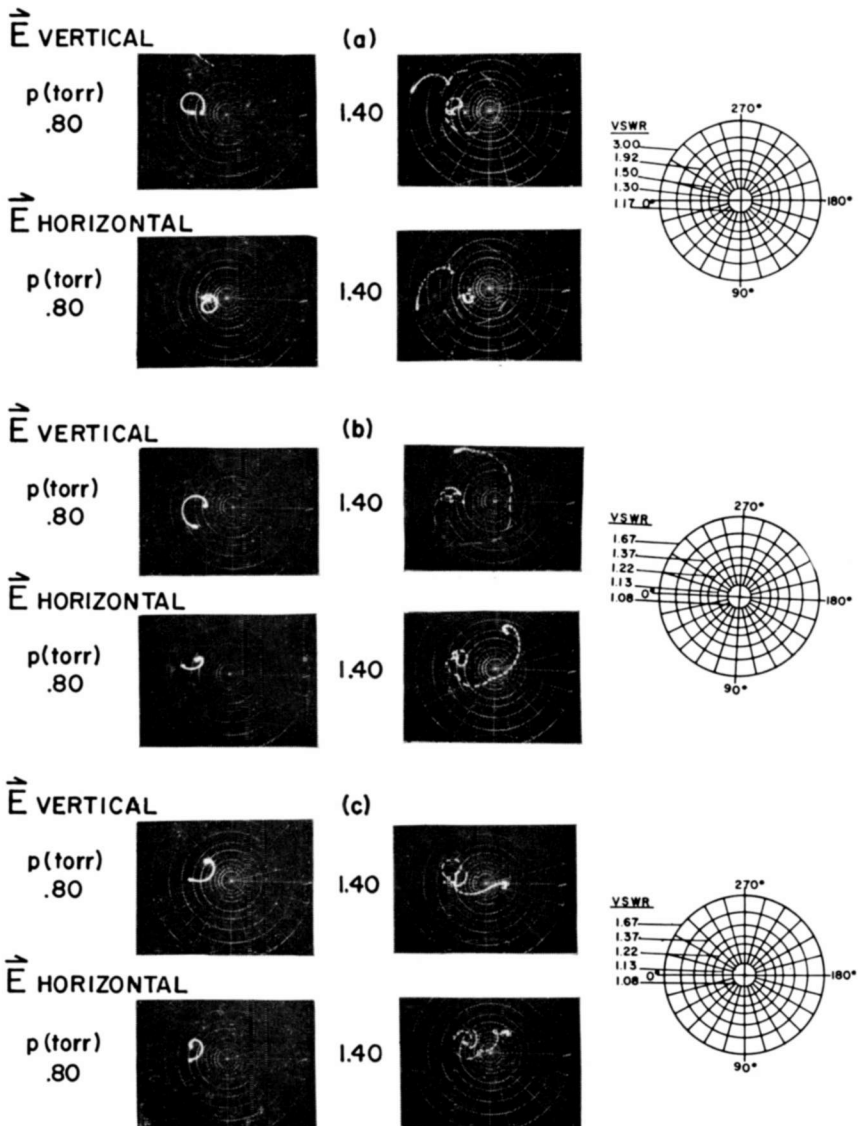


Fig. 18—Microwave reflection measurements made on a slab of plasma generated in helium using a microwave system consisting of (a) transmitting and receiving horn antennas located near the plasma container; (b) transmitting and receiving horn antenna located some distance from the plasma container; and (c) transmitting and receiving microwave lenses.

Figure 19 shows measurements made when energy in a parallel beam (through the use of lenses) is incident on the plasma and the receiver is a simple antenna. In this arrangement a lens is used on the transmitting portion of the microwave arrangement but not on the receiving end. A comparison between use of an open waveguide as

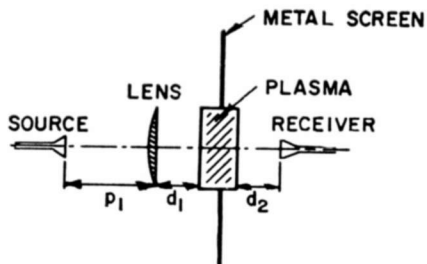
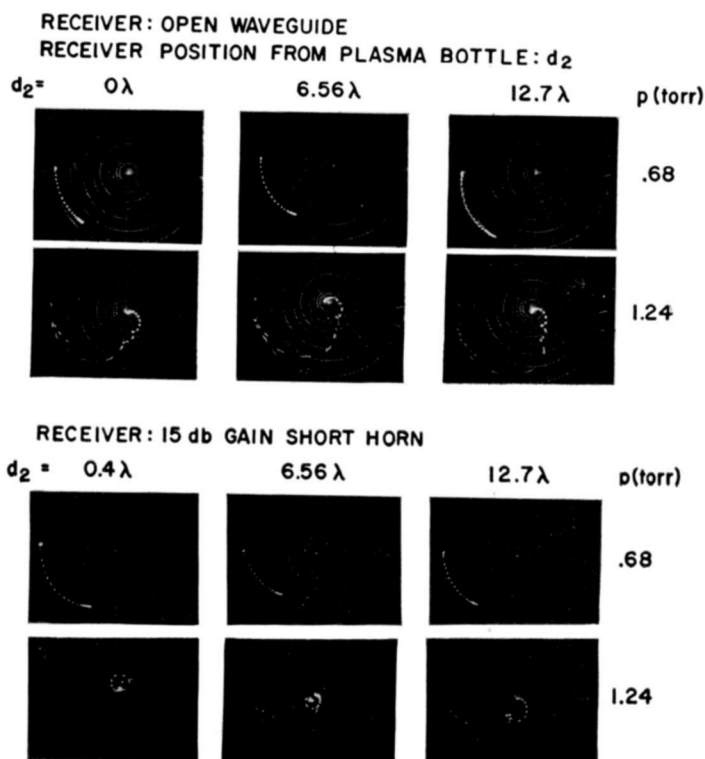


Fig. 19—Microwave transmission measurements made on a helium plasma using a microwave system consisting of a microwave lens on the transmitting portion and an open receiver.

receiver and use of the short 15-db-gain horn as receiver is shown for a helium plasma generated at various pressures and for various receiver locations from the plasma container.

With the open waveguide used as a receiver (Figure 19a) there is little dependence on distance of the receiver from the plasma. In addition, the measurements compare very well with the results obtained with an auxiliary lens on the receiving portion of the microwave arrangement (Figure 17a). Thus for measurements of transmission of r-f energy through a plasma when the incident field is a plane wave, an open waveguide receiver (or any omnidirectional receiver that is well matched to free space) can be used and will give the same results as when a lens is used as the receiving antenna.

When a directive receiver that can give rise to significant reflection (not too well matched to free space) is used to measure the transmission of waves through a plasma, then the location of the receiver has a significant effect on the measurements. As seen from Figure 19b, when the receiver is near the plasma container, significant multiple reflections can occur between the receiving antenna aperture and the plasma, resulting in violent cusps in the measurements and in erroneous values for the amplitude and phase of the wave transmitted through the plasma. As the distance between the plasma container and the receiving antenna is increased, the measurements approach more and more those obtained with an open-waveguide receiver or a lens receiver. It is not until the receiver is more than  $12\lambda$  from the plasma container that the measurements approach the open waveguide or lens values, and even then they show more pronounced cusps due to the multiple reflections. Thus if the receiving antenna is not very well matched to free space or if its match is uncertain, it is necessary to use a lens on the receiving portion of the microwave arrangement if reliable measurements of the plasma are to be performed.

Thus of the three systems, only the lens arrangement appears to be acceptable for measuring plasma properties by free-space propagation of electromagnetic waves through a plasma of slab configuration. In the case of a cylinder of plasma illuminated broadside, lenses can be used to focus the incident beam and hence eliminate refractive defocusing effects.<sup>12, 15</sup>

---

<sup>15</sup> S. Shiobara, S. Miyoshi, and Y. Sakamoto, "Microwave Free-space Method for Plasma Diagnostics," *Jour. Phys. Soc. Japan*, Vol. 18, p. 1341, 1963.

## CONCLUSIONS

Three experimental microwave arrangements—a simple source and receiver, a lens transmitter and lens receiver system, and a lens transmitter with a simple receiver—have been studied at X-band frequencies for application to measurement of the properties of a plasma in the configuration of a finite slab. The effects of stray scattering of electromagnetic energy, diffraction, source of directivity, plasma container, and multiple reflections have been examined in detail for each arrangement. The experimental effects are in some cases of such magnitude as to predominate over the plasma effects, and hence their influence must be either eliminated or minimized in order to make quantitative measurements of the plasma properties. From the measurements on the experimental arrangements, the optimum configurations could be determined and used to study transmission and reflection of electromagnetic waves by a slab of plasma in order to ascertain the best arrangement for measuring the properties of plasmas.

Different results are obtained for the same plasma for each of the three arrangements, the measurements being strongly influenced by the measurement system even in the optimum arrangement. Only the lens-transmitter-lens-receiver system, when used with suitable precautions, appears to be acceptable for measuring the properties of a plasma in the configuration of a slab by free-space propagation of electromagnetic waves.

Measurements obtained by different arrangements should be treated with some caution. A thorough understanding of the effects introduced by the microwave measuring system is essential before a quantitative interpretation of plasma properties can be made from free-space microwave measurements.

## ACKNOWLEDGMENT

The authors are indebted to Mr. B. W. Gibbs for developing much of the experimental apparatus and for conducting most of the measurements.

# A PHOTOCONDUCTIVE THERMOPLASTIC RECORDING SYSTEM

BY

N. E. WOLFF

RCA Laboratories  
Princeton, N. J.

*Summary*—The discovery that polymer-soluble organic photoconductors make excellent electrophotographic layers that are essentially transparent and grainless has led to a thermoplastic recording system that does not require a vacuum. By combining the properties of photoconductivity and thermoplasticity in a single homogeneous medium, it has been possible to produce layers that handle optical input and output to give good quality schlieren projection images. Sensitization over a wide range of the visible spectrum is possible.

## INTRODUCTION

THE interaction of electrostatic charges with deformable insulating layers has a long history.<sup>1</sup> The *Eidophor*<sup>2</sup> system utilized this interaction for the formation of an image. Here a liquid film of the proper viscosity is charged by an electron beam in vacuum. The beam lays down variable charge densities corresponding to the image information. The viscosity of the medium is such that the electrostatic forces will deform the layer at *room temperature*. The resistivity of the film can be adjusted to restore the original surface after, say, a frame time for television applications.

More recently a recording system was described by Glenn<sup>3</sup> who substituted a thermoplastic film for the oil film. Here it is necessary to apply *heat* to the insulating film to attain the proper viscosity for deformation. The image can be "frozen" by quick cooling for permanency, although reheating will erase the picture due to thermal charge dissipation.

---

<sup>1</sup> J. W. Swan, "Stress and Other Effects Produced in Resin and in a Viscid Compound of Resin and Oil by Electrification," *Proc. Roy. Soc. (London)*, Vol. 62, p. 38, 1897.

<sup>2</sup> For a complete bibliography see E. I. Sponable, "Eidophor System of Theater Television," *Jour. of the SMPTE*, Vol. 60, p. 337, Apr. 1953, and E. Baumann, "The Fischer Large Screen Projection System," *ibid.*, p. 344.

<sup>3</sup> W. E. Glenn, "Thermoplastic Recording," *Jour. of Appl. Phys.*, Vol. 30, p. 1870, Dec. 1959.

Both these schemes require a vacuum, since the variable charge densities corresponding to the image information must be put down with an electron beam. The elimination of the vacuum for image recording and a means of providing a direct optical input to the thermoplastic layer seemed desirable.

In a previous publication,<sup>4</sup> H. G. Greig described an organic photoconductive system that could be processed by standard electrophotographic techniques. It was also pointed out that, in addition to providing charge storability, transparency, and photoconductivity, it was possible to incorporate into such electrophotographic layers the thermoplastic properties necessary for processing a recording medium suitable for schlieren projection. The present paper describes a novel embodiment of such an image-recording system.

### EXPERIMENTAL PROCEDURE

Figure 1 shows the steps necessary for recording on photoconductive thermoplastic layers. The coating, Figure 1(A), is the heart of the system and will be described in detail. There are many useful transparent conductive layers such as evaporated gold, copper, and conducting tin oxide. Layer 2 can also be made reflective (evaporated aluminum), or it can be an integral part of the substrate, 3, if a reflective readout of the final image is desirable. In the latter case, the substrate is a metal such as aluminum. For a transparent substrate, glass or a polyester film base is preferred. Figures 1(B) through (E) show the process steps necessary to obtain a ripple image for schlieren projection. While negative corona charging is shown in (B), it is equally feasible to use positive charging, or double corona charging in the absence of a conductive layer between the substrate and the photoconductive thermoplastic layer.

Exposure is done by projection or contact from a photographic transparency. To obtain gray scale it is necessary to use a line screen or half-tone dot pattern. The results shown in Figure 6 were obtained with a line pattern of approximately 20 lines per mm. There are two ways of screening the image:

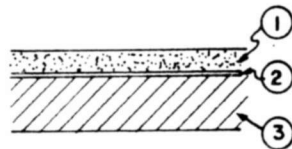
- (1) *Sequential Screening*—A first exposure of the charged layer to the line pattern produces alternate lines of charge and no charge. A second exposure to a negative transparency results in dark areas (discharged, black in schlieren projection, no ripples) and in highlights (the charged alternate line pattern)

---

<sup>4</sup> H. G. Greig, "An Organic Photoconductive System," *RCA Review*, Vol. XXIII, p. 413, Sept. 1962.

where no further exposure occurred. Likewise, a positive transparency can be used to provide a negative projected image.

- (2) *Single Exposure*—A line screen pattern in contact with a negative transparency results in a ripple pattern only where the original scene was dark. If a positive transparency is used, ripples are formed in areas corresponding to the original high-lights. The black areas have no ripples and are charged.



1. Transparent photoconductive and thermoplastic coating
2. Transparent or reflective conductive coating
3. Flexible or rigid transparent substrate

(A)

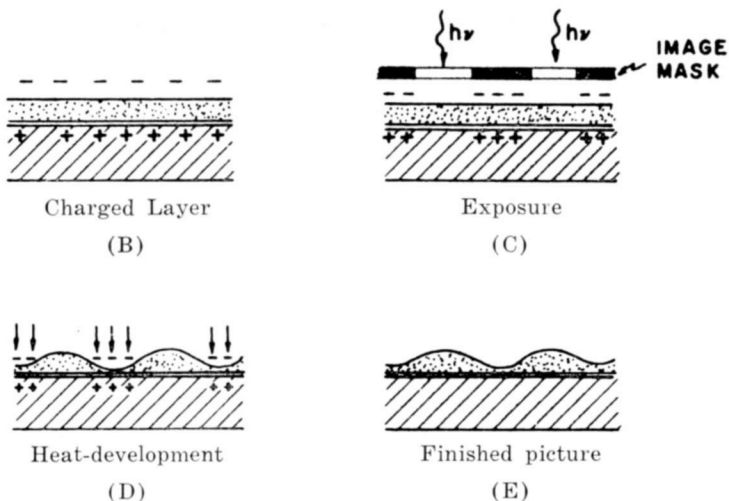


Fig. 1—Photoconductive thermoplastic recording process.

It is also possible to prepare a single screened transparency for the exposure. In this case it is best to make a screened negative. Solid black areas can be either charged or uncharged for schlieren projection (no ripples). It is preferable to have them uncharged, since there is

less of a chance to pick up dust, which will show as bright spots if embedded during subsequent heat development.

Development of the image can be accomplished in many ways. It is only necessary to raise the temperature of the thermoplastic layer sufficiently so that its viscosity is low enough for deformation by electrostatic forces. Once the image is formed, the layer should be cooled quickly, so that thermal charge decay will not destroy the image. For erasure, prolonged heating is necessary so that the surface tension

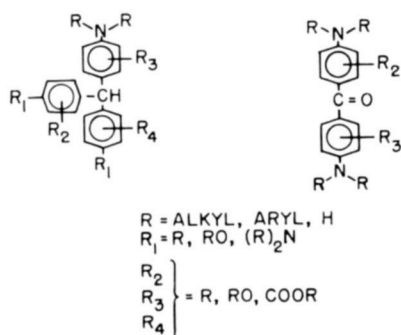


Fig. 2—Leucobase compounds for photoconductive system.

of the thermoplastic layer can restore flatness after all charges have leaked off. Filtered hot air has been found useful for developing images. Here the airflow is controlled by a shutter. Other means of heating are by contacting the substrate (stationary or dynamic) to the heat source or by resistive heating of the conductive backing. Time and temperature required depend entirely on the specific layer used.

## MATERIALS

Photoconductive thermoplastic layers that have been used successfully closely resemble the layers described previously.<sup>4</sup> The type of organic photoconductors that have been investigated are illustrated in Figure 2. Almost all of them are colorless compounds that absorb in the ultraviolet and hence have a restricted sensitivity. They can, however, be readily sensitized. It has been found that these photoconductors will perform in almost any organic dielectric medium, provided they are sufficiently soluble in that medium and that the medium has a sufficiently high dark resistivity. Since the photo-

current increases exponentially with concentration of the photoconductor in the dielectric medium,<sup>5</sup> it was desirable to select a material that would readily dissolve large amounts of the photoconductor and, at the same time, have useful thermoplastic properties for image formation. Several types of polystyrene of an average molecular weight between 20,000 and 30,000 have given good results. Of the nonpolymeric dielectrics, sucrose benzoate has been found to be a good medium, since it forms a glass on cooling. Typically, a concentration of 20 to 50% by weight of the photoconductive compound in the thermoplastic layer was used. In some instances it has been found useful to add a small amount of a halogenated polymer or compound to the layer. This provides a source of halide for the formation of trace amounts of dye by oxidation of the original photoconductor.

#### SENSITIVITY AND SPECTRAL RESPONSE

It was pointed out that the photoconductive compounds by themselves exhibit photoconductivity only in the ultraviolet. Typically, the leucobase of malachite green, bis(4,4'-dimethylaminophenyl)-phenyl methane has absorption peaks at 2080 Å and 2640 Å. However, this compound can be readily transformed into the cationic dye malachite green by a simple oxidation reaction in the presence of an anion. Even under the most carefully controlled conditions, the formation of trace amounts of this dye cannot be avoided when the photoconductor is dissolved in the dielectric matrix. This small amount of dye with its absorption peaks at 3150 Å, 4250 Å, and 6150 Å (determined in methanol) acts as a sensitizer for the leucobase photoconductor and, therefore, extends the sensitivity into the visible spectrum. A photo-response curve of a layer of 50% by weight of the leucobase of malachite green in pure polystyrene (prepared specifically for these measurements) is shown in Figure 3. This "unsensitized" layer shows the photoresponse corresponding to the absorption peaks of malachite green, though somewhat shifted in the polymer environment. In this case, about 10 ppm of dye was formed by "oxidation" resulting in dye sensitization of the layer in the visible.

Spectral response can be extended considerably by the addition of other cationic dyes. For example, layers that contain trace amounts of Auramine, Acridine Orange, and Rhodamine B have been prepared. When all three dyes are incorporated into a single layer, essentially

---

<sup>5</sup> W. Mehl and N. E. Wolff, "Transfer of Photoexcited Carriers in Organic Solid Solutions," to be published in the *Intern. Jour. of the Phys. and Chem. of Solids*.

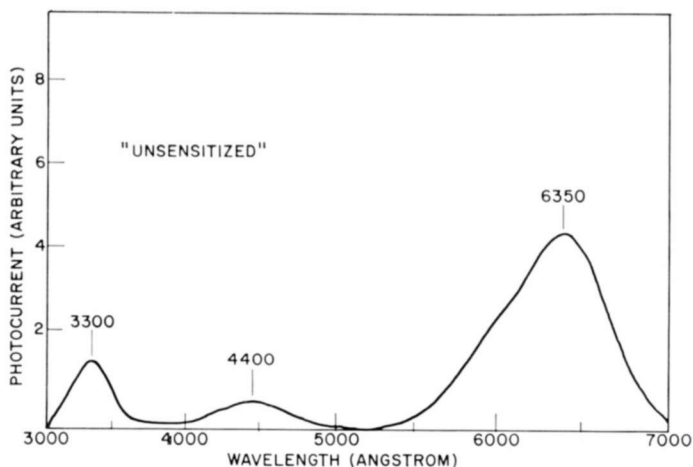


Fig. 3—Photoresponse curve of an "unsensitized" photoconductive thermoplastic layer.

panchromatic response is obtained as shown in Figure 4. In addition to the response peaks corresponding to malachite green, new peaks appear (4910 Å and 5500 Å) that are due to the presence of Acridine Orange and Rhodamine B, while Auramine increases the sensitivity at 4400 Å.

With a tungsten light source providing approximately 40 to 50 foot candles in the image plane, exposures required for good ripple forma-

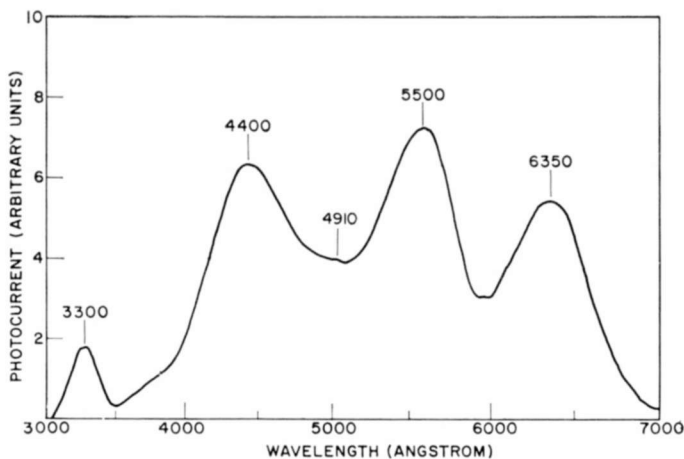


Fig. 4—"Panchromatic" response of a dye sensitized photoconductive thermoplastic layer.

tion range from 5 to 10 seconds. Yet, the same layers will give excellent toner images when exposed for 1 second or less. Since heat is used for developing an image for schlieren projection, it is important that the rate of charge decay in the dark does not increase substantially on heating. Even a small increase of the rate at deformation temperatures results in reduced sensitivity. The longer exposure time is necessary to provide sufficient difference in charges for good image definition.

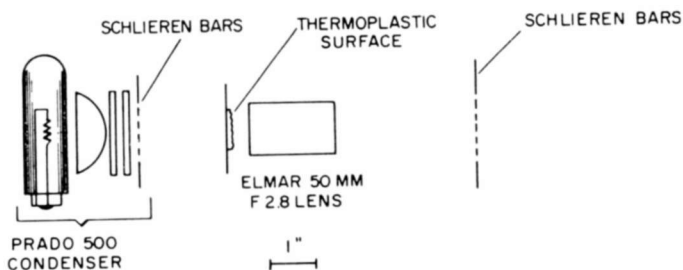


Fig. 5—Schlieren system using modified Leitz Prado 500 projector.

#### RESOLUTION AND PROJECTION

The layers are grainless and essentially transparent (85% transmission) and have shown good resolution when toner developed (150 lines/mm). The resolution is limited by the factors described by Glenn,<sup>3</sup> and also depends on the thickness of the layer. Another restriction is the resolving power of the schlieren projector used.

A simple modification of a commercial Leitz Prado 500 slide projector resulted in an adequate schlieren optical system (Figure 5). The single lens serves to image the light from the first set of schlieren bars onto the second set and, at the same time, to project the image of a slide placed between the first bars and the lens. Focusing is achieved by moving the slide with respect to the rest of the system, which is fixed. This particular projector was capable of resolving better than 24 lines/mm but not more than 118 lines/mm. This was determined with rulings placed in the slide holder. The fine ruling gave a uniform blue projected field and no longer resolved a line pattern. Ripple patterns of up to 56 lines/mm were obtained on the photoconductive thermoplastic slides. The projector can give a 100:1 contrast ratio, though the pictures averaged about 20:1. Figure 6 shows an enlargement of a photographic master (16 lines/mm) on the left and a rephotographed picture of the schlieren-projected ther-

moplastic image on the right. This image was obtained by normal processing and exposure to the master. Only the actual projected picture can demonstrate the quality of the image and particularly gray-scale rendition (8-10 steps). It is interesting to note, however, that all imperfections in the original (dark and light spots) are faithfully reproduced as dark spots.



Fig. 6—Original and projected thermoplastic image. On the left is an enlargement from the photographic screened negative master and on the right is a rephotograph of the projected thermoplastic image ( $2 \times 3$  feet) made from that master.

#### CONCLUSIONS

A novel electrophotographic layer has been described that combines the elements of photoconductivity and thermoplasticity and is entirely composed of organic materials. The input as well as the output is optical and no vacuum is required as for some other thermoplastic imaging layers. Schlieren projection gives images with adequate resolution, gray scale, and contrast. The quantum efficiency is theoretically limited to unity in corona-charged electrophotographic systems;<sup>6</sup> these new layers have shown quantum efficiencies<sup>5</sup> as high as 0.1. Dye sensitization can extend the spectral response over almost the entire visible

<sup>6</sup> H. J. Gerritsen, W. Ruppel, and A. Rose, "Photoleitfähigkeit von Zink-oxyd bei Ohmschen und Sperrenden Kontakten," *Helv. Physica Acta*, Vol. 30, No. 4, p. 235, 1957.

spectrum. It should be possible, therefore, to increase the sensitivity of these photoconductive thermoplastic layers still further.

#### ACKNOWLEDGMENT

The schlieren projection system used in this work was designed by F. H. Nicoll, whom I also wish to thank for his contribution in carrying out many of the early experiments with exposures, screening, and projection techniques using the new photoconductive thermoplastic materials. Thanks are due to H. G. Greig for his continuing efforts in providing materials useful for the system described, and also to E. C. Giaimo who contributed to the evaluation and processing of the recording system. The research reported herein was sponsored by the Aeronautical Systems Division, Air Force Systems Command, Wright-Patterson Air Force Base, Dayton, Ohio, under Contract No. AF33 (657)-7920, and RCA Laboratories, Princeton, New Jersey.

# A NEW SURFACE PHENOMENON IN THERMOPLASTIC LAYERS AND ITS USE IN RECORDING INFORMATION

BY

F. H. NICOLL

RCA Laboratories  
Princeton, N. J.

*Summary*—A new phenomenon involving the crazing of a thermoplastic layer is described. It was found that when a surface layer is added to the thermoplastic, electrostatic charging and subsequent heating of the layer to the softening point will result in deformation of the surface. An added layer only one thousandth of a monolayer of atoms is sufficient to cause the effect. Many chemical and physical methods can be used to produce the correct surface conditions. Suitable very thin layers of organic and inorganic material can be produced on the thermoplastic by deposition from solution, by vacuum evaporation, or by deposition from a beam of ions. Cross linking of the thermoplastic surface by short ultraviolet light, x-rays or electron beams can also be used to alter the surface and produce the crazing phenomenon.

Information can be recorded or images formed by utilizing either a charge pattern with a uniform surface layer or a surface-layer pattern with uniform charge. In both cases the sensitivity is high and the images are capable of high resolution and halftone reproduction. The images produced by the new phenomenon are visible by reflected light or transmitted light and they can be viewed by ordinary optical projection as well as with schlieren-type projectors. The explanation of the effect would seem to lie in the change of surface tension or melting point of the thermoplastic due to the presence of foreign atoms on the surface. It is difficult, however, to understand the exceptionally high sensitivity to the foreign atoms.

## INTRODUCTION

A NUMBER OF papers on the deformation of viscous liquids and softened thermoplastics under the influence of an electrostatic field have appeared in the literature. P. J. Cressman<sup>1</sup> has described a number of these deformations. Glenn<sup>2</sup> has demonstrated a high-density-recording system in which an electron beam in a vacuum deposits charge on a thermoplastic layer coated on a conducting substrate. When this layer is heated to the softening point, lines or dots of charge develop into deformations. In this process,

<sup>1</sup> P. J. Cressman, "New Type of Thermoplastic Deformation," *Jour. App. Phys.*, Vol. 34, p. 2327, Aug. 1963.

<sup>2</sup> W. E. Glenn, "Thermoplastic Recording," *Jour. App. Phys.*, Vol. 30, p. 1870, Dec. 1959.

large uniform areas of charge are unaffected by heat development and remain smooth up to the edge, where a disturbance occurs. Thus it is not possible to obtain halftone reproduction without the use of screening. More recently two papers have appeared<sup>1,3</sup> describing particular charging conditions that produce a frost or wrinkling on uniformly charged regions. These methods of obtaining a frosted surface were

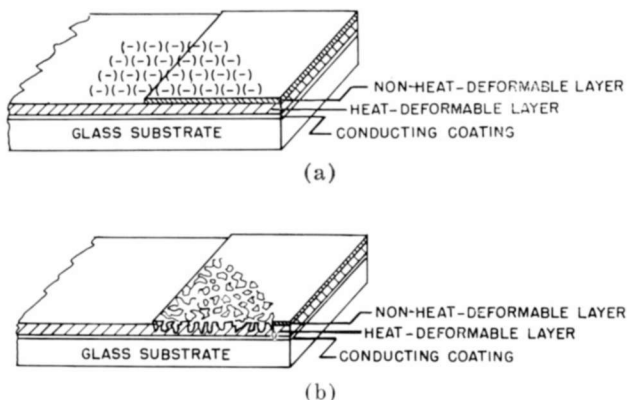


Fig. 1—Steps in processing thermoplastic layer (surface layer on right half only): (a) recording medium after charging and (b) recording medium after heat development.

also observed by the present author but, in addition, a new thermoplastic crazing phenomenon was discovered. The new phenomenon occurs after charging and heat developing of a thermoplastic layer having a special surface treatment or added layer. This paper describes the new phenomenon and its application to recording information.

#### EXPERIMENTAL PROCEDURE

The occurrence of the new surface-sensitive phenomenon is illustrated diagrammatically in Figure 1, which shows the steps in recording a charge pattern on a thermoplastic layer, one half of which has been altered by the addition of a very thin layer of foreign material. In Figure 1(a), the entire surface has been given a negative charge

<sup>3</sup> R. W. Gundlach and C. J. Claus, "A Cyclic Xerographic Method Based on Frost Deformation," *Phot. Science and Eng.*, Vol. 7, p. 14, Jan. 1963.

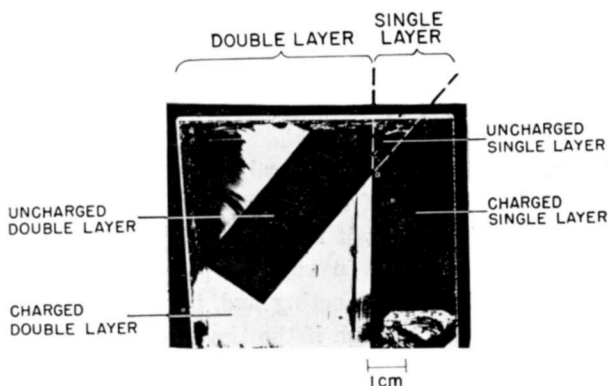


Fig. 2—Development of a simple charge pattern on a double layer.

pattern by shadowing corona from a high-voltage wire charger. Figure 1(b) shows the effect of heat treatment on the surface. The readily visible crazing pattern develops only where there is charge on the double layer. Where there is no charge or no top layer, crazing does not occur and the surface remains smooth. *The combination of charge and top layer* is therefore necessary in order to produce crazing.

An example of a visual crazing pattern is the photograph in Figure 2, made by reflected light, of a pattern on a polystyrene-coated slide. The slide had a thin polyvinyl alcohol layer over the large rectangular area on the left side and the surface was charged except for an oblique rectangular area and some irregular blotches. Heating this slide to the softening point of the plastic caused crazing to occur only in the charged and double-layer area. A second example of a more detailed charge pattern on a double layer that has been heat developed is shown in Figure 3. The method used to obtain this charge pattern is described



Fig. 3—Photograph showing a developed charge image on a double layer.

later. It has been found that the new phenomenon is independent of the polarity of the charge.

### ***Preparation of the Substrate***

The substrate can take any of several forms depending on how the final image is to be viewed. If transmission of light is required, the substrate must be transparent; if reflected light is used, the substrate may be opaque or even black. In any case it must be conducting or have a surface layer that is conducting and, if necessary, transparent. The conductivity need not be high if the time involved in the charging operation is reasonably long. In some cases, it is possible to obtain the necessary conductivity by warming the substrate slightly during charging. This can be done with soda-lime microscope slides. Where a semitransparent coating is required, the usual tin oxide layer can be used or, alternatively, a suitable evaporated layer of metal. A resistance of 5000 ohms per square is usually adequate.

### ***The Thermoplastic Layer***

The thermoplastic base-layer material may consist of a common plastic having the desired properties. The material must be a good insulator at room temperature and must remain a good insulator, at least for a short time, when heated to the melting point. Polystyrene is quite satisfactory, either in a low-melting form, PS-2\*, or in the higher-melting type such as is commonly available in sheets and solid stock. In general these materials are most conveniently applied from a solution of the correct viscosity made by dissolving the solid material in a solvent. Polystyrene is dissolved readily by toluene and can then be used to coat suitable slides by dipping and draining. The layer thickness thus obtained is a function of the concentration and is given very approximately by the curve of Figure 4. As seen later, the thickness of the base layer affects the characteristics of the crazing pattern produced.

### ***The Surface Layer***

The surface layer is added to the thermoplastic layer. The properties of this top layer have not been well established. Certainly the layer must have low lateral leakage, but this may be attained with a conducting material if it aggregates into small isolated areas. The layer should not have a melting temperature below that of the base

---

\* Made by Dow Chemical Co.

layer, and it should not be miscible with the base layer. It is probably desirable that physical properties be different from those of the base layer—such properties as viscosity, surface tension, volume conductivity and dielectric strength may well be important. Experimental work has shown that a satisfactory surface layer may be only one thousandth of an atomic layer (one atom per 1000 sites) for some materials and as great as 1000 Å thick for other materials. When the surface layer is too thin the resultant crazing produced is non-uniform and blotchy. When the layer is much too thick it forms a homogeneous smooth surface that is sufficient to prevent any development of crazing.

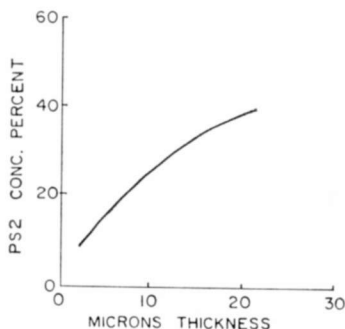


Fig. 4—Layer thickness as a function of solution concentration for polystyrene in toluene.

One of the unusual features of the new phenomenon is the fact that a large variety of materials can be used for the surface layer. Suitable surface layers include organic and inorganic materials. Their properties range from very good insulators at one extreme to metals at the other extreme.

Organic surface layers on the thermoplastic were the first materials to show well-defined and reproducible crazing when charged and heat developed. However, it was first demonstrated that condensed steam, distilled water, and deionized water applied to the base layer and then removed, left nothing on the surface capable of producing crazing. Thus it was possible to add known materials to the water with the assurance that results would be due only to the material added.

The first uniform surface layers were provided by S. M. Thomsen in the form of a step wedge of colloidal silica on a polystyrene base layer. When charged and heat developed, this arrangement demonstrated that an added layer as thin as 50Å produces a uniform crazing and that a layer 500Å thick gives only a few coarse random cracks.

It was then found that polyvinyl alcohol was easily applied to give large-area uniform crazing. With this material, the layer was applied by mechanically dipping the polystyrene-coated slide into a water solution of one part polyvinyl alcohol to 100,000 parts water. Immediately after dipping, the slide was thoroughly rinsed with distilled or deionized water. The resultant layer is probably only one molecule thick, since it is merely the amount of material held by the surface forces after complete rinsing. If rinsing is not done immediately, the meniscus leaves a pattern as the liquid withdraws. This pattern,

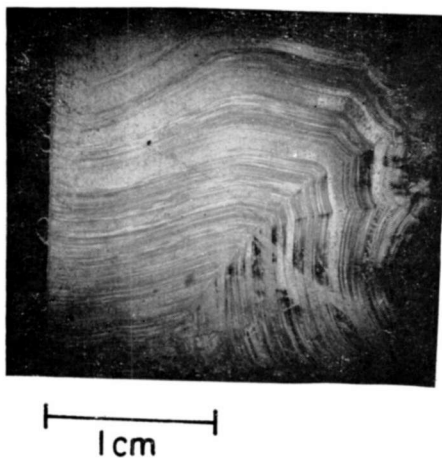


Fig. 5—Drying pattern of very thin polyvinyl alcohol layer on polystyrene after charging and heat developing.

although much too thin to be observed directly, shows up in a marked fashion after charging and heat developing. Such a drying pattern is shown in the photograph of a schlieren projected slide in Figure 5. In this case, the surface layer is too thick and nonuniform to give good quality crazing, but too thin to be seen before development.

A surface layer of particular interest is one composed of cross-linked polystyrene, since this is the same material as the thermoplastic layer but with many properties altered as a result of the cross linking. Layers of cross-linked polystyrene about  $50\text{\AA}$  thick were deposited on the polystyrene base layer. The cross-linked layer was produced in a low-pressure glow discharge in styrene vapor. These double layers showed excellent uniform crazing when charged and heat developed.

A cross-linked surface layer can also be produced as an integral

part of the polystyrene base layer by exposure to suitable radiation. Short-wavelength ultraviolet light is a suitable source for cross-linking; it penetrates very little, thus affecting only the surface. Figure 13 shows the crazing produced after charging and heat developing such an irradiated polystyrene layer. It is also possible to cross link the surface with a suitable electron beam or source of x-rays. All these methods have been used successfully and are discussed under Image Recording Methods.

Inorganic materials have also been used as the surface layer. In particular, thin evaporated layers of gold, aluminum, and tungsten have given excellent results. Layers were effective for calculated coverage of one thousandth of a monolayer of atoms. Layers thicker than about 10Å appeared to be too thick to produce crazing.

### ***Charging The Surface***

Uniform charging is most easily performed by using corona discharge from one or more fine wires stretched inside a grounded metal shield open on one side.<sup>4</sup> The open side is passed over the plastic surface without touching it while the wires are maintained at 5000 volts. Patterns of charge may be obtained by shadowing the corona discharge by means of metal or plastic masks. A pattern of charge may also be obtained from a uniform charge by photoconductive dissipation of the charge by a pattern of radiation.

### ***Heat Development***

It is possible to heat develop the thermoplastic layer by means of hot air or infrared radiation from above the surface. For most purposes, however, it is simpler to heat the slide from below by contact with a hot plate. For glass slides one-sixteenth-inch thick coated with PS-2 polystyrene (softening point about 70°C), contact with a hot plate at 140°C for about 4 seconds is adequate. The slide is then cooled, preferably quickly, on a metal plate.

Through the use of the magnetically operated device shown in Figure 6, the development time in the hot-plate technique can be considerably reduced and very reproducible results can be obtained. The slide to be developed is held down by sponge rubber at the edges of a rectangular holder attached to the horizontal arm as shown. Attached to the hot plate is a nickel-plated copper block one inch square that is approximately 0.2-mil concave on the upper surface in order to give uniform heating when the slide is pressed against it. The prepared

---

<sup>4</sup> J. A. Amick, "A Review of Electrofax Behavior," *RCA Review*, Vol. 20, p. 753, Dec. 1959.

and charged 2×2 inch slide is inserted in the holder while the arm is swung away from the hot plate. Development is brought about by swinging the arm into the hot plate. This action closes a microswitch to cause the electromagnet to pull the sample into contact with the hot block for the desired time interval (determined by a time switch). A spring then raises the frame and sample to its original position, and

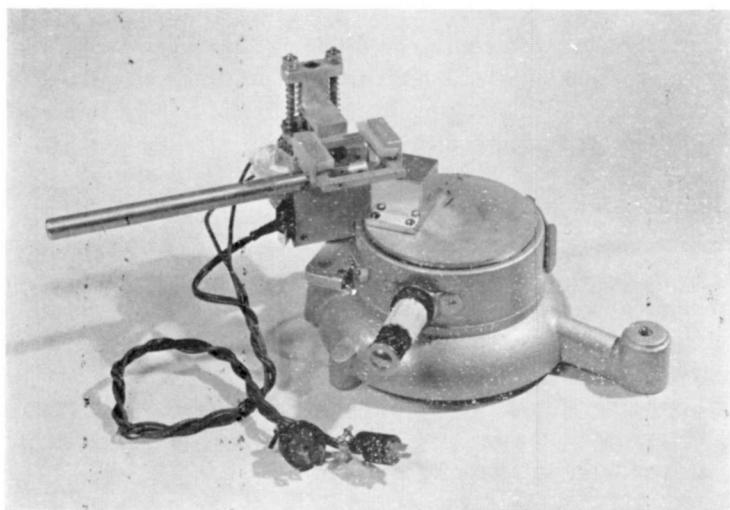


Fig. 6—Magnetically operated quick-heating arrangement using a hot plate.

the developed slide is removed by swinging the handle out. The speed of development in this device is limited by the lag in the heat transfer through the glass slide. Cooling of the slide is brought about by convection, radiation, and heat conduction to the surrounding area of the slide. Development times of one second with good reproducibility have been obtained using this device.

In an effort to show that much faster times were practical, experiments were also made on heating by passing a current through the semitransparent conducting coating on the substrate. Because of the problems involved in obtaining uniform heating at high current without burnout, the particular technique is worth describing. Pyrex\* slides two inches square were coated with tin oxide to a resistance of about 2000 ohms per square. A metallic layer of semitransparent

\* Trade mark.

nickel was then vacuum evaporated onto this coating to give a layer having a resistance of 20 ohms per square. Air drying silver was then painted on to give two contacts 2 centimeters wide and spaced 1.5 centimeters apart. The resistance of this layer was 15 ohms and, with 155 volts applied for 1/60 second, it was possible to develop crazing on a suitably coated slide over an area of 3 square centimeters.

Erasure of the crazed image can be performed by heating for a longer time or to a higher temperature to allow the charge to leak off and surface tension to restore the surface to flatness. In the case of images produced by charge patterns, it is possible to re-use the layer for a new image. Where the surface layer is distributed in a pattern, re-use is not possible since heating does not remove the surface layer.

### ***Observation of Images***

Since the crazed pattern of a heat-developed slide scatters white light and the smooth regions do not, any optical means that differentiates between scattered and unscattered light can be used for viewing. If only slight crazing occurs, a schlieren optical system is desirable. Such a system operates with dark field; thus crazed areas appear white and smooth areas dark.

A modified Kodak 2A projector is shown in Figure 7. It can be used as an ordinary projector with the front slit system tipped down or as a schlieren projector with the slit system up. The schlieren arrangement uses five equally spaced metal strips just in front of the condenser lens. The four bands of light so produced are imaged on the front bar system by means of a lens in the large barrel. Thus with no scattering surface in the slide position, a dark field is obtained on the projection screen. The same lens that is used to focus the bar system also projects an enlarged image of the scattering pattern of the slide on to the projection screen. The projector as described is, of course, a fixed-focus system, the position of the slide determining the location of the image. Examples of schlieren-projected slides with crazed images are shown in Figures 5 and 12.

For samples producing heavy scattering of light, a regular slide projector gives a good image, since the scattering portions scatter light out of the system and produce the dark areas of the image. Figure 11 is a photograph of a crazed image made using the projector with the front tipped down.

Direct viewing of the images is also possible by reflection and transmission. Viewed against a dark background and eliminating specular reflection by slant illumination, very good contrast can be obtained. Figures 2 and 10 were photographed in this way.

Specular reflection from the illuminating light can also be eliminated by using polarized light striking the slide at the Brewster angle. If the **E** vector is parallel to the plane of incidence, the reflection is zero from the smooth areas, so that only the scattered light is seen.

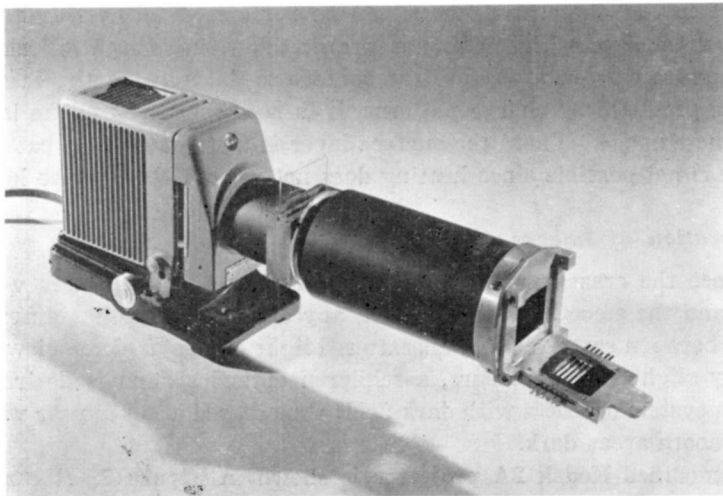


Fig. 7—Special schlieren projector convertible to ordinary projection by tipping down front slit system.

#### MECHANISM OF CRAZING FORMATION

Sufficient experimental work has now been done to define some of the factors that must be explained in the mechanism of crazing formation. It has already been pointed out that a large number of materials of widely different physical and chemical properties are suitable for the surface layer on the thermoplastic. One characteristic common to all is that the layer should be very thin. Thinness may be a requirement because it is necessary to form small islands separated by bare spaces. When such a surface is charged by corona, the potential on the islands will differ from that on the bare patches. However, it is unlikely<sup>5</sup> that these islands are larger than 100 Å, and this is much smaller than the observed crazing structure, which is about 20 microns in size—a factor of more than one thousand.

Figure 8 shows some very approximate dimensions applicable to

<sup>5</sup> L. Holland, *Vacuum Deposition of Thin Films*, Plate 40, John Wiley and Sons, New York, N. Y., 1956.

the base layer, surface film, and crazing structure as well as the maximum island size of the surface layer. To show the widely different dimensions the scale of the drawing is greatly distorted, and for convenient comparison the dimensions are given in angstrom units.

The character of the crazing pattern is shown in Figure 9. These photographs were obtained on a 20 micron PS-2 base layer on which a monolayer of polyvinyl alcohol had been applied. Figure 9(a) was

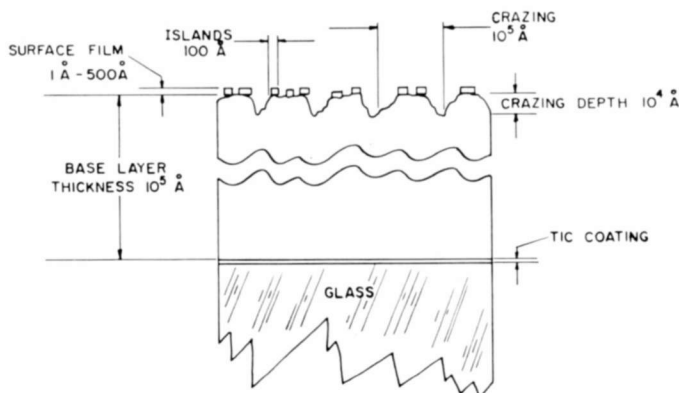


Fig. 8—Approximate dimensions of developed layer structure.

photographed with vertical illumination and Figure 9(b) was taken with low-angle illumination of the same area. It can be seen that the width of a disturbance is approximately eight microns, but the length in some cases is 80 microns. Figure 9(c) is a photograph of another sample with a base layer only a few microns thick. The crazing pattern in this case is finer and more regular. The depth of the crazing pattern was measured very roughly as one micron for a 20-micron-thick base layer.

The theoretical problem, then, is one of explaining how a charge nonuniformity of about 100 Å, produced by islands in the top layer, is amplified to a disturbance of 10 microns. R. M. Williams has suggested that the growth of this structure is similar to the growth of large water waves from small ripples produced by the wind. This is a problem in fluid dynamics that has been examined by many theoreticians. In the present case, however, a difficulty exists in explaining why such a growth in size should take place on the thermoplastic covered by a thin surface layer, but not on a thermoplastic alone. The

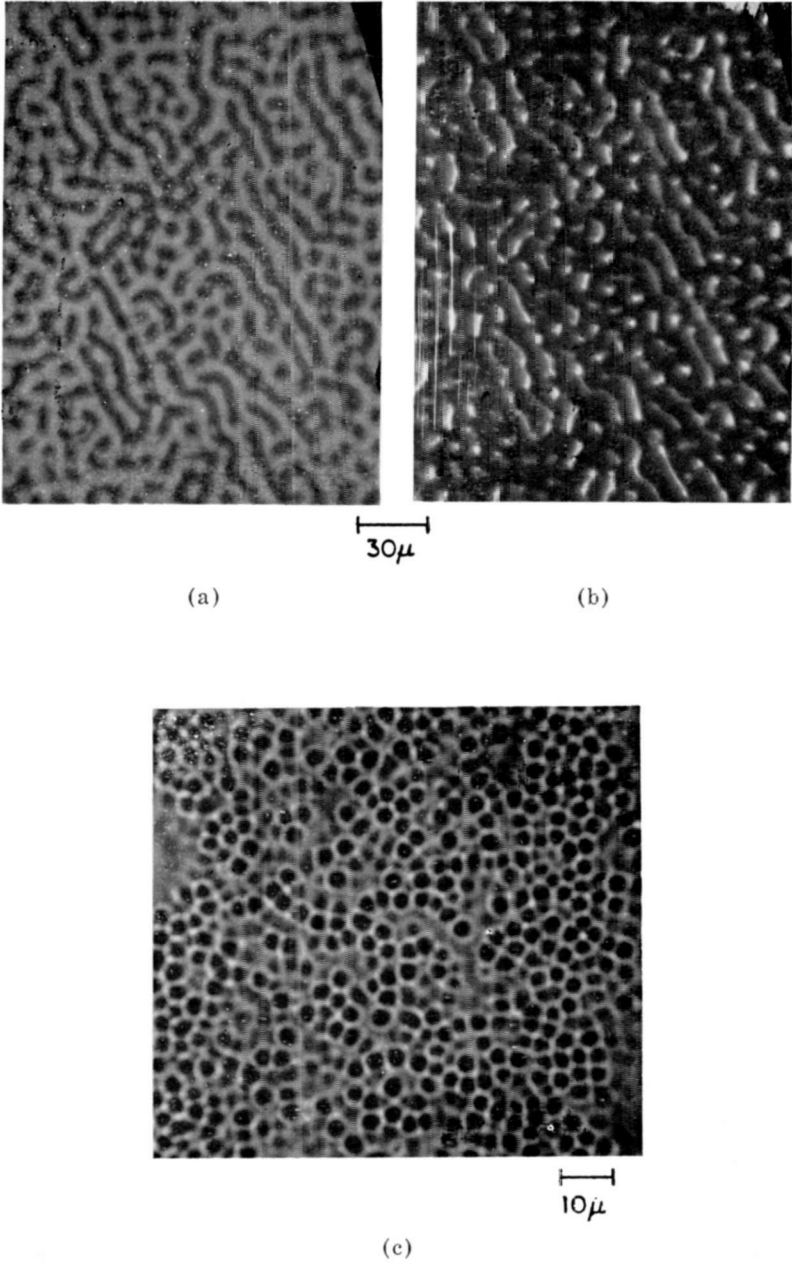


Fig. 9—Microphotographs of crazing structure: (a) vertical illumination, (b) same area with glancing illumination, and (c) crazing structure on thinner base layer.

difficulty arises because, even with a smooth uniform thermoplastic layer, small ripples should be produced by the nonuniform charge. The charge is nonuniform because it is insufficient to charge every surface atom. To take a particular example, a polystyrene layer 25 microns thick has a capacitance of approximately  $80 \mu\mu\text{f}/\text{cm}^2$  and can be charged by corona to 1000 volts. The charge  $q$  is therefore  $10^{-7}$  coulomb per  $\text{cm}^2$  or  $6 \times 10^{11}$  electronic charges per  $\text{cm}^2$ . The charges are therefore spaced about 150 Å apart on the average.

It is interesting to calculate the approximate depth of a deformation produced by charges 150 Å apart. Glenn<sup>2</sup> has given the following formula relating the wavelength of the disturbance  $W$ , the depth  $A$ , and the charge  $q$ ;

$$q = \frac{8 \times 10^{-10}}{W} (\epsilon T A)^{1/2},$$

where  $q$  is in coulombs per  $\text{cm}^2$ ,  $\epsilon$  is the dielectric constant, and  $T$  is surface tension in dynes per  $\text{cm}^2$ . The product  $\epsilon T$  is approximately 25 for materials such as thermoplastics and oils. Assuming that the formula applies for very short wavelengths and that  $W$  is 150 Å, the depth is calculated to be about 5 Å.

Attempts were made to observe such a disturbance on a clean thermoplastic surface, using a replica technique, in the electron microscope. A faint pattern was barely visible on the charged and heated surface, whereas on an identical uncharged and heated surface of the same layer the pattern was absent. If this is due to the charge spacing of 150 Å, then it is difficult to understand why this pattern also is not amplified to dimensions two or three orders of magnitude larger. There is a possibility that nonuniform surface tension, or a reduction in surface tension produced by the added surface layer is responsible for the growth in size of the disturbance. It is known from the work on gravity waves in fluid dynamics that absorbed layers or surface films affect the growth of large waves.

Cressman<sup>1</sup> has attributed his results to the reduction of surface tension caused by the charge on the plastic surface, the deformation beginning when the two forces are equal. In the present work, such a hypothesis would lead to the result that the added surface layer would lower the threshold for crazing or frosting. Such a reduction could not be observed since it was not possible to observe crazing or frosting at all without the added surface layer. Voltages up to 6000 volts on the charging wires produced no crazing on fresh and clean

polystyrene layers prepared by dip coating and thoroughly dried of all solvent. The voltage on the layer under these conditions was probably about 1000 volts for a 25-micron-thick layer.

Since the crazing phenomenon described in the present paper requires the added surface layer or surface treatment, the question arises as to whether Cressman's method of preparing layers by scraping or spreading the hot thermoplastic does in fact produce the special surface properties necessary to cause the frosting.

The presence of the top layer on the thermoplastic does increase the overall sensitivity to charge, the minimum detectable charge being less than can be detected by other means of observing charge patterns. It has been found that the two-layer structure can produce a visible image for a pattern of charge in dots or lines that is too small to develop by conventional powder techniques. Such a minimum developable charge on the double layer is also smaller than the charge required to develop lines or dots on a similar single layer of thermoplastic.

#### IMAGE RECORDING METHODS

In the new electrostatic phenomenon two conditions must be fulfilled to obtain crazing of the thermoplastic upon heat development. First there must be a suitable top layer on the thermoplastic and secondly there must be charge present. It is apparent therefore that images can be produced as a result of a charge pattern on a uniform top layer, or as a result of a top-layer pattern with uniform charge. Both of these methods lend themselves to a variety of techniques for producing either charge patterns or top-layer patterns.

#### **Charge Pattern and Uniform Top Layer**

In general there are three broad methods of depositing charge, the first involves corona excitation in some form, the second involves bombardment by a beam of charged particles in a vacuum, and the third involves uniform charging initially, with some means for dissipating the charge in the desired pattern.

Corona discharge in air is the usual method of *uniform* charging used in Xerography\* and Electrofax.\*<sup>4</sup> However, coarse patterns of charge can be obtained by charging through stencils of metal or insulating material. Figure 10 shows a crazed image produced by shadowing the corona with nylon threads and strips laid on the coated slide. Figure 2 was made by shadowing with a rectangular piece of Mylar.

Charging by corona in a pattern can also be achieved by applying high voltage to a sharp stylus moved very close to the surface of the

\* Trade name ®.

plastic layer. A similar technique is used with the Printapix type of tube<sup>6</sup> in which corona is caused to occur from any wire in a bundle passing through a cathode-ray-tube face. The electron beam in the tube is used to scan this wire bundle in the desired pattern.

Deposition of charge with an electron beam in a vacuum has not been investigated fully but crazing patterns have been obtained by this means. Certain limitations are imposed by the fact that at high voltages (15 kilovolts), if the current is sufficiently high, cross-linking

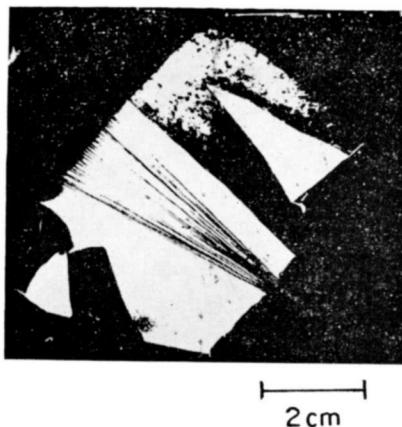


Fig. 10—Crazed pattern produced by shadowing corona with threads and Mylar pieces.

of the surface may take place. Deposition of charge with an ion beam is also a possibility, provided the total exposure does not provide too many deposited atoms that in themselves affect the crazing conditions.

Charge patterns can also be produced by charging uniformly and then exposing to radiation to discharge the desired regions. This is the normal method for obtaining images on Electrofax.<sup>4</sup> The slides prepared for these tests of crazing consist of a polystyrene layer coated with a suitable top layer as described earlier. Although polystyrene is not normally considered to be a photoconductor, exposure to sufficiently strong light will discharge the charged surface. The effective wavelength is in the neighborhood of 3000 Å so that it is not

<sup>6</sup> N. Fyler, D. Cone, R. Door, and J. Wurtz, "High-Speed Direct Electronic Printing Cathode Ray Tube," *Proc. of Fourth National Convention on Military Electronics*, p. 623, June 1960.

possible to use glass negatives because of absorption in the ultraviolet. The image obtained in Figure 3 was obtained by shadowing with an etched metal mask. The exposure was four minutes at a distance of 4 inches from a carbon arc lamp. A similar technique was used to produce the image of Figure 11. A polystyrene-coated slide with a polyvinyl alcohol layer on top was uniformly charged and exposed to the arc light through a wire mesh. The developed image

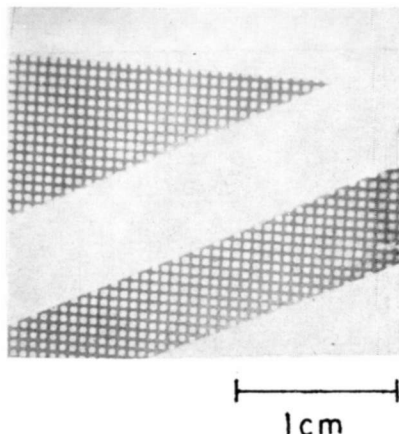


Fig. 11—Developed mesh pattern produced by light exposure of a uniformly charged slide. Photograph of an image projected by a regular projector.

in this case was so strongly scattering that it could be viewed by regular projection.

The use of photosensitive organic thermoplastics such as those developed by H. G. Greig<sup>7</sup> provides a very attractive means for obtaining photographic images using the crazing phenomenon. Figures 12(a) and (b) were obtained with a photosensitive material that was coated with a thin layer of polyvinyl alcohol. This particular organic material was sensitive in the long-wavelength ultraviolet, which is not absorbed by glass, and hence allows the use of a standard photographic negative. Figure 12(a) was made by exposure through a negative so that charge remains in shadowed portions that, after development, appear white on schlieren projection. Figure 12(b) was exposed through a positive to give the opposite polarity image on projection.

<sup>7</sup>H. G. Greig, "An Organic Photoconductive System," *RCA Review*, Vol. 23, p. 413, Sept. 1962.



3mm

(a)



3mm

(b)

Fig. 12—Images showing gray scale on schlieren projection: (a) made by exposure through a photographic negative and (b) made by exposure through a photographic positive.

Figures 12(a) and (b) were made from photographs of the projection screen.

### *Surface-Layer Pattern and Uniform Charge*

There are many means of obtaining patterns in the very thin surface film needed to produce crazing. These include cross-linking of a thin surface layer of the polystyrene by a radiation pattern, or image, and actual deposition of suitable material. The latter may be by vacuum evaporation, by physical contact from a stylus or suitable image transfer medium, or from ion beams in a vacuum.

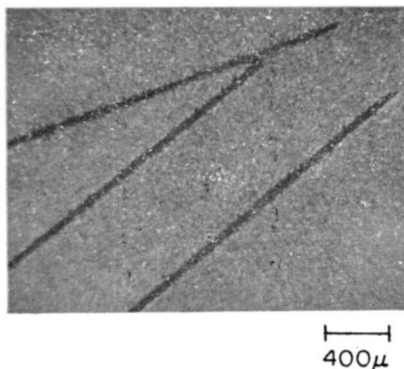


Fig. 13—Image obtained by surface cross-linking produced by short ultraviolet shadowed by 50-micron glass fibers.

An example of a polystyrene surface cross linked by exposure to short ultraviolet and then charged and heat developed to give an image is shown in Figure 13. A quartz ultraviolet lamp (Hanovia type SH) was used to expose the uncharged polystyrene for one-half minute at a distance of 1/4 inch from the lamp. Glass fibers 50 microns in diameter were used to cast shadows by absorption of the short ultraviolet thus preventing cross linking under them. After exposure and consequent cross linking, the slide was allowed to stand for 72 hours before being charged uniformly and heat developed. In this way any photoconductivity induced by the longer wavelength ultraviolet present had decayed completely and did not interfere with the charging process.

Cross linking of the surface of the polystyrene by a modulated electron beam can also produce a pattern that can be observed after uniform charging and heat development. However, it is necessary to choose the correct beam voltage and current density. If the voltage is too high, exposure to the beam will cross link too deep a layer and

no crazing will occur on charging and developing. If the voltage is too low, insufficient cross linking will occur. In a rough test it was found that a 2000-volt beam and approximately  $10^{-5}$  coulomb per  $\text{cm}^2$  cross linked the surface so that a pattern was developed. Tests with a 1000-volt beam indicated that the cross-linked layer, if formed, was too thin to produce crazing.

The penetration of an electron beam into a material of density  $\rho$  at voltage  $v$  is given fairly accurately, for voltages above 500, by

$$\rho d = 2.34 \times 10^{-12} v^2,$$

where  $d$ , the penetration, is in centimeters. The depth of maximum

Table I

$v$ (volts)	$d$ Å	$d_m$ Å
500	55	18-28
1000	220	77-110
2000	880	290-440
5000	5500	1800-2800
10000	22000	7300-11000

energy loss,  $d_m$ , is about 1/3 to 1/2 of the total penetration. Table I gives some calculated values for penetration in polystyrene with  $\rho = 1.06$ .

If it is assumed that 50 Å of cross-linking is needed to produce crazing, as was the case with deposited cross-linked layers, then the table indicates that about 700-volt electrons are required. However, the actual observed effects were obtained with somewhat higher voltages. This difference may be attributed to a change in the efficiency of cross linking with voltage, or to some surface charging of the layer that reduces the effective beam voltage during bombardment.

X-rays can also be used to produce a permanent cross-linked pattern in the polystyrene that can be developed by the usual charging and heating. As was the case with electrons, the depth of cross linking must be right to produce crazing. If the x-ray beam is too hard and the exposure long, the depth of cross linking will be too great and no crazing will occur after charging and heating. Insufficient data are

available to indicate the best range of x-ray hardness. However, crazing patterns were made by exposure to tungsten radiation at 45 kilovolts and 20 milliamperes, with the sample placed 10 inches away and exposed 1/2 hour. It is probable that very much softer x-rays would be more satisfactory and would require less exposure.

Deposition of a suitable layer pattern onto the thermoplastic surface can be accomplished whether the added material is organic or inorganic. The amount of organic material required to produce crazing can be deposited in a pattern on the polystyrene by various means.

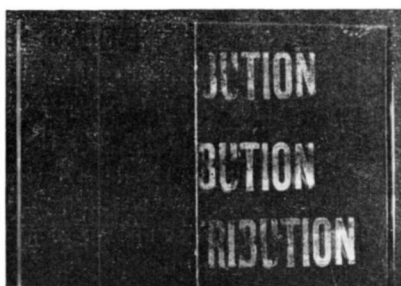


Fig. 14—Image obtained from rubber stamp pressed on to slide: charged and heated on right half, uncharged and heated on left half.

Writing can be done with a stylus or ball-point pen using a very dilute solution of suitable material to give a pattern that can be developed. Because the small amount of material required may be available naturally on a number of surfaces, a pattern can sometimes be made by pressure contact to the polystyrene with material transfer from such a surface. For instance, a resolution pattern was developed by transfer of material from the emulsion side of a 35-mm test pattern on photographic film. Newsprint can in some cases be transferred by contact to the polystyrene to give a heat developable image. The usual difficulty is transfer of too much material. Figure 14 is a photograph of a charged and heat-developed image made by pressing a "clean" unused rubber stamp onto a polystyrene layer in several places. The slide was made in one piece, stamped, and then cracked down the middle. The right-hand piece alone was then charged and the two pieces were heated side by side; only the charged side developed an image.

Vacuum evaporation through a mask gives excellent patterns with many materials and particularly with metals. Figure 15 shows a developed image of a few lines of gold about one atom thick, evaporated through a fine wire grill. The spacing between wires in the grill is approximately eight microns, which is the width of the lines in the microphotograph of the scattering produced after charging and heat developing.

Deposition of material from an ion beam or a molecular beam is another means of recording information. This is again possible be-

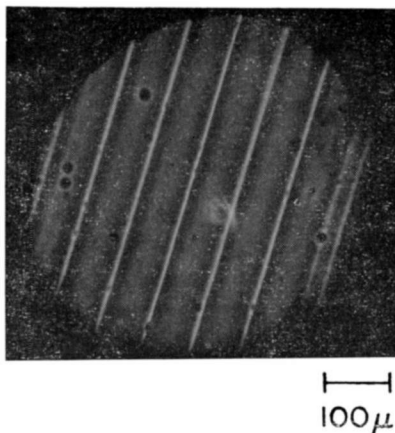


Fig. 15—Charged and heat-developed image of fine gold lines one atom thick on a polystyrene layer.

cause of the very small amount of material required. A commercial MS-7 mass analyzer can provide up to  $10^{17}$  ions/cm<sup>2</sup>, which should be more than enough. The mass analyzer has been used to produce a 20-kilovolt ion exposure test on a glass strip coated with polystyrene. After the test and removal from the vacuum, the layer was charged uniformly and heat-developed to display the various ion masses.

The appearance of the developed lines is best seen from the photographs of the schlieren-projected image shown in Figure 16. However, the lines are also visible under a microscope and by regular projection. The very noisy background in Figure 16 is not characteristic, but is due to a rather poor layer of polystyrene and the long storage time before exposure and development, which allowed dust to accumulate.

From the known line area and ion-beam current, it was calculated that  $3 \times 10^{-8}$  coulomb/cm<sup>2</sup>, or  $2 \times 10^{11}$  ions/cm<sup>2</sup>, can be detected.

This corresponds to  $2 \times 10^{-4}$  monolayer of gallium or arsenic atoms. This is a considerably thinner layer than that of the evaporated gold in Figure 15. However, it was later shown, by evaporation of tungsten, that a much thinner layer will suffice. In fact the minimum thickness is in good agreement with that for ions.

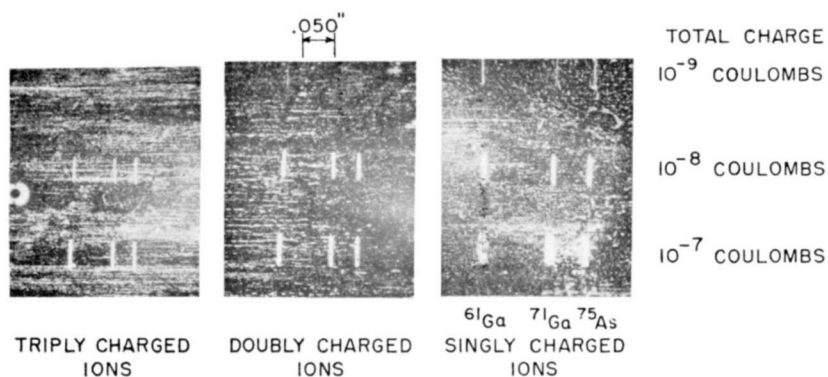


Fig. 16—Charged and heat-developed lines recorded on MS-7 mass spectrograph.

### CONCLUSION

The new crazing phenomenon, which depends on an added layer of material on the thermoplastic, is a sensitive high-resolution method of recording information. A visible image is obtained by using either a charge pattern or a surface-layer pattern. The imaging process is sensitive to a wide range of radiation wavelengths or incident particles. The first investigation of the new phenomenon has not stressed the high-sensitivity aspect. It is probable that with greater care and better choice of materials the sensitivity can be made to approach that of photographic film for some applications. The halftone capabilities without screening, and the rapid dry development with possible re-use under some conditions, make this a very attractive recording process.

### ACKNOWLEDGMENTS

The work reported here depended greatly on help from other members of RCA Laboratories who willingly assisted in various ways. H. F. Ogawa made a large contribution by his careful observations of the results of small changes in techniques and procedures. J. W.

Mirsch bombarded a number of samples with electrons. M. D. Coutts, G. W. Neighbor, and J. R. Woolston provided some special materials, electron micrographs, and tests with x-rays and ions. S. M. Thomsen was very helpful in the early stages in making available some samples of thin surface films. C. Busanovich kindly provided some unusually thin cross-linked polystyrene layers. H. G. Greig and N. E. Wolff were of assistance in providing photosensitive organic materials and in discussions. R. M. Williams, A. Rose, and E. G. Ramberg have also given time to discussions of the new phenomenon. Thanks are due to H. Johnson and W. M. Webster for their enthusiasm and support throughout this work.

# THE NASA RELAY I EXPERIMENTAL COMMUNICATION SATELLITE

BY

J. D. KIESLING

RCA Astro-Electronics Division  
Princeton, N. J.

*Summary*—The Relay communications satellites were designed to explore the technological problems of long haul microwave communications using medium altitude, active satellites. These technological problems, which include the environment of outer space, ground station performance, and compatibility with existing communication facilities are discussed in relation to satellite design trade offs. The various subsystems of the Relay satellite are described and the in-orbit experience with Relay I and Relay II is reviewed.

## INTRODUCTION

THE ESTABLISHMENT of world-wide high-capacity telecommunications by means of active repeaters in artificial earth satellites has been a potentiality and a challenge for some years. Now that rockets can place an earth satellite in a precise orbit with a statistically predictable chance of success, the technical challenge is to learn to design satellite systems having performance and operating life suitable for modern telecommunications at acceptable cost. A self-powered satellite having a long and reliable operating lifetime in a hostile radiation environment presents challenging design problems and the need for experimentation.

The NASA RELAY I project was designed to test the practicality of certain engineering concepts relating to orbital configuration, radio repeater operation for telecommunications including operating problems of large complex ground stations, and measurement of the damage to electronic components by the high-energy radiation environment. Related problems involving network control, tracking, and handover also required investigation.

When Project Relay was conceived and planned there had been only two experiments with active communication satellites. These were SCORE and COURIER. Both were successful in that they amply demonstrated the feasibility of communicating via a satellite. Im-

portant at the time, these projects contributed very little to the technology needed for commercial communications. The "Telstar" satellite and the "Relay" satellite were the first experiments undertaken to provide experience with wide-band active repeaters in orbit and to provide data on the space environment that is basic to the design of satellites with satisfactory operating lifetimes. "Telstar" is a private project of the American Telephone and Telegraph Company.

At the time Project Relay was conceived, which was many months before the beginning of contract work on its design and construction in May 1961, the Van Allen radiation belts had been recently discovered and adequate quantitative information was lacking as to their nature, distribution, and intensity. It was necessary to devise techniques of design that would minimize radiation damage to solar cells and electronic components, starting with the limited available data. The Relay satellite was to include means for measuring radiation effects in order to obtain information needed for future satellite design.

Furthermore, additional compatibility problems existed with ground-based communication facilities, the frequency spectrum available, and transmission standards. For example, what frequencies were suitable for high-capacity communication satellites? What suitable frequencies could be made available in a crowded microwave spectrum? Could space communications share the bands used for terrestrial overland trunks without undue interference? Would satellite wideband global telecommunications that meet modern high-quality transmission standards be achievable at reasonable costs?

Project Relay was conceived and designed to answer some of these fundamental questions. The extensive legal, scientific, and engineering study since that time was stimulated by general recognition of the important potentialities of communication satellites. Many national and international groups and individuals contributed to the impressive resolution of the questions relating to frequencies and sharing with other services, ending in an international agreement on frequency allocations for space telecommunications at Geneva in October 1963. Experience with Project Relay and Project Telstar contributed prominently to this international accord.

In the Relay satellite project, the Radio Corporation of America was contractor to the U. S. National Aeronautical and Space Administration (NASA). Both Telstar and Relay satellites were launched by NASA, using Thor-Delta rockets, from Cape Canaveral (now Cape Kennedy) on the Atlantic Missile Range in Florida. Relay I was launched December 13, 1962 into an elliptical orbit inclined 48 degrees, with an apogee of 4000 and a perigee of 800 miles. It is spin stabilized

at 160 rpm; attitude control is by means of a magnetic torque coil in conjunction with a horizon scanner and a solar aspect indicator.

Its power supply consists of solar cells and storage batteries. Power consumption is approximately 100 watts during wideband transmission.

The operating functions of the spacecraft are:

- (1) the relaying of wide-band microwave signals by means of a heterodyne repeater (two are provided, one acting as a redundant spare),
- (2) the telemetering of data indicating the status of circuits, components, and environment, and
- (3) the transmission of beacon signals to assist in the acquisition and tracking of the satellite.

All spacecraft power is generated by solar cells. Storage batteries, which are charged by the solar cells, are used to supply the peak power necessary for repeater operation. The satellite spins (at 160 rpm) so as to maintain axial alignment of the antenna radiation pattern for most favorable coverage of the earth. For spin stability, the moment of inertia about the spin axis is five per cent higher than about any other axis. Through the use of a torque coil, the satellite attitude may be adjusted on command to correct for (a) the drift of the spin axis due to forces resulting from interaction of the earth's magnetic field with the residual magnetic dipole moment of the satellite and the currents flowing in its electrical circuits, (b) torque forces due to gravity gradient variations caused by the nonspherical shape of the earth, and (c) orbit precession.

## THE SPACECRAFT

### *Structural Configuration*

Four views of the spacecraft in various stages of assembly are seen in Figure 1. The size of the body is determined by the size of the Thor-Delta low-drag shroud (fairing). Best use of this space led to an octagonal cross section with a maximum diameter of 29 inches and a height of 19 inches, topped with a tapered section 16 inches high. The complete spacecraft is seen in Figure 2.

The Relay design objective was to have an assembly meeting the following requirements:

Mass distribution disc-like for proper spin stabilization ( $I_{pitch}/I_{roll}$  not to exceed 0.95)

Maximum surface area for mounting solar cells (at least 4.75 square feet of projected area)

Size to fit within the shroud dimensions

Adequate direct access to all equipment components

Radio beacon and repeater antennas clear of the spacecraft body to reduce shadowing of the radiation patterns.

The central skeleton structure for Relay I is seen in Figure 3. Its cruciform arrangement provides a proper disc-like mass distribution,

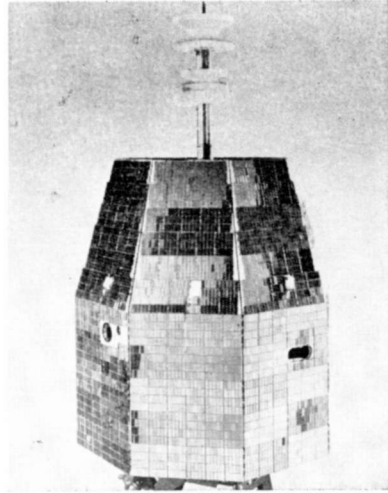
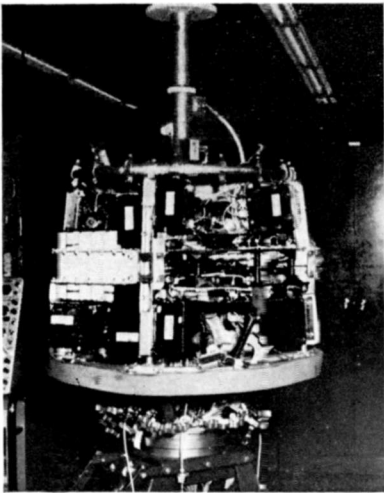
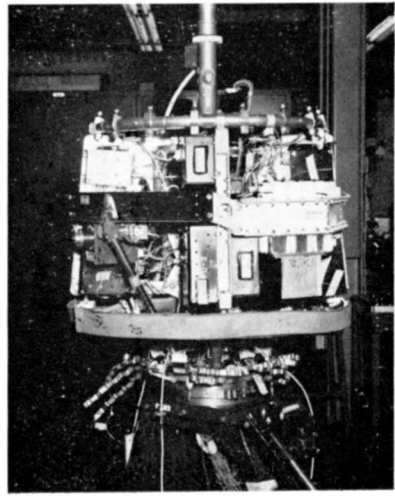
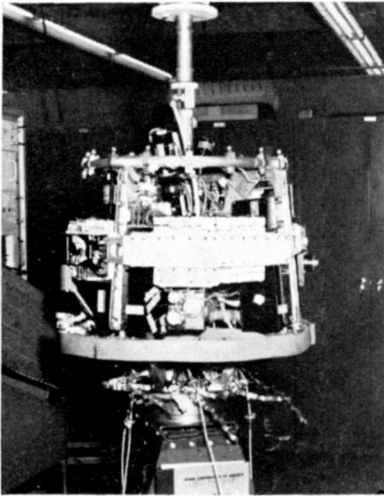


Fig. 1—Relay I satellite in various stages of assembly.

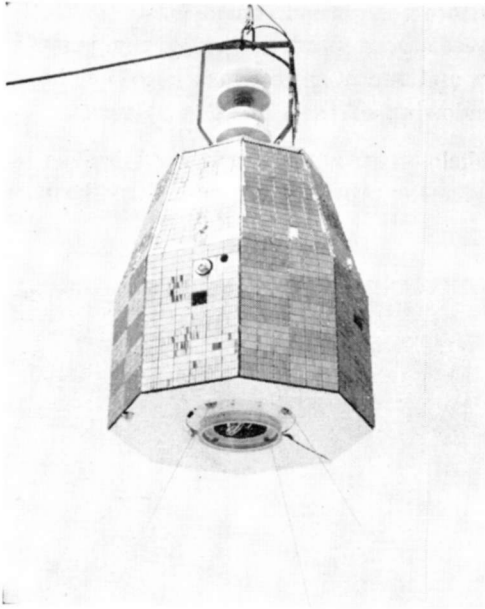


Fig. 2—The Relay I satellite.

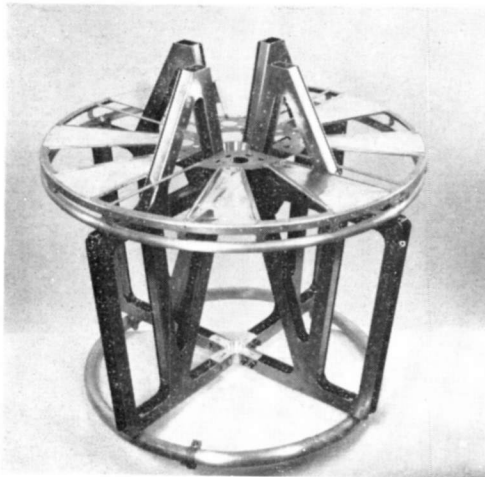


Fig. 3—The skeleton structure, showing the cruciform.

accessibility, and thermal conduction areas for the electronic components as seen in Figure 4. Careful consideration was given to the mounting of the repeater output traveling-wave tubes since these are the stiffest and hottest components used. They were treated as pure masses with minimum vibratory and thrust loadings transmitted to them through their mounts. The mountings also provide heat conduction to minimize temperature of the collectors. Vibration is reduced

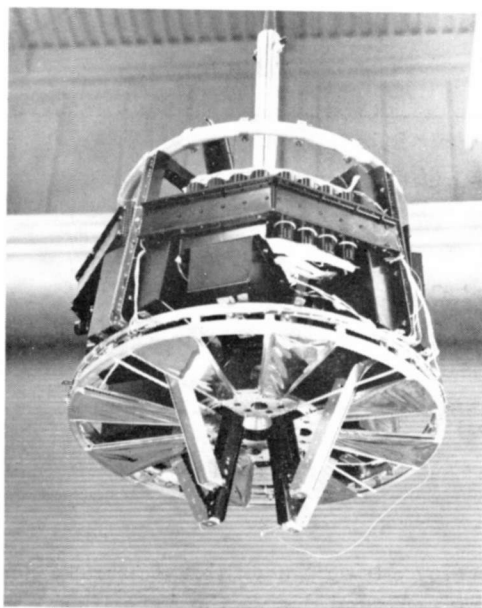


Fig. 4—The structure with components installed.

by encapsulating each tube in foam and by the location of these tubes within the structure. Thermal conduction to the outside is provided by a large-area flexible strap from the collector end to a heavy structural member. The chosen arrangement proved to be effective both for heat conduction and radiation, and avoided the added weight of a separate heat sink.

The structural design required the utmost care to attain the necessary stiffness and vibratory deadness at absolutely minimum weight. Aluminum alloy 2024-T3 was used since it provides optimum strength, modulus of elasticity, and density.

The solar-cell panels are of epoxy-bonded, honeycombed aluminum with three longitudinal reinforcing members. The outer skin has a

thickness of 0.005 inch and the inner skin 0.003 inch. Each of the eight panels is continuous for the full length of the spacecraft body. The angular shape is obtained by crustforming. The core is filled with epoxy resin to a width of two inches along the bend line for extra strengthening.

The vertical panel load is transferred to the cruciform skeleton by two brackets bonded near the panel top and resting on an upper hoop. The panels are restrained at their lower ends by fiberglass reeds that provide stiffness only in radial and tangential directions. This elimi-

*Table I*

Power-Supply Subsystem	66.2 lb.
Attitude-Control Subsystem	1.4 lb.
Radiation-Monitoring Equipment	13.4 lb.
Structure	18.8 lb.
Wideband Communication Subsystems	33.7 lb.
Telemetry, Tracking, and Command Subsystem	17.7 lb.
Wiring Harness	6.0 lb.
Miscellaneous (Balance Weights, Hardware, Cables)	17.8 lb.
<b>Total</b>	<b>175 lb.</b>

nates column loading during launch thrust acceleration—only tension plus bending is experienced due to the impossibility of the reaction vector intersecting with the panel's center of gravity.

The total weight of the eight panels with their solar cells, radiation-protective covers, and wiring is 31.9 pounds. The weight budget for the completed Relay I satellite is given in Table I.

### ***The Communication Repeaters***

The communication performance objective in the repeater design was to fully satisfy the international transmission standards for a circuit with two intermediate earth relay stations. The system performance of Relay I together with the associated experimental earth stations is shown in Table II.

There are two identical repeaters (transponders) aboard Relay I, one of which is a redundant spare that can be switched in by command from the ground.

Table II—Typical Link Performance

	Andover, Maine (USA) to Goonhilly, Down (England)		Nutley, N. J. (USA) to Rio de Janeiro (Brazil)		Andover, Maine (USA) to Pleumeur Bodou (France)	
	Ground to Spacecraft	Spacecraft to Ground	Ground to Spacecraft	Spacecraft to Ground	Ground to Spacecraft	Spacecraft to Ground
Experiment	TV	TV	2-way telephony	2-way telephony	one-way telephony	one-way telephony
Frequency	1725 mc	4170 mc	1725 mc	4170 mc	1725 mc	4170 mc
Deviation	4.6 mc	13.7 mc (peak-to-peak including sync)	.137 mc, rms	412 kc, rms	.69 mc, rms	2.08 mc, rms
Transmitter Power	10 kw	10 watts	10 kw	4 watts	10 kw	10 watts
Receiver Noise Temperature	6960°K	175°K	6960°K	420°K	6960°K	51°K
Antenna Gain (transmitter, circular polarization)	50.2 db	-1 db	42 db	-1 db	50.2 db	-1 db
Antenna Gain (receiver, circular polarization)	-1 db	58.3 db	-1 db	48.2 db	-1 db	57.6 db

Table II—Typical Link Performance (Continued)

	Andover, Maine (USA) to Goonhilly, Down (England)		Nutley, N. J. (USA) to Rio de Janeiro (Brazil)		Andover, Maine (USA) to Pleumeur Bodou (France)	
	Ground to Spacecraft	Spacecraft to Ground	Ground to Spacecraft	Spacecraft to Ground	Ground to Spacecraft	Spacecraft to Ground
Space Loss	176 db	184 db	176 db	184 db	176 db	184 db
Receiver Noise Bandwidth	23 mc	23 mc	23 mc	1.3 mc	23 mc	24.3 mc
Predetection Carrier-Noise Ratio	27.6 db***	14.7 db	21 db	8.3 db	27.6 db	18.1 db
Margin	—	7.0 db*	—	1.1 db	—	8.6 db
Minimum Base- band Signal to Noise (unweight- ed without pre- emphasis)**	—	30.5 db****	—	—	—	—
Baseband	3.5 mc (video**) and 4.5 mc aural subcarrier		12 channels		300 channels	

\* Frequency following receiver

\*\* 525-line 60-field television

\*\*\* Includes 1 db ellipticity loss and 1 db transmission line loss

\*\*\*\* Peak-to-peak signal to rms noise television

A block diagram of the dual repeater is seen in Figure 5. The receiver and its associated beacon are shown in Figure 6 and the traveling-wave-tube power amplifier is shown in Figure 7. Signals from earth stations to Relay I use a frequency-modulated carrier of 1725 mc. The carrier frequency is translated to 4170 mc and amplified to 11 watts before transmission to the antenna. In this process the modulation index is tripled and the signal is hard-limited. The tripling

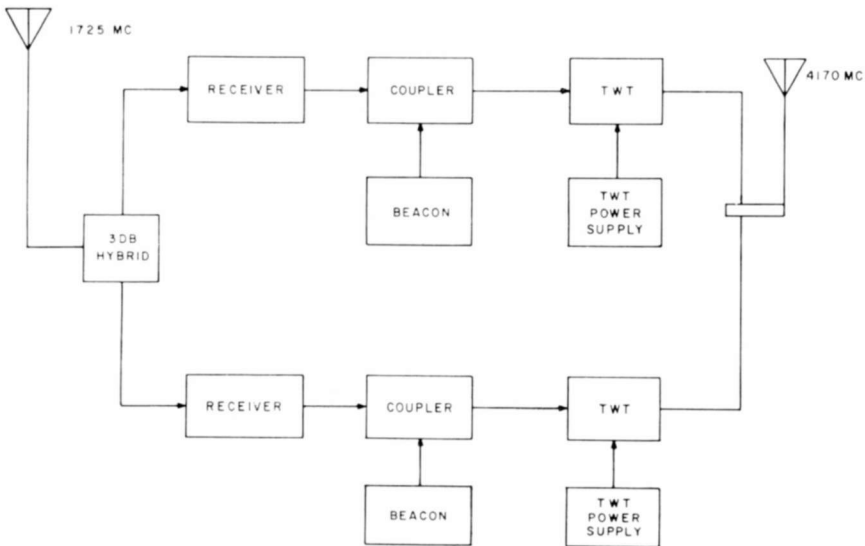


Fig. 5—Relay I wideband communication repeaters, block diagram.

of modulation index is done to compensate for bandwidth limitations of the ground klystron transmitters. The traveling-wave-tube amplifier also provides to the antenna a 200-milliwatt tracking-beacon frequency of 4080 mc.

### Receiver

Figure 8 is a block diagram of the receiver portion of a repeater. Its active elements are all solid state. The circuitry follows well-established principles, except possibly for its varactor frequency multipliers and intermediate-frequency branching—the latter being required for 2-way telephony because of the tripling. To accomplish this function, the latter stages of the receiver i-f amplifier are divided into three channels, switched by a voltage-controlled silicon diode switch in the i-f signal path. In the wide-band mode, the diode switch com-

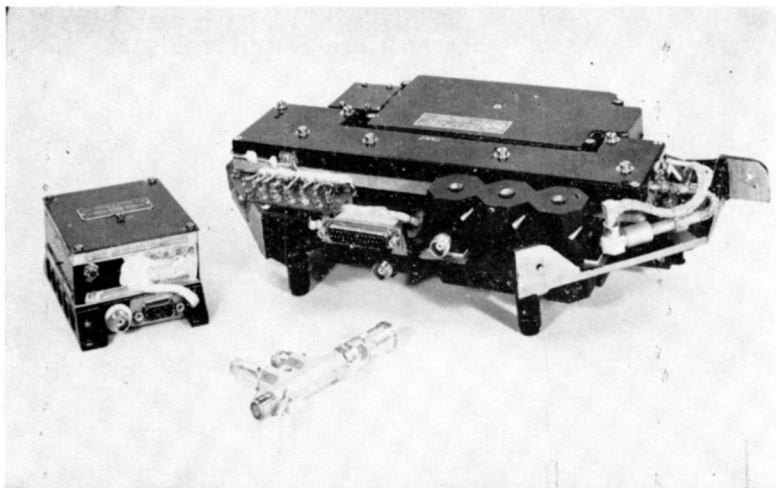


Fig. 6—The wide-band communications receiver and its associated beacon.

pletes the i-f signal path, through a broad-band signal tripler stage, to the antenna with an output bandwidth of 35 mc between  $-1$  decibel points. This channel is used for television, one-way multichannel telephony, and other experimental wide-band transmissions. For two-way transmission, the two ground transmitters are offset in frequency  $\pm 5/3$  mc. The ground receivers are offset in frequency  $\pm 5$  mc. In the satellite receiver the i-f switch is in the alternate position, completing the i-f through two parallel, narrow-band channels displaced from the

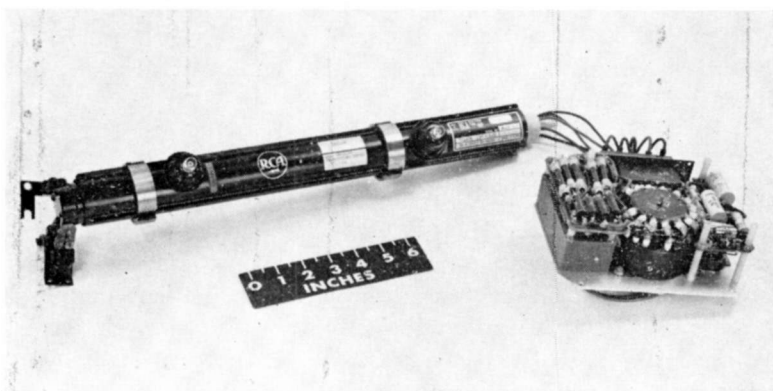


Fig. 7—The traveling-wave tube and its power supply.

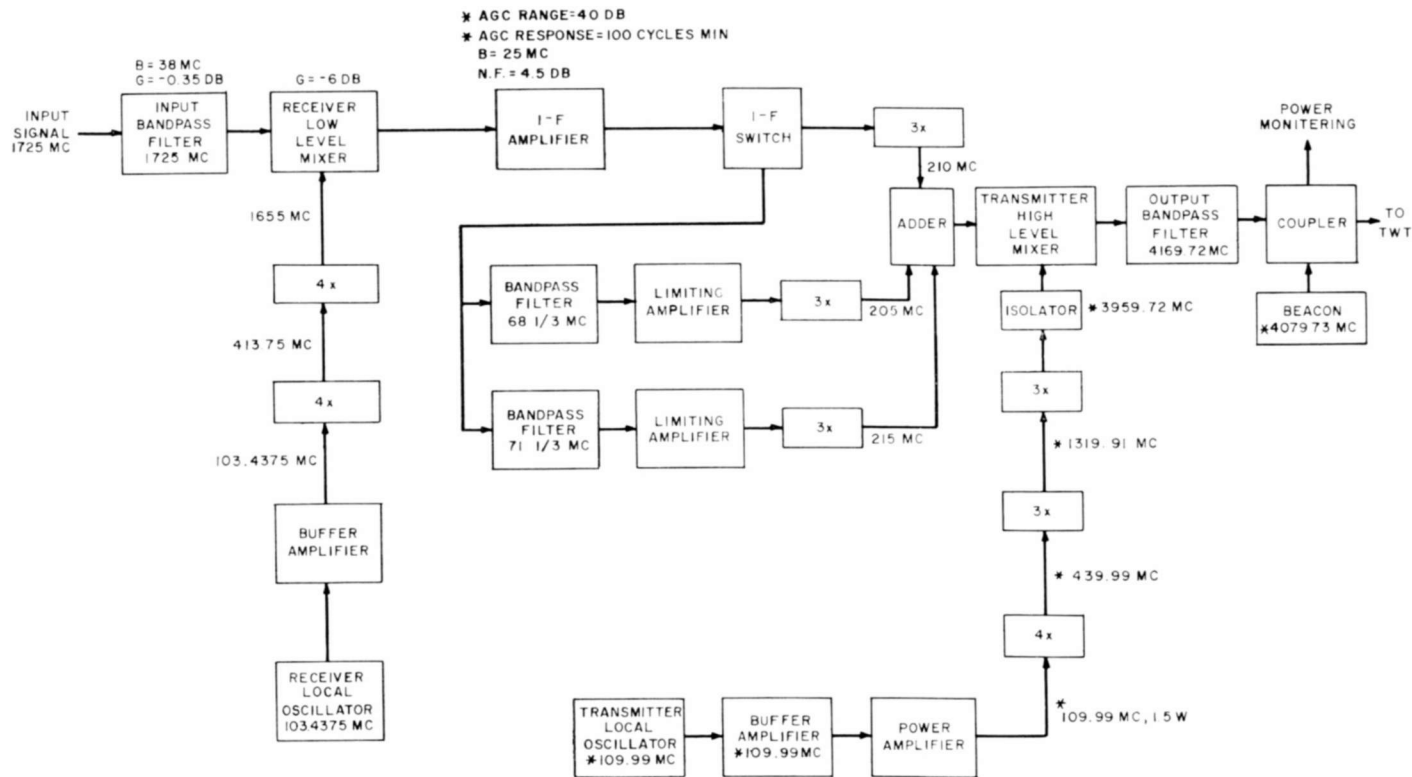


Fig. 8—Receiver block diagram.

input center frequency by  $\pm 5/3$  mc. As seen in Figure 8, the two-way signals are amplified together in the main i-f, separated by filters, tripled in frequency, and recombined by a linear adding circuit. The receiver noise figure is 14 decibels, including 3 decibels loss in a branching hybrid, and the maximum overall gain of the receivers exceeds 100 decibels. The receiver will operate at input levels from minus 80 dbm to minus 40 dbm.

### ***Traveling-Wave-Tube (TWT) Power Amplifier***

The TWT amplifier, shown in Figure 7, is capable of a saturated output power of 11 watts at a gain of 36 decibels over the frequency range of 4050 to 4250 mc. The efficiency, including heater power, is 21.5 per cent. The tube is designed to operate in the vacuum environment of outer space. It is radiation and conduction cooled and is mounted inside a cylinder filled with a foam plastic for isolation from the launch stresses and any other stresses that might be induced due to movement of the spacecraft structure. The tube is built in two versions, one of which uses a pressurized envelope. In the second version, the tube is not pressurized, i.e., the capsule surrounding the vacuum envelope is allowed to assume a low gas pressure. The high-voltage power supply for the TWT is all solid state and consists of a d-c to a-c converter feeding the primary of two high-voltage transformers. The first of these transformers provides cathode voltage ( $-1000$  volts at 45 milliamperes) and filament voltage to the tube as soon as the repeater is energized. After a 3-minute time delay a solid-state switch closure energizes the second transformer, which applies helix and anode voltage to the TWT simultaneously. Thus only a transponder turn-on command is required. The high-voltage supply is unpressurized and, except for an electrical shield, operates directly in the space environment.

The entire system including the antennas has a typical unequalized group delay of 0.5 ns per mc linear component, and 0.16 ns per mc<sup>2</sup> parabolic component within the operating temperature range, yielding a total intermodulation noise of about 1500 picowatts for 300-channel telephony.

### ***Microwave Antennas***

The spacecraft communications antennas receive at 1725 mc and transmit at 4170 mc and are contained in one mechanical assembly, consisting of a coaxial receiving antenna inside the coaxial transmitting antenna. The whole assembly projects from one end of the satellite

(the antenna array for telemetry and command is mounted on the other end of the spacecraft). Both microwave antennas are circularly polarized but of opposite sense and are quasi-isotropic, with a vertical coverage extending from 40 to 115 degrees (1-db-down points). Each antenna consists of inclined slots around the periphery of the coaxial outer conductor. External plates convert the linear slot excitation into a circularly polarized wave. The receiving antenna is excited in the

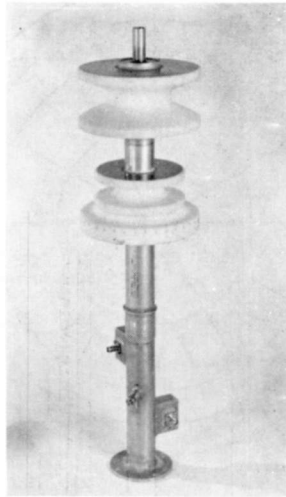


Fig. 9—The microwave antennas.

coaxial TEM mode. The transmitting antenna may be driven from either of two orthogonal ports that excite circularly polarized  $TE_{11}$  modes of opposite rotation sense in the coaxial line. The two ports are thus isolated, and the "off" TWT does not load the active TWT. The antenna weighs  $2\frac{1}{4}$  pounds. A picture of the dual antenna assembly is shown in Figure 9. Typical antenna radiation patterns are shown in Figures 10a and 10b.

### **VHF Antenna**

The 136-mc VHF antenna consists of four monopoles extending out from the mounting ring face of the spacecraft. For command reception the antennas are fed in phase to produce a basically dipole-like pattern. For telemetry and tracking transmission, the monopole pairs are fed in phase quadrature to produce a circularly polarized wave in the plane perpendicular to the spin axis. In any plane parallel to the spin axis the wave is linearly polarized. A diplexer harness is used to

couple the two receivers and two transmitters to the antennas. The receivers are connected in parallel through  $1/8$ -wavelength cables, so that an open or short circuit on one of the receivers will have a minimum effect on the other. The transmitters are coupled into the harness through a 3-decibel coupler providing a minimum of 20 decibels isolation between transmitters. The weight of the antenna assembly (monopoles and harness) is 1.25 pounds.

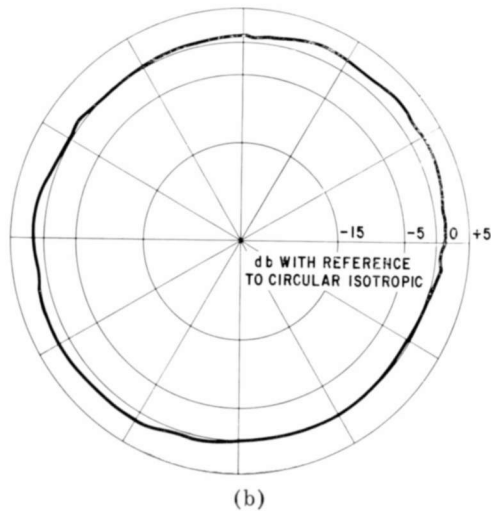
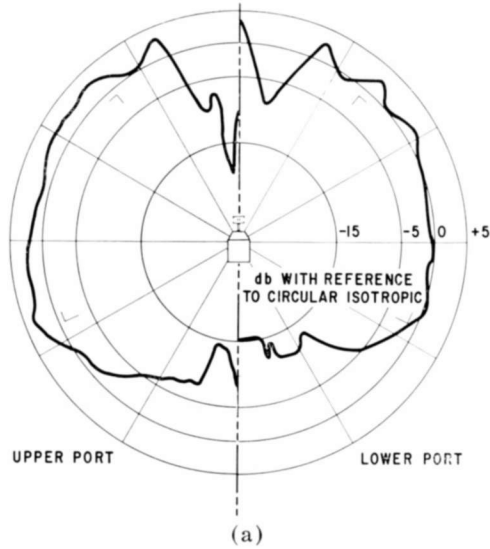


Fig. 10—Wide-band antenna radiation patterns: (a) polar plot and (b) equatorial plot.

## TELEMETRY, TRACKING, AND COMMAND SYSTEM

***Telemetry and Tracking Transmitter***

Orbital data for the Relay program is provided by the NASA global Minitrack network, operating in the 136-137 mc band. For the tracking signal, an unmodulated carrier is radiated continuously at a 0.25-watt level by the satellite. Upon ground command from a control station, a second transmitter (identical to the first one, but removed from it in frequency) may be energized. Either transmitter may be selected for tracking or telemetry; if one should fail, the other would be used for both functions. The transmitters are crystal controlled, all solid state, and are phase-shift keyed by the modulating signals. Each transmitter weighs 0.65 pound. There are 128 telemetry channels used to report satellite status and experimental data to earth.

***Encoder***

This unit samples transducer output voltages in the satellite and converts the information into a digital, 9-bit, pulse-code-modulation signal for transmission to the ground through the telemetry transmitter.

***Command Receiver***

This is an amplitude-modulated, crystal-controlled single-conversion superheterodyne receiver originally designed for and successfully used in the TIROS series of satellites. Each of the two receivers weighs one pound and draws 1/8 watt at 12 volts.

***Decoder***

Twenty commands can be sent to the satellite, using digital transmission on an audio subcarrier. A 3-out-of-6 error-detecting code is used to provide relative immunity against interfering signals. Two decoders and two command receivers are interconnected so that any one receiver and any one decoder may fail without affecting the circuit performance (see Figure 11). Recognition of a correct code energizes the corresponding control circuit, which then actuates the selected equipment. For example, either wide-band communication system may be switched on or off, current may be sent through the magnetic-torquing (attitude-control) coil, and telemetry transmission may be initiated.

If the satellite should go beyond line of sight with a wide-band repeater left on, a timer disconnects the repeater after two minutes.

## ATTITUDE CONTROL

Attitude control consist of means of correcting the initial attitude by small increments, means of reducing the precession motion of the spin axis to a small value, and means of offsetting the long-term drift of the attitude caused by external torques on the satellite. The requirements of each of these is briefly considered.

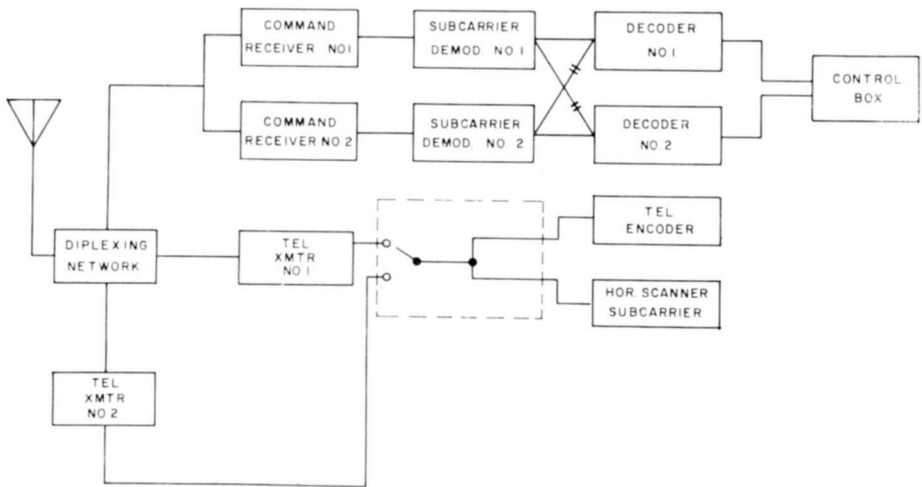


Fig. 11—Tracking, telemetry and telecommand system.

Injection into orbit was achieved with a high degree of accuracy; in fact, the  $3\sigma$  error in the injection attitude for Relay I was within  $\pm 5^\circ$ . The major portion of the long-term drift of its spin axis is caused by the torque produced by the earth's magnetic field and the dipole moment of the spacecraft due to residual magnetism and electric current flowing in the circuitry. By reducing the residual dipole moment, this drift can be made small; it is believed to be no more than  $0.1^\circ$  per day. Because the inertia ratio of Relay is higher than 0.9, the torque resulting from the gravity gradient is negligibly small.

The accuracy of injection depends in part on the angular velocity of spin-up during third stage flight which, for Relay I, was 160 rpm. Since the mission requirements could be accommodated without resorting to spin-down after injection, the high angular momentum imparted during spin-up resulted in a dynamically "stiff" satellite. Therefore, disturbances that give rise to precession, such as unbalanced forces

at separation, are not likely to give rise to large angles of nutation or wobble of the spin axis. Relay has a spin moment of inertia about one-fourth that of TIROS and an angular velocity more than 10 times as great. Thus, precession angles for Relay have magnitudes somewhat less than half of those experienced by TIROS for disturbances of the same magnitude.

The elements of the attitude-control system are of two kinds—the attitude-monitoring devices, or sensors, and the attitude-correction devices. There are two attitude sensors on the Relay I spacecraft—the sun-aspect indicator and the horizon scanner. Together, these provide the angular information from which the spin-axis attitude is computed. The attitude-correction devices consist of a magnetic torque coil, which may be activated by ground command to create a compensating field to that of the residual dipole moment of the satellite and the earth's magnetic field, and a fluid-type precession damper that acts to reduce the precession forces to which the spin axis may be subject. These devices contribute a weight of about 1.5 pounds.

The horizon scanner consists of an infrared detector and associated electronic circuitry. Its optical axis is aligned perpendicular to the spin axis. With the earth and satellite in correct geometrical relationship, the optical axis of the scanner intercepts the earth as the spacecraft rotates about its spin axis. As the scanner field-of-view ( $2^\circ \times 2^\circ$ ) intercepts the earth from space, the sudden increase of infrared energy causes a sharp rise in the output of its bolometer. As the field-of-view passes from earth to sky, the sharp decrease in infrared energy causes a corresponding fall in its output. In essence, the moment of tangency of the line-of-sight of the scanner and a limb of the earth at contact and horizon crossing is sensed.

To keep amplifier components small, the bolometer output signal resulting from the earth scan is converted into two pulses by differentiation—a positive pulse at contact, and a negative pulse at the separation phase of the scan. The signal modulates a 1.3-kc subcarrier oscillator and is transmitted by telemetry to a ground station.

The digital sun-aspect indicator is used to determine the sun angle (that is, the angle between the sun vector and the spin axis of the spacecraft). The solar aspect sensor was designed and built by the Goddard Space Flight Center of NASA. The sensor performs analog-to-digital conversion optically. It uses a binary "gray code" light mask to produce a digital signal in terms of elevation and azimuth angles of incident light from the sun relative to the satellite coordinates.

This device consists of a number of dual photo-diodes placed behind a light mask with slit openings as shown in Figure 13. Opaque separa-

rators are situated between the dual photo-diodes, so that each photo-diode sees only the portion of the light mask directly in front of it. The slits and diodes are aligned so that each diode has a fan-shaped field of vision lying in a plane parallel to the fields of vision of the other diodes. This sensor is designed to detect the sun which, for this purpose, is virtually a point source of light so that these parallel planes

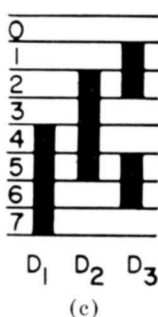
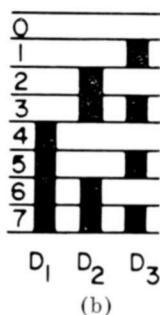
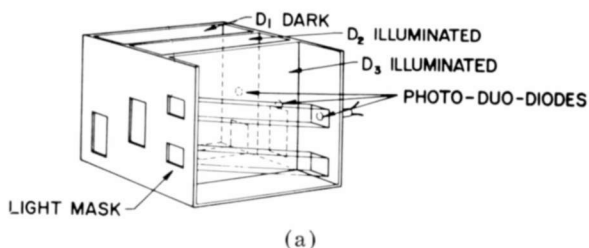


Fig. 12—The sun-aspect indicator: (a) 3-bit fan-type grey code sensor, (b) 3-bit regular binary code, and (c) 3-bit grey binary code.

can be assumed to be a single plane. If the sensor is rotated about a vertical axis in this plane, the field of vision of the diodes will sweep out a solid angle. When this field passes across the solar disc, one or more of the diodes will be illuminated. The particular combination of diodes illuminated provides a digital measurement of the elevation angle of the sun in sensor coordinates. The accuracy of this elevation measurement depends on how many binary sensors are used. A fan-shaped field of view can be quantized into as many as  $2^N - 1$  segments when there are  $N$  binary sensors. A gray-code system (depicted in Figure 12) is used instead of the regular binary code. The gray code requires a decision from only one sensor for each transition between quantized segments.

The sensor designed specifically for Relay uses 6 coding slits and one reset switch, and covers a field from  $+80^\circ$  to  $-80^\circ$  in  $2.7^\circ$  steps. It is designed to have an accuracy of about  $\pm 1^\circ$ , but in some applications, by applying data interpolation, its accuracy may be  $\pm 0.2^\circ$  or less. It is located with its axis perpendicular to the spin axis and parallel to a radius of the spacecraft. This sensor draws 5 milliamperes at 27.5 volts; "0" in the binary code corresponds to 4.5 volts and "1" to 0.0 volts. Physically, the sensor is a 2-inch cube with the light mask constituting the outer face. It weighs 0.54 pound.

The magnetic torque coil is center-tapped to obtain dipole moments of opposite sense (depending upon which half is energized), and has the capability of producing a dipole moment of 1.5 ampere-turns per square meter. The current drain is 12 milliamperes at 28 volts d-c. The coil assembly weighs less than half a pound, has a diameter of 25.3 inches, and consists of a total of 763 turns of No. 32 aluminum wire.

Torquing of the spacecraft is controlled by command signals from the ground resulting in a prolonged torquing with a dipole moment of one sense. This method is limited in the sense in which the attitude may be changed. Another method, based on reversing the torque sense each quarter orbit, requires a larger number of ground stations, each strategically located to realize its full potential. However, this one-station control method achieves the desired attitude correction by moving the spin axis in a path closer to the optimum. Prelaunch studies with a digital computer have proven useful in formulating procedures for both methods.

The precession damper on Relay is of the liquid-in-tube type. It consists of a toroidal tube in which the reservoir channel has an inside diameter of 7.25 inches and an 0.25-inch square cross section. It is mounted concentrically with the spin axis and, to make it most effective, its distance from the vehicle center-of-gravity is made as large as possible. For convenience, it was placed at the top of the cruciform.

Reduction of precession angle is achieved by virtue of the dissipation of energy in the fluid flow caused by the acceleration gradient of precession. Two modes of operation are possible. For large precession angles, the silicone liquid will flow as a slug, completely filling the channel of the reservoir along some portion of it. For smaller angles, the fluid does not contact the inner periphery of its channel at any point. Damping in this condition is not as effective as with slug flow. To accommodate that special condition of unfavorable inertia ratio during third-stage flight (when damper action would increase any precession), the damper is designed with the fluid volume slightly

less than half that of the reservoir. In this way, a sufficiently large transition angle between modes of flow can be obtained to prevent slug-flow. Thus it is unnecessary to cage the damper before separation of spacecraft and third stage. Calculations indicate that for the spacecraft alone, the time constant of damping is of the order of one minute.

#### THERMAL DESIGN

The requirements of simplicity and reliability dictated the use of a passive type of temperature-control system for the Relay spacecraft. The controlling factors of the passive control system are the ratio of absorptivity to emissivity ( $a/e$ ) of all surfaces (both internal and external) and the anti-reflective coatings on the solar cell covers. The solar cells have a fixed  $a/e$  characteristic and a narrow temperature range for optimum efficiency, and occupy more than 90 per cent of the side-surface area of the structure. Therefore, it was necessary to establish control of the  $a/e$  characteristic in the remaining areas. These controlled areas are provided by sheets or films closing the ends of the spacecraft assembly. The films are of aluminized Mylar,<sup>®</sup> painted on the outside to give the required  $a/e$  of 0.35.

As the analysis of these elements and of the mission constraints progressed, it was found that the control of temperature within the range 0° to 30°C was the best that could be assured. While this range was considered acceptable for electronic components, the need for best performance of the temperature-sensitive storage batteries led to the decision that this range was marginal; therefore, an active heat controller was introduced into the design to reduce the range to a more acceptable value. This controller acts as a vernier control, telescoping the temperature range by about 5°C at each end. It consists of two circular shutters, one fixed and one rotating. Alternate sections are covered with aluminized Mylar, with the intervening sections left open. The construction is shown in Figures 3 and 13. The controller occupies the area near one end of the skeleton structure assembly, and is located between the electronic components (e.g., the TWT's) and the spacecraft thermal end enclosure. It acts as a partial or total radiation barrier, depending upon the alignment of the two shutters. Thus, the whole arrangement acts as a controllable heat "leak" from the components to outer space—the sectors of the controller tending to open as the temperature rises toward the upper end of the range. The shutter actuator is a vapor-filled, temperature-sensitive bellows attached to a battery pack and acting through a mechanical linkage. The small end of the spacecraft also carries an end closure but no active heat controller.

Extensive testing by actual duty cycles was done on a full-scale thermal model in a vacuum chamber whose wall temperatures were controlled.

#### POWER SUPPLY

The Relay I spacecraft power supply is composed of solar cells, storage batteries, and control and protective devices. Initial requirements led to a solar-cell-area requirement of no less than 4.75 square

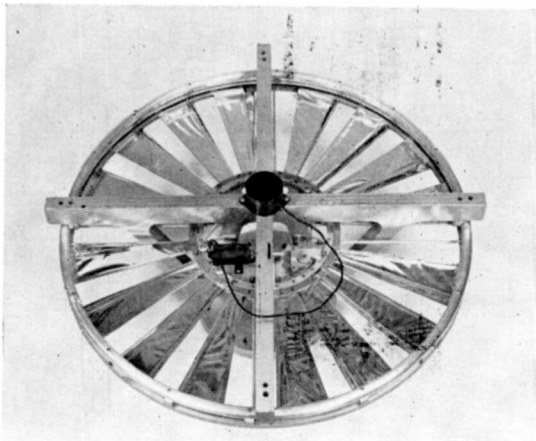


Fig. 13—The thermal controller.

feet. The 8 longitudinal panels on both the cylindrical and pyramidal areas of the satellite structure were sized to provide the necessary projected area. This afforded room for 8215 cells, each  $1 \times 2$  centimeters. The entire solar-cell array yields an average prelaunch power capacity of 60 watts at  $34^{\circ}\text{C}$ . Since the ends of the spacecraft are not exposed to the sun, no solar cells were placed on them. A block diagram of the power-supply system is shown in Figure 14.

The silicon cells are grouped into 5-cell shingles. Fifteen shingles (75 cells) are connected in series to provide the proper voltage; then all of the series-connected strings are wired in parallel to the batteries, through a diode power gate. The shingles are physically distributed in strings along the length of the spacecraft, nearly parallel to the spin axis, so that full strings are equally illuminated. The area packing-factor was 90.3 per cent.

The cells each carry a cover of fused silica (Corning No. 7940) 0.060 inch thick for radiation protection. The shingles are bonded

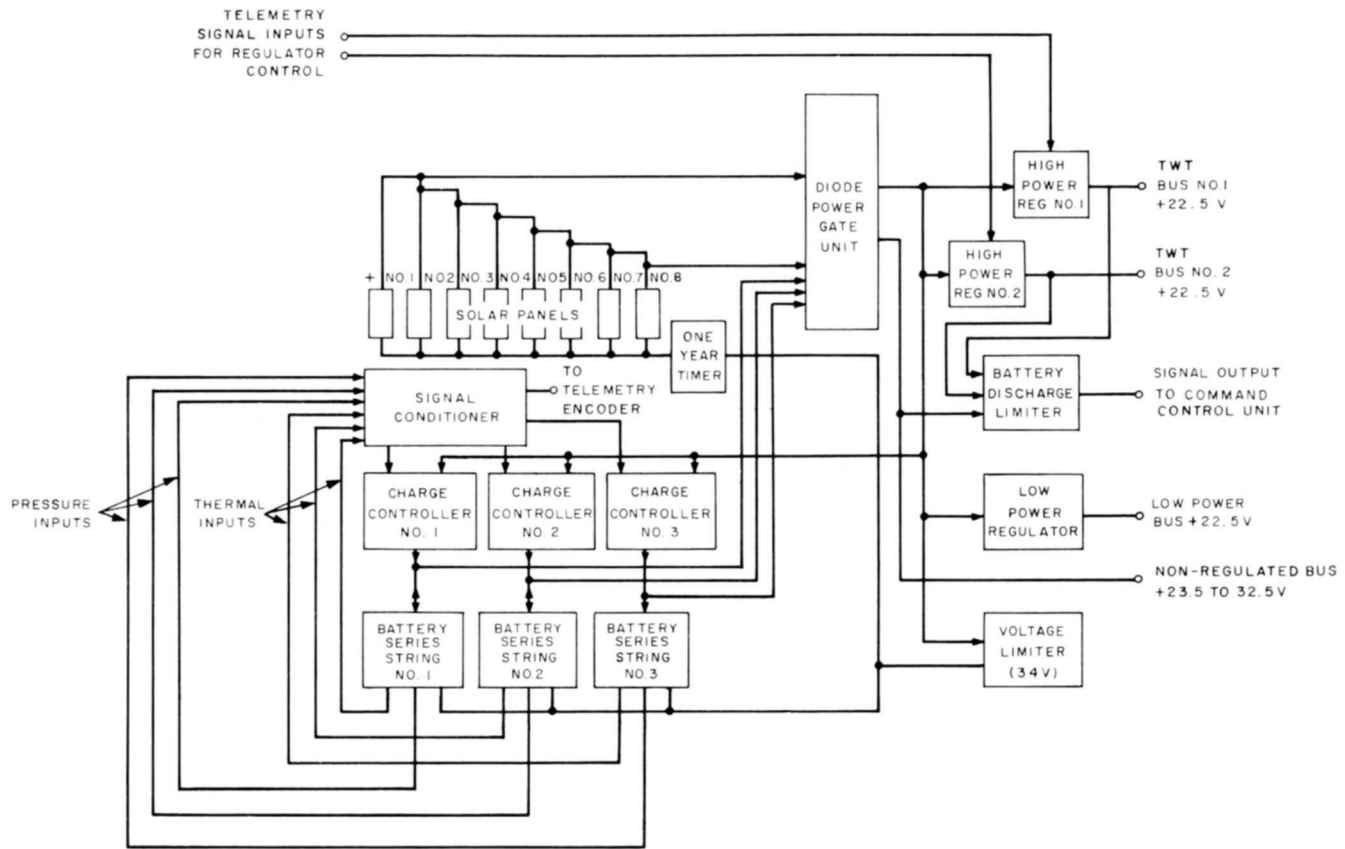


Fig. 14—Relay I power-supply system.

adhesively to the honeycomb panel. Face-wiring is employed, and the final power leads for each panel are brought through a "dark-time" blocking diode to a connector on the inner face of the panel.

The Relay I solar cells are p-on-n type boron-doped silicon with

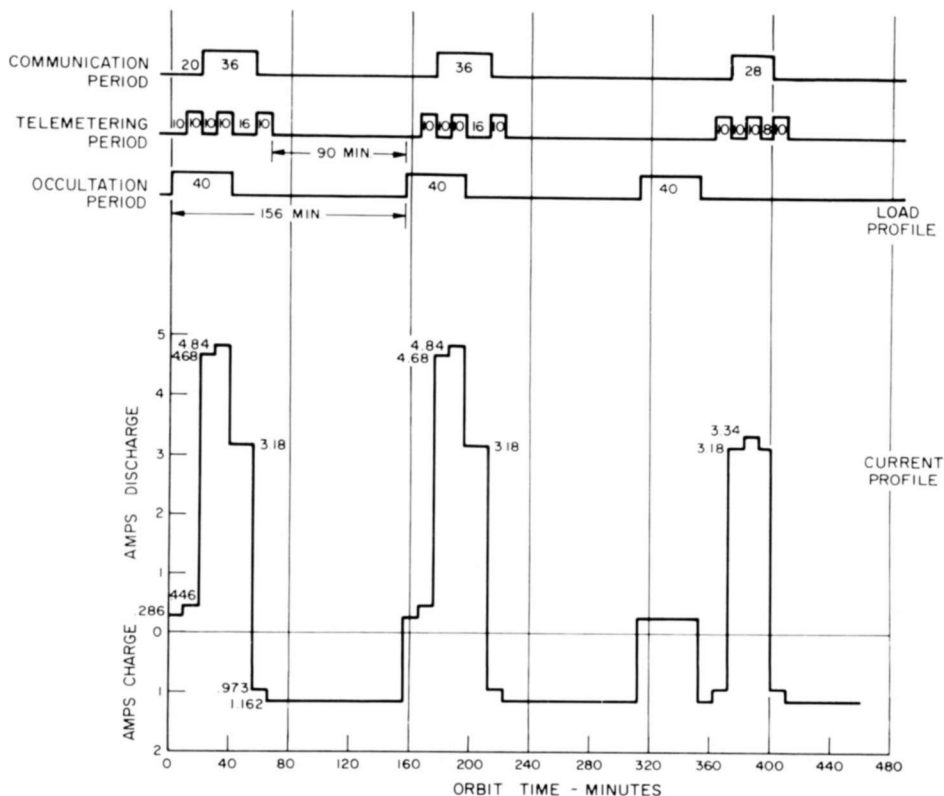


Fig. 15—The power profile.

face grids. To allow for degradation when in space, the solar-cell array has sufficient area in the initial, undegraded condition of the cells to produce 130 per cent of the estimated power requirement.

The storage battery cells are the sealed nickel-cadmium type. Each has a 3-ampere-hour capacity at 25°C and weighs 0.35 pound. Twenty of these cells are series-connected to provide 25 to 28 volts to the regulators. There are three 20-cell strings, physically divided into two battery packs, to form the complete battery. A power profile of the Relay electrical-load requirements, upon which this storage-battery capacity is based, is shown in Figure 15.

Three regulated 22.5-volt buses carry power to the two wide-band communication systems and the radiation equipment. An unregulated bus provides between 24 and 33 volts for all other equipment in the spacecraft.

Power distribution is controlled by the diode power gate, which allows flow of power from any of the eight solar panels or three battery strings to a principal power bus, and from any of the three battery strings or the solar array to an auxiliary power bus. Through the use of these diodes, only those power sources that are capable of developing sufficient voltage are paralleled. Solar panels with insufficient illumination and battery strings with insufficient voltage are automatically disconnected.

Associated with each battery string is a charge controller to permit a trickle-charge current of 50 milliamperes to the batteries whenever the solar-panel voltage is adequate. When the battery voltage builds up under charge to a normal value, the rate of charge is increased to 500 milliamperes. The batteries are monitored by a three-channel temperature transducer to prevent a continuing over-charge. Each channel is equipped to sense temperatures at a number of critical locations in its string of twenty storage cells. When the preset temperature limit is reached at any location, an output signal, developed in that channel, is applied to the appropriate charge controller to reduce the charging rate back to trickle charge.

For protection of all battery cells against too deep a discharge, a single-battery discharge limiter is provided. When the highest battery series-string voltage falls to a preset level as indicated by a low voltage on the unregulated (battery fed) bus, a voltage-sensing device signals the command-control unit to develop turn-off signals that are applied to the voltage regulators supplying the wide-band repeater busses. In the regulators, these signals act to hold the voltage outputs to low values, thereby effectively decoupling the repeater loads from the batteries.

With both repeater busses at low voltage, the output of the battery-voltage-sensing circuit is returned to normal value, so that control can again be exercised when required.

A single voltage-limiter unit is provided for the system. This unit is essentially a shunt regulator that puts an additional load on the power bus (from which it is supplied) whenever the bus voltage reaches the preset limit of 34 volts. This voltage value is considered as always adequate for charging the series strings of storage cells.

Through the use of the limiter, power loss in the charge controllers

and the series-voltage regulators is reduced at times of high solar-power output and low load. The voltage limiter is physically located so that its power dissipation can be radiated directly to surrounding space with minimum effect upon the temperature of the various working circuits of the satellite.

A voltage regulator is incorporated for each wide-band repeater subsystem of which the TWT constitutes the major load. The nominal output voltage is 22.5 volts. The switch controlling power to the wide-band communications system consists of a pair of transistors controlled from the wide-band command-control unit. The switch thus controls the regulator and its associated load.

### RADIATION EXPERIMENTS

The satellite carries a group of components to obtain data on particle radiation in space; this group is comprised of six radiation detectors and a collection of isolated solar cells and semiconductor diodes. The latter are assembled on a "radiation damage effects" panel. Radiation measurements include:

Protons:	Omnidirectional	35-300 Mev
	Directional	1-8.1 Mev
Electrons:	Directional	0.5-1.2 Mev
		0.25-1.0 Mev

The radiation detectors are included to monitor the proton and electron energy spectra by measuring the flux density in various domains of space. Two of them are scintillation counters, four are p-n semiconductor junctions. Exposure of one of the detectors is omnidirectional, the others are restricted to a small solid angle and are gated by a magnetometer to measure only that flux normal to the earth's magnetic field. Five accumulators in the telemetry encoder count and store the detector outputs; a sixth accumulator registers the background radiation. With the exception of the omnidirectional detector output, the accumulators are reset and the directional detector ranges changed every twelve seconds. These ranges are changed four times, giving a total cycle period of forty-eight seconds.

Thirty silicon solar cells are divided into three groups of nine, plus one group of three. One of the three groups comprises three p-on-n cells protected by a 0.60-inch quartz cover glass, three cells with 0.030-inch covers, and three with no covers. The second of the three groups is similar to the first except that n-on-p cells are used. The third set is again similar except that special reversed p-on-n cells are used. These

last cells have thin bases, and are especially vulnerable to radiation damage. Finally, the last three are special gallium-arsenide p-on-n cells with no quartz protection. One hundred of the 128 telemetry channels are reserved for high-speed measurements of the outputs of the short-circuited cells.

The radiation damage panel contains, in addition to the solar cells, six selected diodes that are used to measure the effect of radiation on minority-carrier lifetime.

The solar-aspect indicator referred to in connection with attitude control was originally designed to use with the radiation-damage-effects panel. Photodiodes mounted behind six slits arranged in simple cyclic binary code provide a measurement of the angle between the sun vector and the spin axis of the satellite. This angle is used in the analysis of the damage effects.

#### EXPERIMENTAL PLAN

The operational sequence is accomplished in two steps. The satellite is first acquired by the NASA test site using the VHF command system. The satellite's 136-mc beacon signal is left on continuously for this purpose. Following acquisition, the spacecraft telemetry is read out and analyzed to determine the condition of the spacecraft. If the temperatures and condition of battery charge are satisfactory, the wide-band repeater and microwave beacon are turned on and the performance evaluated with test signals. Telemetry is continuously monitored by the test site.

The satellite is normally turned off by the test site. If the earth station fails to turn off the spacecraft, a circuit sampling the automatic gain control bus of the wideband repeater will detect a "no carrier" condition and de-energize the wide-band system after two minutes.

The traffic-test operation plan was modified as information accumulated from the experiments. In general, correlation was made between the satellite and ground-station performance so that the characteristics of the transmission medium were measured as well as the satellite performance degradation due to the space environment.

The transmission-medium characteristics measured were attenuation, phase characteristics, interference, noise, time delay and other characteristics of special interest.

The satellite receiver signal strength, telemetry data, and attitude is correlated with ground stations performance (antenna elevation, pointing error, weather conditions, and doppler shift). Typical link performance is shown in Table II.

## EXPERIMENTAL RESULTS

Relay I was launched on December 13, 1962 from the Atlantic Missile Range. Information from the first orbit confirmed that the satellite had achieved the desired orbit. As of January 1964 several hundred scheduled tests had been conducted and an extensive library of data had been accumulated. All classes of telecommunication traffic were transmitted between the United States and Europe, South America, and Asia, including multiplexed telephony, multiplexed telegraphy, and teleprinter exchange (Telex), high-speed data transmission between computers, and television exchanges that appeared before continental television audiences during events of international interest.

There were cooperating earth stations in operation at Andover, Maine and Nutley, New Jersey in the United States, Goonhilly Downs in England, Pleumeur Bodou in France, Fucino in Italy (receiving only), and a transportable station at Rio de Janeiro in Brazil, at the time Relay I was launched. Subsequently, stations that become operational in Germany and in Japan participated in tests with Relay I. The various stations differ in details of capacity and performance, but satisfactory operation was obtained with all of them.

Certain difficulties have been encountered with the Relay I satellite. The most troublesome has been an intermittent failure of a series power transistor in the power-supply voltage regulator that provides regulated voltage to wide-band transponder No. 1 (there are two wide-band transponders). This regulator transistor also acts as a switch to disconnect the wide-band transponder when not in use. The germanium transistor developed sufficiently high leakage current that the No. 1 transponder turned on after launch and could not be turned off. The batteries discharged under the constant high current drain and the satellite was not usable. The leakage was believed to be associated with the dew point of the gas inside the transistor cap. After about two weeks the trouble cleared and the satellite became operational. The trouble reappeared in March 1963 when the satellite was in partial eclipse but cleared again after several days.

One of the three battery strings became inoperative during March because of a defective charge regulator. Due to the redundant circuitry used, the satellite is still completely usable except for a lower duty factor.

Spurious responses by the spacecraft have been observed frequently; that is, equipment sometimes turns on or off without ground command. It is not yet established whether this problem is due to a fault in the satellite or to spurious commands by radiations from ground transmitters such as airport radio control. Thus far it has not been

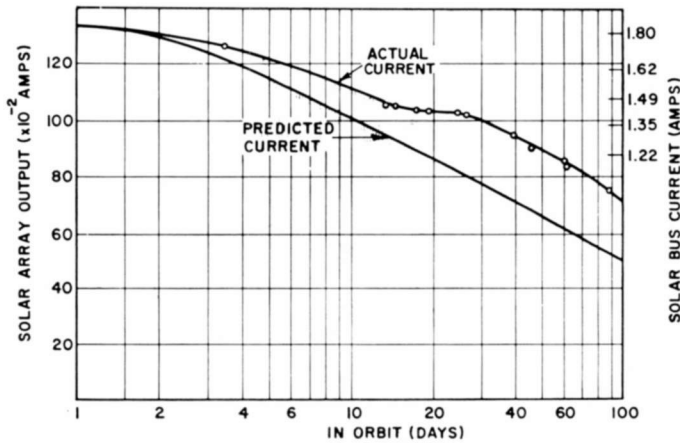


Fig. 16—Plot of predicted and actual current degeneration of p-on-n cells used on Relay I.

possible to duplicate these spurious commands from the ground. However, experiments performed in the laboratory on similar equipment have shown that it is possible for commercial ground transmitters to cause spurious signals under some circumstances. As a result, the command system for Relay II was modified.

Radiation has taken its toll of the spacecraft solar cell systems. Figure 16 shows the comparison of the predicted and actual current degeneration of the p-on-n solar cells as a function of time. Note that the solar-cell array initially had 130 per cent of needed capacity at

Table III—Radiation Damage Effects on Various Solar Cells\*  
(Courtesy Dr. R. C. Woddel, GSFC)

Cell No.	Cell Type	Shield Thickness (inch)	0 days (%)	0.21 day (%)	0.75 day (%)	17.1 days (%)	30.4 days (%)
1, 2, 3	p/n	0	100	56	42	24	24
4, 5, 6	p/n	0.03	100	98	96	76	73
7, 8, 9	p/n	0.06	100	99	98	81	77
10, 11, 12	n/p	0	100	86	66	48	43
13, 14, 15	n/p	0.03	100	98	98	89	88
16, 17, 18	n/p	0.06	100	99	98	92	91
28, 29, 30	GaAs	0	100	77	54	12	12

\* Data corrected for normal illumination, and mean solar distance.

launch based on 100 minutes of operation per day, and that the array capability had decreased to about 70 per cent of needed capacity after 100 days in orbit. This degradation means that the operating duty factor of the satellite must be decreased as time passes. The degradation has been less than expected, probably because the Van Allen radiation is somewhat less than originally estimated. Relay II satellite was fitted with n-on-p solar cells, which are much more resistant to radiation. This second satellite was successfully launched January 21, 1964.

Part of the radiation experiment performed on Relay I consisted of the measurement of radiation damage to various types of solar cells with and without shields (fused silica). Preliminary results are shown in Table III. The table shows the dramatic effect of shielding and indicates that the damaging agent is low-energy electrons or protons. The degradation of the GaAs cells was unexpected.

#### ACKNOWLEDGMENTS

A pioneering project of the scope of the Relay I satellite required the knowledge and skills of many men in NASA and in various divisions of RCA, only a few of whom are named here. Mr. D. Mazur, Chief of the Spacecraft Systems and Projects, GSFC, and Mr. J. Berliner, Project Manager (succeeded by Mr. W. Sunderlin), are the key NASA personnel responsible for the basic planning of the program. Prime contractor was the RCA Astro-Electronics Division, under direct project management of R. M. Wilmotte and R. Dunphy.

# ANALYSIS OF GATE-CONTROLLED SPACE-CHARGE-LIMITED EMISSION PROCESSES IN SEMICONDUCTORS

BY

ROSCOE C. WILLIAMS

RCA Laboratories  
Princeton, N. J.

*Summary*—The mechanism of operation of *p-i-n* units with a gate (hole-injecting device) placed somewhere in the *i* region is investigated. This class of semiconducting devices, termed chargistors, operates by two-carrier injection into a trap-free high-resistivity material. The analysis of the behavior of these devices was assisted by the development of an exact closed-form solution for the *p-i-n* diode using injection parameters.

These exact closed-form solutions were used to construct Green's functions that are valid throughout the intrinsic region. They were used to calculate carrier density distributions, electric fields, and potentials throughout the intrinsic region for chargistors with single or multiple gates. The gates were treated as both point and extended sources. Multiple-gate solutions were found for each case.

The results show that the transconductance of the triode structure increases as the distance between gate and *n-i* junction decreases. An unexpected result is that the transconductance increases as the injection parameter decreases. Transconductances of the order of  $5 \times 10^6$   $\mu\text{mhos}/\text{cm}^2$  are obtainable.

The transit time across the intrinsic region was found to be long ( $\sim 10$   $\mu\text{sec}$  for an *i* region four diffusion lengths long) even though the electric field has values of several hundred volts/cm in the middle of the *i* region.

## INTRODUCTION

THE *p-i-n* diode became an item of interest when Hall<sup>1</sup> showed that forward current in such a device is carried by recombination of electrons and holes that are injected from either side into a relatively thin neutral *i* region. When the structure has insulating (*i*) or semi-insulating (*s-i*) intermediate regions with dimensions large compared to a diffusion length, low-level current flow can be carried in the forward direction by space-charge-limited emission processes.

Space-charge-limited processes have been studied theoretically by

<sup>1</sup>R. N. Hall, "Power Rectifiers and Transistors," *Proc. IRE*, Vol. 40, p. 1512, Nov. 1952; U.S. Patent No. 2,994,018, July 26, 1961.

Lampert and Rose<sup>2-4a</sup> and by Parmenter and Ruppel,<sup>4b</sup> and experimentally by Stafeev,<sup>5-7</sup> Melngailis and Rediker,<sup>8</sup> Holonyak et al,<sup>9</sup> and Larrabee.<sup>10</sup>

Lampert, Rose, Stafeev, Melngailis and Rediker, and Holonyak et al are concerned with the presence of traps in the *i* or (*s-i*) region whose large capture cross section for holes presents a "recombination barrier," i.e., limits the contribution of the holes to the current (thereby limiting the current) until the transit time of the holes approaches their lifetime. Beyond that point the current increases through a negative-resistance region to the "semiconductor regime."

This paper is concerned with the trap-free case, primarily because of the development of a new class of semiconducting devices<sup>11</sup> that rely on two-carrier injection into a trap-free high-resistivity semiconductor material ( $\tau \sim 200 \mu\text{sec}$ ).

The p-i-n diode problem under conditions of large injection ( $n \sim p$ )

---

<sup>2</sup> M. A. Lampert, "A Simplified Theory of Two-Carrier, Space-Charge-Limited Carrier Flow in Solids," *RCA Review*, Vol. 20, p. 682, Dec. 1959.

<sup>3</sup> M. A. Lampert and A. Rose, "Volume-Controlled, Two-Carrier Currents in Solids: The Injected Plasma Case," *Phys. Rev.*, Vol. 121, p. 26, Jan. 1961.

<sup>4a</sup> M. A. Lampert, "Double Injection in Insulators," *Phys. Rev.*, Vol. 125, p. 126, 141, Jan. 1962.

<sup>4b</sup> R. H. Parmenter and W. Ruppel, "Two-Carrier Space-Charge Limited Current in a Trap-Free Insulator," *Jour. Appl. Phys.*, Vol. 30, p. 1548, Oct. 1959.

<sup>5</sup> A. A. Lebedev, V. I. Stafeev, and V. M. Tuchkevich, "Some Properties of Gold-doped Germanium Diodes," *Soviet Phys.—Tech. Phys.*, Vol. 1, p. 2071, Oct. 1957.

<sup>6</sup> V. I. Stafeev, "Modulation of Diffusion Length as a New Principle of Operation of Semiconductor Devices," *Soviet Phys.—Solid State*, Vol. 1, p. 763, Dec. 1959.

<sup>7</sup> V. I. Stafeev, "Photoconductivity in Semiconductor Diodes Induced by Carrier Lifetime Changes," *Soviet Phys.—Solid State*, Vol. 3, p. 1829, March 1962.

<sup>8</sup> I. Melngailis and R. H. Rediker, "Negative Resistance InSb Diodes with Large Magnetic Field Effects," *Jour. Appl. Phys.*, Vol. 33, p. 1892, May 1962.

<sup>9</sup> N. Holonyak, Jr., S. W. Ing, Jr., R. C. Thomas and S. F. Beracque, "Double Injection with Negative Resistance in Semi-insulators," *Phys. Rev. Letters*, Vol. 8, p. 426, June 1, 1962.

<sup>10</sup> R. D. Larrabee, "Current Voltage Characteristics of Forward Biased Long p-i-n Structures," *Phys. Rev.*, Vol. 121, p. 37, Jan. 1961.

<sup>11</sup> H. N. Yu, "The Chargistor, A New Class of Semiconductor Devices," *IBM Jour. Research and Development*, Vol. 5, No. 4, Oct. 1961.

approximation) was first examined by Herlet and Spenke<sup>12</sup> and Kleinman.<sup>13</sup> Kleinman's solution for large injection is dependent upon a parameter of the coordinate system used to describe the p-i-n diode as shown in Figure 1. The injected electron density at  $x = +c$  is denoted by  $n_{+c}$ . The injected hole density at  $x = -c$  is denoted by  $p_{-c}$ . Under the  $n \sim p$  approximation  $p_{-c}$  is then equal to  $n_{-c}$ .

The electron densities  $n_{+c}$  and  $n_{-c}$  are not known for a forward-biased p-i-n diode, i.e., the case where both the p<sup>+</sup>-i and n<sup>+</sup>-i junctions are forward biased. Kleinman developed a one-parameter theory for p-i-n diodes<sup>13</sup> by introducing a parameter  $\gamma_k$  which is the ratio of these unknown electron densities at  $x = \pm c$ , in other words  $\gamma_k = n_{-c}/n_{+c}$ .

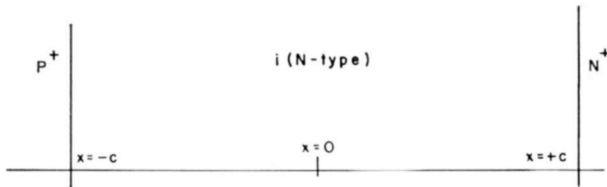


Fig. 1—Coordinate system used to describe the p-i-n diode.

The carrier distributions within the i region,  $-c \leq x \leq +c$ , can only be obtained when  $n_{+c}$  and  $n_{-c}$  are known, or when  $\gamma_k$  is known. Kleinman<sup>13</sup> derived an equation for  $\gamma_k$  that was a fourth-degree polynomial. This equation contains the current as a parameter, hence  $\gamma_k$  depends on the value of the current.

Since the exact solution of a fourth-degree polynomial is cumbersome and impractical, Kleinman used an approximate solution. With this solution the voltage drop across the whole device could be easily obtained for large injection with no recombination since the currents were then constant across the i region, which greatly simplified the analysis. However, for large injection with recombination, the voltage drop involves integrals that are rather involved transcendental functions of  $\gamma_k$ . These integrals must be approximated to find the total voltage drop across the p-i-n diode.

These two facts—(1) the fourth-degree polynomial in  $\gamma_k$  and the

<sup>12</sup> V. A. Herlet and E. Spenke, "Gleichrichter mit p-i-n bzw. mit p-s-n Struktur unter Gleichstrombelastung," *Zeits. für Angew. Physik*, p. 149, Vol. 7, March 1955.

<sup>13</sup> D. A. Kleinman, "The Forward Characteristic of the PIN Diode," *Bell Syst. Tech. Jour.*, Vol. 35, p. 685, May 1956.

necessity to approximate its solution, and (2) integrals for the voltage drop that involve complicated transcendental functions of  $\gamma_k$  that also required approximations, cause considerable difficulty if one intends to use the p-i-n diode solution as the basis for an investigation that uses a p-i-n structure with a third junction (p-i) placed at some arbitrary point in the i region.

These difficulties were overcome in the present investigation by developing an "exact" closed-form solution for the p-i-n diode. What is meant by exact is that for large injection with recombination present, the only approximation involved is the  $n \sim p$  approximation.

The approximations involved in Kleinman's solution to the fourth degree polynomial in  $\gamma_k$  are circumvented because the theory is formulated in such a way that the fourth-degree polynomial does not enter into it.

This was accomplished by introducing a parameter that is well-known in junction theory, namely an injection parameter. The injection parameter for the p-i junction is the ratio of the hole current to the total current, while a similar parameter for the n-i junction is the ratio of the electron current to the total current.

This is then a two-parameter theory, while Kleinman's theory only involves one. However, the advantages gained by using injection parameters are (1) they are parameters which, in principle, can be determined by experiment;\* (2) they remove the two major analytical difficulties discussed above. The exact closed-form solutions obtained in this way can then be used to discuss p-i-n structures with a hole-injecting device placed somewhere in the i region.

This part of the problem is discussed by using Green's functions. The Green's function for the problem is obtained from the exact closed-form solution of the p-i-n diode. The carrier distributions are readily obtained using this Green's function. The effect on these distribution functions of injecting a small number of holes when current is flowing in the i region is brought forth and emphasized when this method of solution is used.

The electric field is then calculated from these distribution functions. This solution for the field shows that the field can be almost completely modulated by injecting a small number of holes, justifying the claim made by Yu<sup>11</sup> that until gate cutoff occurs, the charginistor operates by conductivity modulation.

---

\* While injection parameters are known to be current dependent, for a first approximation they are treated as constant. Values appropriate to the current range of interest are used in the evaluation of the analytic results of this paper.

An exact expression for the voltage appearing at any point along the *i* region is obtained by integrating the electric field from the *n-i* junction to the point of interest. The *n-i* junction is placed at ground potential.

This expression shows that the current varies as  $V^2$  across the intrinsic region, demonstrating a Child's Law behavior for the current, in agreement with Kleinman's<sup>13</sup> results.

Since Yu<sup>11</sup> has demonstrated experimentally that electrostatic shielding exists in the chargistor after gate cutoff has occurred, this fact is used to calculate the transconductance of the device. The results show that the transconductance increases as the distance between gate

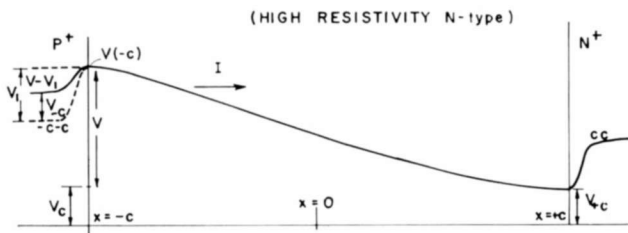


Fig. 2—Variation of potential with distance throughout *i* region of *p-i-n* diode when constant current is flowing.

and *n-i* junction (feeder) decreases, in agreement with Yu's experimental results. An unexpected result is that the transconductance increases as the injection parameters decrease.

Finally, the transit time across the *i* region is calculated using Shockley's<sup>14</sup> definition of transit time. This requires the use of the exact closed-form expression for the electric field. The transit time is long even though the electric field has values of several hundred volts per centimeter in the middle of the *i* region.

#### SOLUTION BY INJECTION PARAMETERS

The boundary conditions for the carrier distributions developed by Kleinman<sup>13</sup> for the *p-i-n* diode will be taken as the starting point. Consider Figure 2. The *p-i* and *n-i* junction interfaces are located at  $x = \mp c$ . The potential, when a constant current is flowing through the device, is shown in the diagram.

<sup>14</sup> W. Shockley and R. C. Prim, "Space-Charge Limited Emission in Semiconductors," *Phys. Rev.*, Vol. 90, No. 5, p. 753, June 1, 1953.

Following Kleinman, points in  $p^+$  and  $n^+$  contacts on the edges of the space-charge regions will be denoted by  $-c-c$  and  $+c+c$ , respectively. Consequently,  $n_{-c-c}$  is the electron density in the  $p^+$  contact at the junction and  $n_{-c}$  is the electron density on the  $i$  side of the same junction. Analogously,  $p_{cc}$  is the hole density on the  $n^+$  side of the junction at  $x = +c$ , while  $p_c$  is the hole density on the  $i$  side of the same junction.

To bring this problem into line with Yu's experiments, the  $i$  region will consist of high-resistivity N-type germanium.

Hence, the equilibrium densities in the  $p^+$ ,  $i$  (or N region) and  $N^+$  region will be denoted by  $n_p^+$ ;  $n_N$ ,  $p_N$ ;  $p_N^+$ .

Kleinman's boundary conditions<sup>12</sup> are, at  $x = \pm c$ ,

$$\begin{aligned} n_{-c-c} &= n_{-c} \left[ \frac{n_p^+}{n_N} \right] \exp \{ \beta V_{-c} \}, \\ n_c &= n_N \exp \{ \beta V_c \}, \\ p_{-c} &= p_N \exp \{ \beta V_{-c} \}, \\ p_{cc} &= p_c \left[ \frac{p_N^+}{p_N} \right] \exp \{ \beta V_c \}. \end{aligned} \tag{1}$$

Since we are concerned with large injection, we can say that the number of injected electrons and holes in the  $i$  region (high-resistivity N-type material) is much greater than the number of uncompensated donors in the  $i$  region. Thus

$$\begin{aligned} n &\gg N, & p &\gg N, \\ n_{-c-c} &\gg n_p^+, & p_{cc} &\gg p_N^+. \end{aligned} \tag{2}$$

We therefore set  $n = p$  everywhere in the  $i$  region. Actually, the statement  $n = p$  is really the Poisson equation for the problem since this is equivalent to saying that  $(1/K)d^2V/dx^2$  is small in comparison to  $n$  and  $p$ , which is true if the electric field is slowly varying throughout the  $i$  region. Since  $n = p$ , we set  $n_c = p_c$  and  $n_{-c} = p_{-c}$  in Equation (1);

$$n_{-c-c} = p_{-c} \left[ \frac{n_p^+}{n_N} \right] \exp \{ \beta V_{-c} \},$$

$$\begin{aligned}
 p_c &= n_N \exp \{ \beta V_c \}, \\
 p_{-c} &= p_N \exp \{ \beta V_{-c} \},
 \end{aligned}
 \tag{3}$$

$$p_{cc} = p_c \left[ \frac{p_{N^+}}{p_N} \right] \exp \{ \beta V_c \}.$$

The current densities  $J_n$  and  $J_p$  are  $J_n = qI_n$  and  $J_p = qI_p$  where  $I_n$  and  $I_p$  have dimensions of particles/cm<sup>2</sup>-sec. Kleinman's boundary condition on the currents were obtained by observing that the minority carrier currents flowed into the contacts by diffusion. Thus

$$\begin{aligned}
 I_p(+c) &= I_{ps} \left\{ \frac{p_{cc}}{p_{N^+}} - 1 \right\} \\
 I_n(-c) &= I_{ns} \left\{ \frac{n_{-c-c}}{n_{p^+}} - 1 \right\},
 \end{aligned}
 \tag{4}$$

where  $I_{ps}$  and  $I_{ns}$  are saturation current densities;

$$\begin{aligned}
 I_{ps} &= \frac{p_{N^+} D_p}{L_p}, \\
 I_{ns} &= \frac{n_{p^+} D_n}{L_n}.
 \end{aligned}
 \tag{5}$$

For large injection conditions, from Equation (2),

$$\frac{n_{-c-c}}{n_{p^+}} \gg 1, \quad \frac{p_{cc}}{p_{N^+}} \gg 1;$$

hence, we can neglect the 1's in Equations (4). Thus,

$$\begin{aligned}
 I_p(+c) &= I_{ps} \left( \frac{p_{cc}}{p_{N^+}} \right), \\
 I_n(-c) &= I_{ns} \left( \frac{n_{-c-c}}{n_{p^+}} \right).
 \end{aligned}
 \tag{6}$$

Combining Equations (3) and (6),

$$I_p(+c) = I_{ps} \left[ \frac{p_c}{p_N} \right] \exp \{ \beta V_c \},$$

$$I_n(-c) = I_{ns} \left[ \frac{p_{-c}}{n_N} \right] \exp \{ \beta V_{-c} \}. \quad (7)$$

Equations (3) and (7) form the basis of the analysis as it does in Kleinman's work except that (7) is in a slightly different form.

We shall now introduce injection parameters. This parameter for the p-i (actually p<sup>+</sup>-N) junction is

$$I_p(-c) = \gamma I,$$

i.e., the hole current is some fraction\*  $\gamma$  of the total current  $I$ . The injection parameter for the n-i (actually N<sup>+</sup>-N) junction is

$$I_n(c) = \xi I.$$

Thus, the electron current at  $x = -c$  is  $I_n(-c) = (1 - \gamma)I$ , while the hole current at  $x = +c$  is  $I_p(+c) = (1 - \xi)I$ . We can therefore write

$$I_p(-c) = \gamma I, \quad I_n(-c) = (1 - \gamma)I,$$

$$I_n(c) = \xi I, \quad I_p(c) = (1 - \xi)I. \quad (8)$$

The unknown carrier densities  $p_c$  and  $p_{-c}$  will now be expressed in terms of the known quantities  $\gamma$ ,  $\xi$ , the total current  $I$ , and the intrinsic carrier concentration  $n_i$  in the i(N) region.

Since  $I_p(+c) = I_{ps} (p_c/p_N) \exp\{\beta V_c\} = (1 - \xi)I$  from Equations (7) and (8),

$$p_c = (1 - \xi) \frac{I}{I_{ps}} p_N \exp\{-\beta V_c\}, \quad (9)$$

---

\* The use of  $\gamma$  as an injection parameter might seem to be confusing since Kleinman uses  $\gamma_i$  as the ratio of the unknown carrier density at the p-i junction interface to that at the n-i junction interface. It should be pointed out, however, that traditionally  $\gamma$  has been known as an injection parameter or emitter efficiency, i.e., the ratio of minority carrier current to total current for a given junction.

From Equation (3),  $p_c = n_N \exp\{\beta V_c\}$ ; therefore

$$n_N \exp\{\beta V_c\} = (1 - \xi) \frac{I}{I_{ps}} p_N \exp\{-\beta V_c\},$$

which yields<sup>†</sup>

$$\exp\{2\beta V_c\} = (1 - \xi) \frac{I}{I_{ps}} \left( \frac{p_N}{n_N} \right). \quad (10)$$

Following a similar procedure, it can be shown that

$$\exp\{2\beta V_{-c}\} = (1 - \gamma) \frac{I}{I_{ns}} \left( \frac{n_N}{p_N} \right). \quad (11)$$

Substituting  $p_c = n_N \exp\{\beta V_c\}$  into Equation (10),

$$p_c = n_N (1 - \xi)^{1/2} \left[ \frac{I}{I_{ps}} \right]^{1/2} \left( \frac{p_N}{n_N} \right)^{1/2} = (1 - \xi)^{1/2} \left[ \frac{I}{I_{ps}} \right]^{1/2} (p_N n_N)^{1/2},$$

$$p_c = n_i (1 - \xi)^{1/2} \left[ \frac{I}{I_{ps}} \right]^{1/2}. \quad (12)$$

Hence we have expressed  $p_c$ , the unknown carrier density at  $x = +c$ , in terms of known quantities, thus circumventing the necessity of solving a quartic equation in the ratio of  $p_{-c}$  to  $p_c$ . Similarly, it can be shown that\*

$$p_{-c} = n_i (1 - \gamma)^{1/2} \left[ \frac{I}{I_{ns}} \right]^{1/2}. \quad (13)$$

#### CARRIER DISTRIBUTIONS AND VARIATIONS IN THE ELECTRIC INTENSITY THROUGHOUT THE INTRINSIC REGION

The complete specification of  $p_c$  and  $p_{-c}$  in terms of known quantities allows the carrier distribution throughout the intrinsic region

<sup>†</sup> The N region is high-resistivity material with a long lifetime; this is why it has been called the *i* region. This means that  $p_N = n_N$ , since the material is quite close to intrinsic. However, to keep things perfectly general, we shall not set  $p_N = n_N$ .

\* The question of whether  $\gamma$  or  $\xi$  can approach unity is examined in Appendix I.

to be obtained. In the intrinsic region the currents satisfy the following equations:

$$I_p(x) = -D_p \frac{dp}{dx} + \beta D_p p E,$$

$$I_n(x) = D_n \frac{dp}{dx} + \beta D_n p E.$$
(14)

$I_n(x)$  is expressed in terms of the hole density  $p$  because of the approximation involved with Poisson's equation, i.e.,  $n = p$ .

The process of recombination is expressed by the equations

$$-\frac{dI_p(x)}{dx} = \frac{dI_n(x)}{dx} = \frac{p}{\tau}.$$
(15)

Differentiating Equations (14), multiplying the first by  $b = D_n/D_p$  and adding it to the second, yields

$$2D_n \frac{d^2p}{dx^2} = \frac{(b+1)}{\tau} p,$$

or

$$\frac{d^2p}{dx^2} = \frac{(b+1)}{2D_n\tau} p.$$

Following Kleinman, let  $L^2 = 2D_n\tau/(b+1)$ .

Then

$$\frac{d^2p}{dx^2} = \frac{p}{L^2}.$$
(16)

The solution to Equation (16) can be written

$$p(x) = A \sinh \left[ \frac{c-x}{L} \right] + B \sinh \left[ \frac{c+x}{L} \right].$$
(17)

The boundary conditions are

at  $x = -c$ ,

$$A = \frac{p_{-c}}{\sinh \frac{2c}{L}},$$

at  $x = +c$ ,

$$B = \frac{p_c}{\sinh \frac{2c}{L}}.$$

If we set  $\lambda = 2c/L$ , where  $\lambda$  is a dimensionless constant,

$$p(x) = \frac{1}{\sinh \lambda} \left[ p_{-c} \sinh \left( \frac{c-x}{L} \right) + p_c \sinh \left( \frac{c+x}{L} \right) \right].$$

Substituting for  $p_{-c}$  and  $p_c$  from Equations (13) and (12), respectively,

$$p(x) = n_i \operatorname{csch} \lambda \left[ \frac{I}{I_{ps}} \right]^{1/2} \left[ \sqrt{\frac{1-\gamma}{R^2}} \sinh \left( \frac{c-x}{L} \right) + \sqrt{1-\xi} \sinh \left( \frac{c+x}{L} \right) \right], \quad (18)$$

where  $R^2 = I_{ns}/I_{ps}$  is a dimensionless constant.  $I_{ns}$  is the saturation current for the p-i junction, while  $I_{ps}$  is the saturation current for the n-i junction. These currents are given by Equation (5). Let  $p(x)/n_i = \bar{P}(x)$  be the hole density divided by the intrinsic carrier concentration. Then

$$\bar{P}(x) = \operatorname{csch} \lambda \left[ \frac{I}{I_{ps}} \right]^{1/2} \left[ \frac{\sqrt{1-\gamma}}{R} \sinh \left( \frac{c-x}{L} \right) + \sqrt{1-\xi} \sinh \left( \frac{c+x}{L} \right) \right]. \quad (19)$$

Figure 3 is a plot of  $\bar{P}(x)$  for  $\xi = \gamma = 0.98$  and for  $\xi = 0.96$  and  $\gamma = 0.98$ . These curves hold for any ratio of the current,  $I$ , to the reverse saturation current  $I_{ps}$  of the n-i (N+-N) junction. The constant  $R^2$ , however, depends on the ratio of the conductivities of N+-N junction to the p+-N junction (see Appendix VI).

The curves have the concave upward characteristic, as shown by Kleinman.<sup>13</sup> Physically this characteristic has the following explanation. Each junction acts as a source for a carrier of a particular sign; since conditions of charge neutrality must exist throughout the intrinsic region, a carrier of opposite sign must be present at a given junction to nullify the charge of the injected carrier. Hence, the

presence of sources for oppositely charged carriers and the condition of charge neutrality lead to high pair densities near the junctions.

As the carriers move away from these sources (junctions) into the body of the intrinsic region, the processes of recombination become dominant and the pair density decreases, leading to a minimum and hence a concave-upward curve.

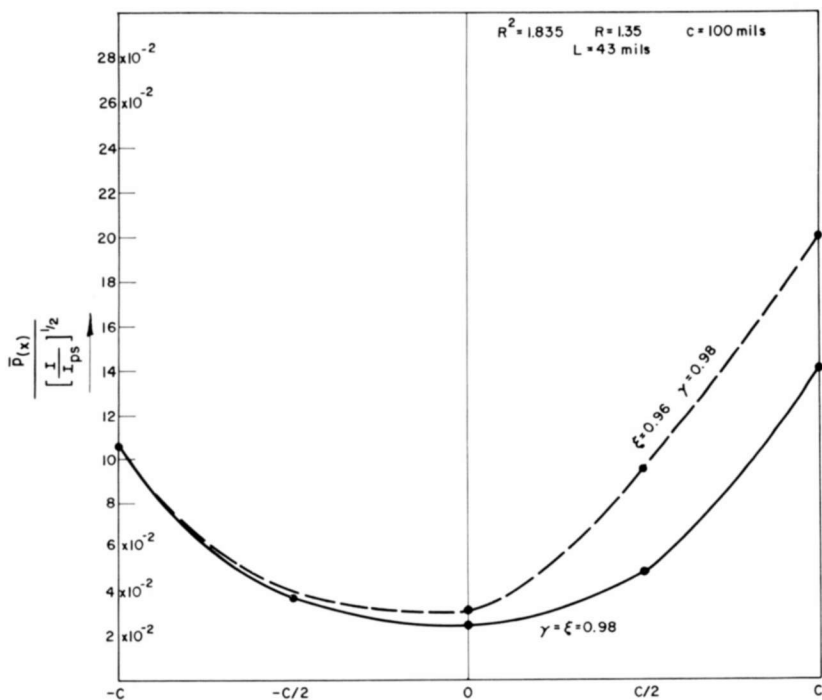


Fig. 3—Plot of pair distribution throughout *i* region,  $-c \leq x \leq c$ , for a p-i-n diode. Note that decreasing the injection parameter  $\xi$  from 0.98 to 0.96 increased the pair density near the n-i junction. The minimum is induced by recombination.

The recombination process is extremely important in this device in that it is the reason why current flows. This was pointed out by Hall.<sup>1</sup> The fact that recombination leads to a minimum also results in a variation in the electric intensity, which enhances conductivity.

The recombination process is a volume-controlled process. Hence, as the volume is increased (the intrinsic region is lengthened), the minimum in the pair density should decrease, thus enhancing the concave-upward characteristic. Conversely, as the volume is reduced, the recombination processes are correspondingly reduced causing the

minimum to move up and the concavity to diminish. In fact, in the limit of small volume or negligible recombination processes, the pair density would be constant across the intrinsic region. All this information is shown quite clearly in Equation (19).

In addition to this, the solution of Equation (19) shows that if the injection parameter  $\xi$  for the n-i (N+-N) junction is decreased, the hole concentration at the n-i junction ( $x = +c$ ) increases. This follows because a decrease in  $\xi$  means that more current at the n-i junction is carried by holes, i.e.,

$$I_p(c) = (1 - \xi)I.$$

Since holes enter the n-i junction by diffusion, an increase in  $I_p(c)$  requires an increase in hole density, as indicated by Equation (19). The charge-neutrality condition that exists throughout the i region requires an increase in the electron concentration if the hole concentration increases. This is brought about by a decrease in the number of electrons leaving the vicinity of the i region near the n-i junction, resulting in a pair-density increase at the n-i junction.

It can be shown that the pair density will increase at the p-i (p+-N) junction if  $\gamma$  is decreased by considering the electron-current increase and its corresponding requirements.

Since the total number of particles/cm<sup>2</sup>/sec flowing through the intrinsic region is a constant given by

$$I = I_p(x) + I_n(x), \quad (20)$$

we can add Equations (14) and solve for the field in terms of  $I$ ,  $p$  and  $dp/dx$ ;

$$\beta E = \frac{bI}{D_n(b+1)p(x)} - \left[ \frac{b-1}{b+1} \right] \frac{1}{p} \frac{dp}{dx},$$

where  $b = D_n/D_p$ . Expressing  $E$  in terms of  $\bar{P}(x)$ , we get

$$\beta E = \frac{bI}{D_n n_i (b+1) \bar{P}(x)} - \left[ \frac{b-1}{b+1} \right] \frac{1}{\bar{P}(x)} \frac{d\bar{P}}{dx}. \quad (21)$$

Figure 4 is a plot of the electric intensity as a function of distance through the intrinsic region, with  $\bar{P}(x)$  given by Equation (19).

The shape of these curves indicates that the field is much smaller

at the junction boundaries than at the center. Since the current is carried primarily by diffusion at these boundaries, this is to be expected. It has been shown that when the injection parameter of one of the junctions is decreased, the pair density near that junction

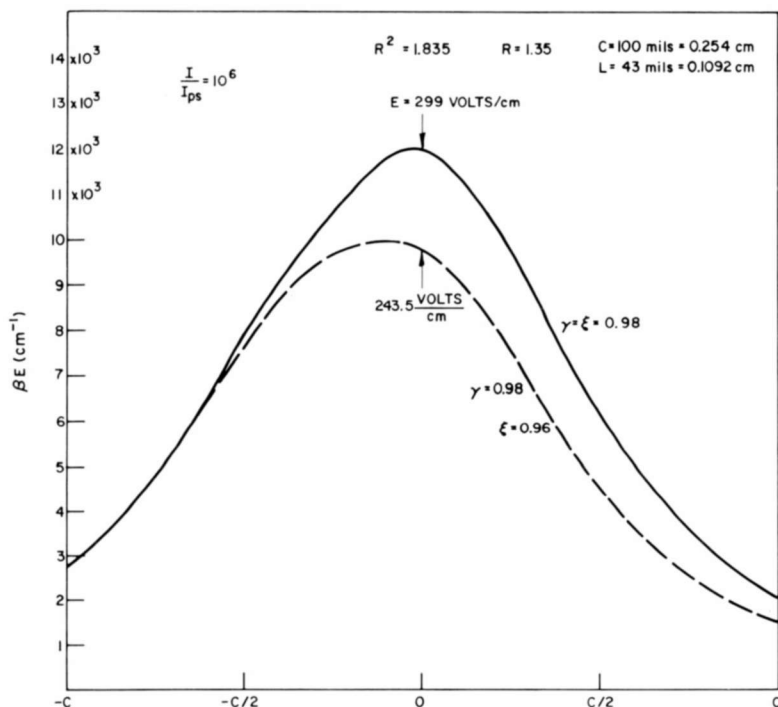


Fig. 4—Plot of the variation in electric field throughout the *i* region. The maximum near the middle of the *i* region is due to the recombination induced minimum in the pair density.

increases. Since the electric intensity is strongly dependent on the reciprocal pair density<sup>\*</sup> the electric intensity decreases as the pair density increases. The strong reciprocal pair density dependence exhibited by the electric intensity explains why it is a minimum at

\* The  $\frac{d}{dx} \ln \bar{P}(x) = \frac{1}{\bar{P}} \frac{d\bar{P}}{dx}$  dependence is weak in comparison with the  $1/\bar{P}(x)$  dependence. In fact,  $\xi = 0.96$ ,  $\gamma = 0.98$  and  $(I/I_{ps})^{1/2} = 10$ , the term involving  $1/\bar{P}(x)$  is three orders of magnitude larger than the term involving  $\frac{1}{\bar{P}} \frac{d\bar{P}}{dx}$ .

the junction interface (large pair density there) and a maximum near the center where the pair density is small because of recombination. Of course, once the large electric field is established in the center of the intrinsic region, it sweeps carriers out of the center, which tends to preserve the minimum in the pair-density distribution.

### V-I CHARACTERISTIC OF THE P-I-N DIODE

The voltage drop between any point  $x$  in the intrinsic region and the n-i junction, which is maintained at ground potential, is obtained by integrating the electric field, which is given by Equation (21), from the n-i junction interface to point  $x$ .

$$\begin{aligned} \beta V_i(x) &= -\beta \int_c^x E dx = \beta \int_x^c E dx \\ &= \frac{bI}{D_n(b+1)} \int_x^c \frac{dx}{p(x)} - \left[ \frac{b-1}{b+1} \right] \ln \left[ \frac{p_c}{p(x)} \right]. \end{aligned} \quad (22)$$

Substituting

$$p(x) = \frac{1}{\sinh \lambda} \left\{ p_{-c} \sinh \left[ \frac{c-x}{L} \right] + p_c \sinh \left[ \frac{c+x}{L} \right] \right\}$$

into Equation (22) and integrating (see Appendix II) yields

$$\begin{aligned} \beta V_i(x) &= \frac{2LbI_{ns}^{1/2} \sinh \lambda \left[ \arctan(A \exp\{\lambda\}) - \arctan \left( A \exp \left\{ \frac{\lambda}{2} \left( 1 + \frac{x}{c} \right) \right\} \right) \right]}{D_n n_i (b+1) (1-\gamma)^{1/2} \left[ 2 \left( \frac{1-\xi}{1-\gamma} \right)^{1/2} R \cosh \lambda - \left( \frac{1-\xi}{1-\gamma} \right) R^2 - 1 \right]^{1/2}} \\ &\quad - \left( \frac{b-1}{b+1} \right) \ln \left( \frac{p_c}{p(x)} \right) \end{aligned} \quad (23)$$

where

$$A = \left[ \frac{R^2(1-\xi) - (1-\gamma) + 2R\sqrt{(1-\xi)(1-\gamma)} \sinh \lambda}{(1-\gamma) \exp\{2\lambda\} - R^2(1-\xi)} \right]^{1/2}$$

By letting

$$F(\xi, \gamma, R; \lambda, x) = \frac{\arctan(A \exp \{\lambda\}) - \arctan \left( A \exp \left\{ \frac{\lambda}{2} \left( 1 + \frac{x}{c} \right) \right\} \right)}{\left[ 2 \left( \frac{1 - \xi}{1 - \gamma} \right)^{1/2} R \cosh \lambda - \left( \frac{1 - \xi}{1 - \gamma} \right) R^2 - 1 \right]^{1/2}},$$

then Equation (23) can be written<sup>†</sup>

$$\beta V_i(x) = \frac{2LbI_{ns}^{1/2} \sinh \lambda}{D_n n_i (b+1) (1-\gamma)^{1/2}} F(\xi, \gamma, R; \lambda, x) I^{1/2} - \left( \frac{b-1}{b+1} \right) \ln \left( \frac{p_c}{p(x)} \right) \quad (26)$$

The square-root dependence of the voltage on the current contained in the first term comes about quite naturally since in Equation (22) the voltage varies directly as the current times a quantity  $K$  (Equation (70), Appendix II). Since  $K$  depends on the reciprocal of the square-root of the current (see Appendix II), the product of current with its reciprocal square-root yields a square-root dependence, i.e., a Child's Law relationship between voltage and current. Notice that no approximations other than the initial  $n = p$  approximation were involved in obtaining this relationship. When  $\xi \neq \gamma$ , the constant  $A$  depends on  $\xi$  and  $\gamma$  along with  $R$ , which is a saturation current ratio. These three parameters are junction parameters while  $\lambda = 2c/L$  is a parameter characteristic of the intrinsic region. A plot of  $F(\xi, \gamma, R; \lambda, x)$  is shown in Figure 5 for the simple case of  $\xi = \gamma$ , since then  $F(\xi = \gamma, \gamma, R; \lambda, x) = F(R; \lambda, x)$ . Since  $\beta V_i(x)$ , aside from certain constant factors, has its  $x$  dependence contained in  $F(\xi = \gamma, \gamma, R; \lambda, x)$ , Figure 5 also shows the manner in which  $\beta V_i(x)$  varies with distance through the intrinsic region.

The voltage drop  $V_i(-c) = V_i$  across the whole intrinsic region is obtained simply by setting  $x = -c$  into Equation (23). The ratio  $p_c/p_{-c}$  in the last term of Equation (23) is given by Equation (73), Appendix II. This yields, for  $V_i$ ,

<sup>†</sup> When the p-i and n-i junctions have equal injection ratios, the constant  $A$  is independent of the injection parameters. Similarly,  $F(\xi = \gamma, \gamma, R; \lambda, x) \equiv F(R; \lambda, x)$ , a function independent of injection parameters.

$$\beta V_i = \frac{2LbI_{ns}^{1/2} \sinh \lambda}{D_n n_i (b+1) (1-\gamma)^{1/2}} F(\xi, \gamma, R; \lambda) I^{1/2} - \left( \frac{b-1}{b+1} \right) \ln \left( \frac{1-\xi}{1-\gamma} \right) \quad (27)$$

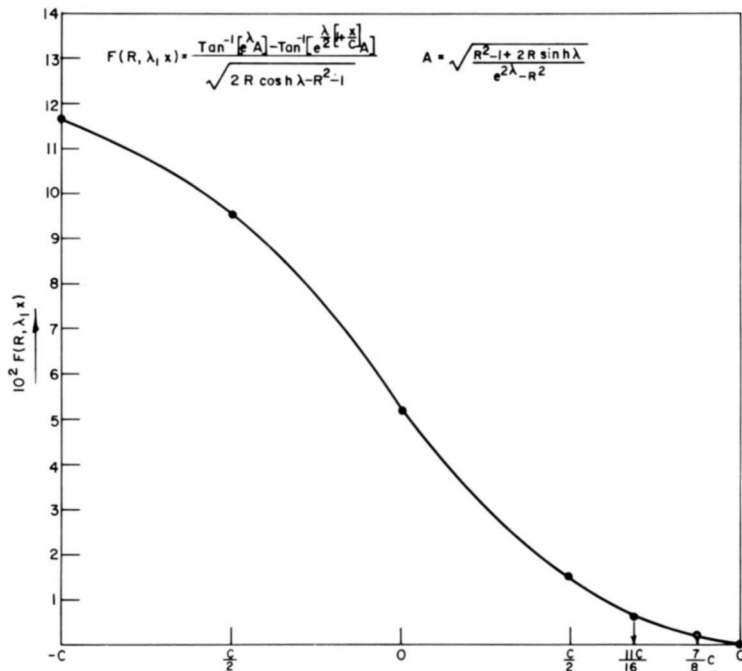


Fig. 5—Variation of  $F(\xi, \gamma, R; \lambda, x)$  throughout *i* region for the simple case of  $\xi = \gamma$ .  $F$  is then  $F(R; \lambda, x)$ , i.e., independent of injection parameters. Since the potential has its  $x$  dependence contained in  $F$ , the above graph, aside from constant factors, shows the manner in which the potential varies with distance throughout the *i* region.

which shows that the voltage drop across the *i* region varies as the square-root of the current. Notice that at  $x = -c$

$$F(\xi, \gamma, R; \lambda, x) = F(\xi, \gamma, R; \lambda).$$

The forward biases  $V_{-c}$  and  $V_c$  across the p-i and n-i junctions can be readily obtained from Equations (10) and (11). From Equation (10),

$$\exp \{\beta V_c\} = (1 - \xi)^{1/2} \left[ \frac{I}{I_{ps}} \right]^{1/2} \left( \frac{p_N}{n_N} \right)^{1/2}. \quad (28)$$

From Equation (11),

$$\exp \{\beta V_{-c}\} = (1 - \gamma)^{1/2} \left[ \frac{I}{I_{ns}} \right]^{1/2} \left( \frac{n_N}{p_N} \right)^{1/2}. \quad (29)$$

Taking the product of Equations (28) and (29) yields the sum of the forward biases across the two junctions:

$$\beta(V_{-c} + V_c) = \frac{1}{2} \ln [(1 - \xi)(1 - \gamma)] + \ln \left[ \frac{I}{(I_{ns} I_{ps})^{1/2}} \right]. \quad (30)$$

Hence, the voltage drop across the junctions varies as the logarithm of the current, as expected. The  $V$ - $I$  characteristic for the p-i-n diode is then the sum of Equations (27) and (30):

$$\beta V = \beta(V_{-c} + V_c + V_i), \quad (31)$$

which contains both a square root and logarithmic dependence on the currents.

#### GREEN'S-FUNCTION SOLUTION OF GATE-CONTROLLED SPACE-CHARGE-LIMITED EMISSION PROCESSES

It was pointed out in the introduction that the injection parameter solution, Equation (19), can be used to discuss p-i-n structures with a gate (hole-injecting device) placed somewhere in the i region.

The Green's-function solution to this problem is obtained using the injection parameter solution. Figure 6 illustrates a p-i-n diode with an injecting electrode situated at some position  $x = l$  in the middle region  $-c < x < +c$ .

The particle-flow Equations (14) hold in this region with the gate present, but the condition for recombination, namely Equation (15), must be modified to take into account the fact that generation now exists because of the gate.\* Thus,

$$\frac{dI_n(x)}{dx} = -\frac{dI_p(x)}{dx} = \frac{p}{\tau} - \frac{f(x)}{\tau}, \quad (32)$$

\* The gate could be a p-i junction, n-i junction, metal-semiconductor contact, or even a light source capable of generating carriers.

where the generating source is represented by  $f(x)$ . Differentiating Equations (14) with respect to  $x$  and equating each to the right-hand side of Equation (32) yields

$$-\frac{dI_p(x)}{dx} = D_p \frac{d^2p}{dx^2} - \beta D_p \frac{d}{dx} (pE) = \frac{p}{\tau} - \frac{f(x)}{\tau}, \quad (33)$$

$$\frac{dI_n(x)}{dx} = D_n \frac{d^2p}{dx^2} + \beta D_n \frac{d}{dx} (pE) = \frac{p}{\tau} - \frac{f(x)}{\tau}. \quad (34)$$

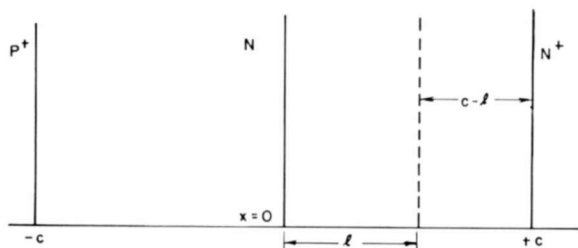


Fig. 6—Diagram of p-i-n diode with an injecting electrode situated at some position  $x = l$  in the i region.

Multiplying Equation (33) by  $b = D_n/D_p$  and adding it to Equation (34) eliminates the term involving  $d(pE)/dx$ , resulting in the equation

$$\frac{d^2p}{dx^2} - \frac{p}{L^2} = -\frac{f(x)}{L^2}, \quad (35)$$

where

$$L^2 = \frac{2D_n\tau}{b+1}.$$

Hole generation occurs in the following manner. The current through the device is held constant thus fixing the carrier concentrations at the end. The holes injected through the gate lead to an increase in carrier concentration, which in turn should lead to a decrease in the field since the field strength is inversely proportional to the carrier concentration. The decrease in field strength should result in a decrease in the voltage drop across the intrinsic region.

The differential Equation (35) must be solved with the distribution of the generated or injected carriers  $f(x)$  known and with the bound-

ary conditions of Equations (12) and (13). Since the current is held constant, this fixes the carrier concentrations at  $x = \pm c$ .

The gate will first be considered as a point source. Once the solution for a point source is obtained, the solution for an extended source, i.e., gate of finite width, can be obtained from the point-source solution. The extended-source solution is obtained by the usual technique of multiplying the point-source solution by the intensity of the extended source and integrating the product over the extended-source area. The intensity of the extended source will usually be a function of position, and must be specified.

### Point-Source Solution

When the gate is a point source of unit strength,

$$f(x) = \delta(x-l). \quad (36)$$

Equation (35) then becomes

$$\frac{d^2p}{dx^2} - \frac{p}{L^2} = -\frac{1}{L^2} \delta(x-l), \quad (37)$$

with the boundary conditions of Equations (12) and (13) to be satisfied. It has been shown that  $\bar{P}(x)$ , given by Equation (19), is a solution to Equation (16) subject to the boundary conditions;

$$\frac{d^2\bar{P}}{dx^2} - \frac{\bar{P}}{L^2} = 0. \quad (38)$$

Subtracting Equation (38) from Equation (37) yields

$$\frac{d^2\phi(x)}{dx^2} - \frac{\phi(x)}{L^2} = -\frac{1}{L^2} \delta(x-l), \quad (39)$$

where  $\phi(x) = p(x) - \bar{P}(x)$ .

Since we are considering a constant-current solution,  $p(x)$  and  $\bar{P}(x)$  are equal at the junctions; thus  $p(-c) = p_{-c} = \bar{P}(-c)$ , and  $p(+c) = p_c = \bar{P}(+c)$ , which leads to the following boundary conditions on  $\phi(x)$ :

$$\phi(-c) = \phi(+c) = 0. \quad (40)$$

Hence, we have transformed the problem from one of obtaining a

solution to Equation (37) subject to the boundary conditions of Equations (12) and (13) to one where we must obtain a solution to Equation (39) subject to the boundary conditions of Equation (40).

If a Green's function can be found for the problem, then a solution to Equation (39) would be\*

$$\phi(x) = \frac{1}{L^2} \int_{-c}^{+c} G(x, \zeta) \delta(\zeta - l) d\zeta = \frac{1}{L} G(x, l). \quad (41)$$

Since  $\phi(x) = p(x) - \bar{P}(x)$ , then the solution to Equations (37) subject to the boundary conditions of Equations (12) and (13) will be, using Equations (41),

$$p(x) = \bar{P}(x) + \frac{1}{L} G(x, l), \quad (42)$$

where  $\bar{P}(x)$  is given by Equation (19). In order to find the Green's function, Equation (41), we must solve

$$\frac{d^2 G(x, \zeta)}{dx^2} - \frac{G(x, \zeta)}{L^2} = -\delta(x - \zeta) \quad (43)$$

subject to the boundary conditions

$$G(-c, \zeta) = G(+c, \zeta) = 0. \quad (44)$$

This solution is constructed in Appendix III where it is shown that

$$\begin{aligned} G(x, \zeta) &= \frac{L}{\sinh \lambda} \sinh \left[ \frac{c+x}{L} \right] \sinh \left[ \frac{c-\zeta}{L} \right], & x < \zeta, \\ G(x, \zeta) &= \frac{L}{\sinh \lambda} \sinh \left[ \frac{c-x}{L} \right] \sinh \left[ \frac{c+\zeta}{L} \right], & x > \zeta. \end{aligned} \quad (45)$$

---

\*  $\phi(x)$  integrates into  $\frac{1}{L} G(x, l)$  and not  $\frac{1}{L^2} G(x, l)$  because the argument of the Green's function is really

$$G(x, \xi) = G\left(\frac{x}{L}, \frac{\xi}{L}\right)$$

Thus, the point-source solution to Equation (37), subject to boundary conditions of Equations (12) and (13), is given by Equation (42), where  $\bar{P}(x)$  is given by Equation (19) and  $G(x, l)$  is given by Equation (45) with  $\zeta = l$ .

If the point source is of strength  $\bar{P}_G$ , i.e., if a hole density of  $\bar{P}_G = P_G/n_i$  is injected at the gate, then multiplication of Equation (45) by  $\bar{P}_G$  yields the solution. The closed-form solution for a gate that acts as a point source of strength  $\bar{P}_G$  is

$$\begin{aligned}
 p(x) &= \operatorname{csch} \lambda \left[ \frac{I}{I_{ps}} \right]^{1/2} \left[ \frac{\sqrt{1-\gamma}}{R} \sinh \left[ \frac{c-x}{L} \right] + \sqrt{1-\xi} \sinh \left[ \frac{c+x}{L} \right] \right] \\
 &+ \frac{\bar{P}_G}{\sinh \lambda} \sinh \left[ \frac{c-l}{L} \right] \sinh \left[ \frac{c+x}{L} \right], \quad x < l, \\
 p(x) &= \operatorname{csch} \lambda \left[ \frac{I}{I_{ps}} \right]^{1/2} \left[ \frac{\sqrt{1-\gamma}}{R} \sinh \left[ \frac{c-x}{L} \right] + \sqrt{1-\xi} \sinh \left[ \frac{c+x}{L} \right] \right] \\
 &+ \frac{\bar{P}_G}{\sinh \lambda} \sinh \left[ \frac{c+l}{L} \right] \sinh \left[ \frac{c-x}{L} \right], \quad x > l. \quad (46)
 \end{aligned}$$

### N-Gate Solution

If more than one gate is present, i.e., if tetrode or pentode chargistors<sup>11</sup> are being considered, the above analysis is easily extended to cover a multiple-gate structure. Let  $N$  be the number of gates present, each gate acting as a unit point source. Let the gate nearest the n-i junction be called  $G_1$  and denote its position as  $x = l_1$ . The second gate from the n-i junction will be called  $G_2$  and its position will be denoted by  $l_2$  and so on up to  $G_N$  at position  $l_N$ .

The intensity distribution function  $f(x)$  will be given by

$$f(x) = \sum_{j=1}^N \delta(x - l_j). \quad (47)$$

Equation (35) becomes

$$\frac{d^2 p}{dx^2} - \frac{p}{L^2} = -\frac{1}{L^2} \sum_{j=1}^N \delta(x - l_j). \quad (48)$$

Following the procedure for obtaining the differential equation and boundary conditions for the Green's function outlined above, one obtains

$$\frac{d^2}{dx^2} G(x, \xi_1, \xi_2, \dots, \xi_N) - \frac{G(x, \xi_1, \xi_2, \dots, \xi_N)}{L^2} = - \sum_{j=1}^N \delta(x - \xi_j), \quad (49)$$

subject to the boundary conditions

$$G(-c, \xi_1, \xi_2, \dots, \xi_N) = G(+c, \xi_1, \xi_2, \dots, \xi_N) = 0. \quad (50)$$

Since Equation (49) is a linear differential equation, the effects of the individual gates are additive. Hence, we can find the Green's function for each particular gate and sum them to obtain the total Green's function for the system. In particular, Equation (45) gives the Green's function for the  $j$ th gate if  $\xi$  is replaced by  $\xi_j$ ;

$$G_j(x, \xi_j) = \frac{L}{\sinh \lambda} \sinh \left[ \frac{c+x}{L} \right] \left[ \frac{c-\xi_j}{L} \right], \quad x < \xi_j, \quad (51)$$

$$G_j(x, \xi_j) = \frac{L}{\sinh \lambda} \sinh \left[ \frac{c-x}{L} \right] \sinh \left[ \frac{c+\xi_j}{L} \right], \quad x > \xi_j.$$

Hence, the Green's function for  $N$  gates is obtained by summing over all of the gates, i.e.,

$$G(x, \xi_1, \xi_2, \dots, \xi_N) = \sum_{j=1}^N G_j(x, \xi_j), \quad (52)$$

where the  $G_j(x, \xi_j)$  are given by Equation (51).

The  $N$ -gate solution to Equation (48), subject to boundary conditions of Equations (12) and (13) is given by

$$p(x) = \bar{P}(x) + \frac{1}{L} G(x, l_1, l_2, \dots, l_N), \quad (53)$$

where  $\bar{P}(x)$  is given by Equation (19) and  $G(x, l_1, l_2, \dots, l_N)$  is given by Equation (52) with  $\xi_j = l_j$ ,  $j = 1, 2, \dots, N$ .

The triode solution is given by Equation (46). The tetrode and pentode solutions are given by Equation (53) with  $N = 2$  and  $3$ , respectively.

**Extended-Gate Solution**

The solution for the case where the gate is an extended source is obtained in Appendix IV. Obviously, a variety of intensity distribution functions  $f(x)$  could be examined through Equation (80) with the possibility that each intensity distribution might affect the hole distribution in a different way.

As an example of this, it is shown in Appendix IV that when the source intensity is constant over the source extension, i.e.,  $f(x)$  is given by Equation (81), then

$$\begin{aligned} \phi(x) = \frac{\bar{P}_G}{\sinh \lambda} & \left\{ \sinh \left[ \frac{c+x}{L} \right] \cosh \left[ \frac{c-l+\epsilon}{L} \right] \right. \\ & \left. + \sinh \left[ \frac{c-x}{L} \right] \cosh \left[ \frac{c+l+\epsilon}{L} \right] \right\} - \bar{P}_G. \end{aligned} \quad (84)$$

The closed-form solution is given by

$$p(x) = \bar{P}(x) + \phi(x). \quad (54)$$

where  $\bar{P}(x)$  is given by Equation (19) and  $\phi(x)$  by Equation (84).

When the source intensity varies as a half-period sinusoid over the source extension, i.e.,  $f(x)$  is given by Equation (86), then

$$\begin{aligned} \phi(x) = \frac{\bar{P}_G \left( \frac{\pi L}{2\epsilon} \right) \operatorname{csch} \lambda}{\left[ 1 + \frac{\pi^2 L^2}{4\epsilon^2} \right]} & \left\{ \sinh \left[ \frac{c-l+\epsilon}{L} \right] \sinh \left[ \frac{c+x}{L} \right] \right. \\ & \left. + \sinh \left[ \frac{c+l+\epsilon}{L} \right] \sinh \left[ \frac{c-x}{L} \right] \right\} - \frac{\bar{P}_G \sin \left[ \frac{\pi(x-l+\epsilon)}{2\epsilon} \right]}{\left[ 1 + \frac{\pi^2 L^2}{4\epsilon^2} \right]} \end{aligned} \quad (89)$$

The closed form solution is again given by Equation (54) with  $\bar{P}(x)$  given by Equation (19) and  $\phi(x)$  by Equation (89).

Evidently Equations (84) and (89) differ markedly in form; this points out the necessity of taking into account the fact that, in general,

the gate will not only be extended, but its intensity will vary over its extension.

Extended  $N$ -gate solutions can be obtained for variable or constant intensity sources by substituting the  $N$ -gate Green's function, Equation (52), into Equation (80) and integrating. The result is, for an extended gate with constant intensity over its extension, a sum of

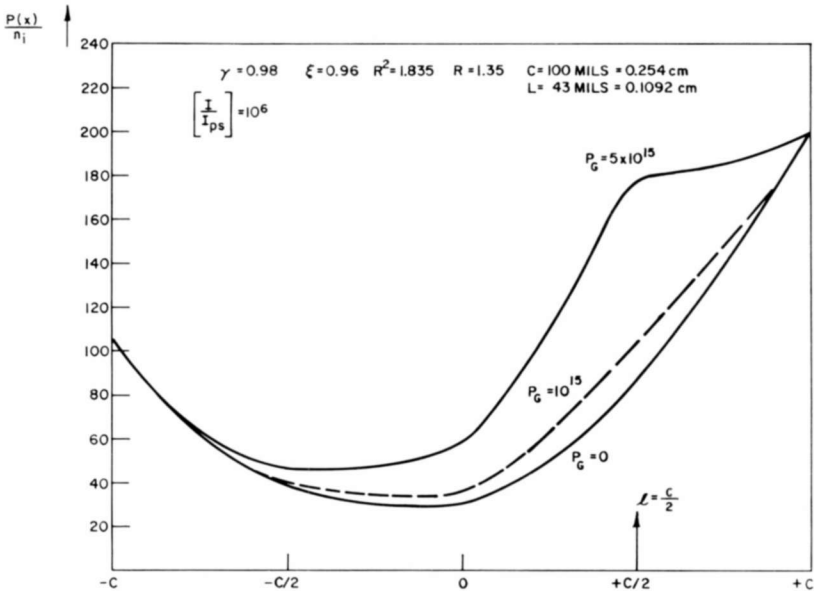


Fig. 7—Plot of the pair density distribution curve throughout  $i$  region for the triode structure for three different values of the pair densities injected at the gate. Note that when  $P_G = 10^{15}$  the deviation of the distribution curve from the  $p$ - $i$ - $n$  diode solution ( $P_G = 0$ ) is slight.

functions similar to Equation (84) with  $l$  and  $\epsilon$  replaced by  $l_j$  and  $\epsilon_j$ ;  $j = 1, 2, 3, \dots, N$ .  $\bar{P}_G$ , of course, is replaced by  $\bar{P}_{Gj}$ . For an extended gate with a half-sinusoid variation in intensity over its extension, the result is a sum of functions similar to Equation (89) with  $\bar{P}_G$ ,  $l$  and  $\epsilon$  replaced by  $\bar{P}_{Gj}$ ,  $l_j$  and  $\epsilon_j$ .  $j = 1, 2, 3, \dots, N$ .

A plot of the hole density for a triode structure is shown in Figure 7 for three different values of the injected hole density— $P_G = 0$ ,  $P_G = 10^{15}$ , and  $P_G = 5 \times 10^{15}$  holes/cm.<sup>3</sup>

The gate is placed at  $c/2$ . The following values were used:  $c = 100$  mils and  $L = 43$  mils, so that the gate location is just over a diffusion length away from the  $n$ - $i$  junction. When  $P_G = 0$ , the hole distribution

curve is that of a p-i-n diode. When  $P_G = 10^{15}$ , the curve begins to depart from the p-i-n diode distribution, but not appreciably. This shows that even though the injected hole density exceeds the intrinsic carrier concentration  $n_i$  by an order of magnitude, the effects of recombination are so great a diffusion length away from the n-i junction that these additional holes do not produce any great effect on the hole distribution until their density reaches that of the holes at the n-i junction itself.

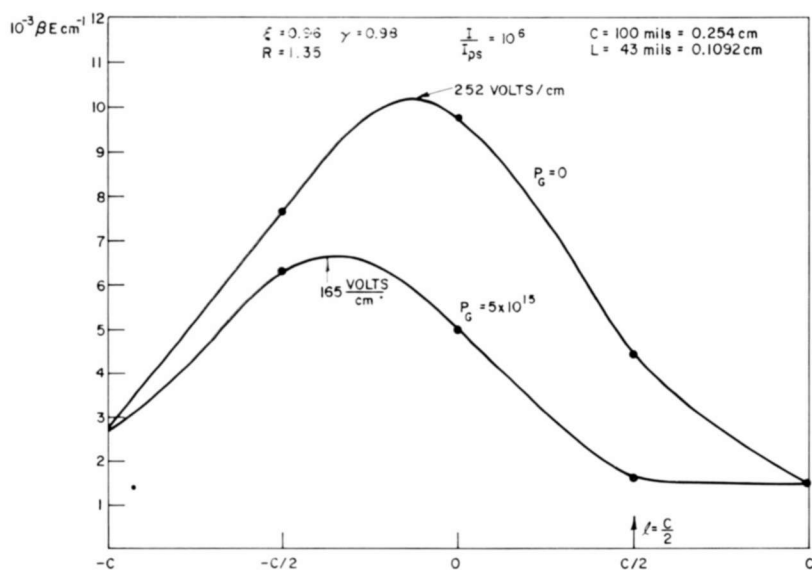


Fig. 8—Plot of the variation in the electric intensity throughout  $i$  region for two different values of the hole densities injected at the gate. The severe reduction in field for  $P_G = 5 \times 10^{15}$  constitutes conductivity modulation.

Recombination is not the only factor that reduces the effect of the injected holes at the gate. The electric field is much larger at the gate than it is at the n-i junction. Figure 4 shows that if the gate is located at  $c/2$ , the field is about three times larger there than it is at the n-i junction. This field sweeps the holes toward the n-i junction, preventing any accumulation at the gate. Only when the field at the gate is comparable to the field at the n-i junction will this effect stop. Figure 8 shows this is indeed true when  $P_G = 5 \times 10^{15}$ , because then the field at the gate is very nearly equal to the field at the n-i junction. The holes can now accumulate at the gate once they overcome the effects of recombination. This is brought out by Figure 7.

The electric field that is plotted in Figure 8 is obtained by substi-

tuting  $p(x)$  given by Equation (46) for  $\bar{P}(x)$  in Equation (21). This is the electric field that belongs to the triode solution.

The electric field that belongs to an extended gate with a constant source intensity is obtained by substituting  $p(x)$  given by Equation (54) for  $\bar{P}(x)$  in Equation (21), while the field belonging to an extended gate with a source intensity varying as a half-period sinusoid is obtained by substituting  $p(x)$  given by Equation (54) for  $P(x)$  in Equation (21).

The electric field belonging to the various  $N$ -gate solutions, Equation (53), and the extended  $N$ -gate solutions discussed above is obtained by substituting the hole density given by the appropriate  $N$ -gate solution for  $\bar{P}(x)$  into Equation (21).

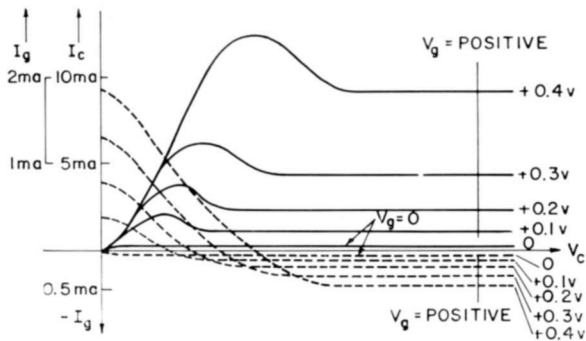


Fig. 9—Current-voltage characteristics of a triode structure as determined by Yu.<sup>11</sup>  $I_g$ ,  $V_g$  are the gate current and voltage, respectively, while  $I_c$  and  $V_c$  are the charger ( $p^+ - i$ ) current and voltage.

### TRANSCONDUCTANCE

The transconductance of the chargistor will be calculated as an example of how the analysis can be applied to a given set of circumstances. Figure 9 is a set of output characteristics of a triode structure.<sup>11</sup> Notice that these characteristics can be divided into three separate regions.

- I. A Child's-law region where the current varies as the square of the output voltage.
- II. A negative-resistance region.
- III. A constant-current region.

The Child's-law region has been discussed extensively in the preceding part of this paper. This is the region where conductivity modulation occurs, as shown by Figures 7 and 8.

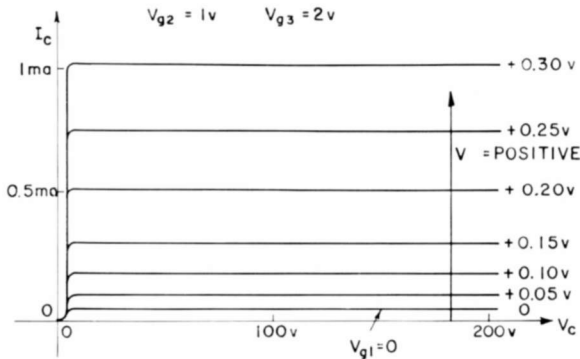


Fig. 10—Current-voltage characteristic of a pentode structure.<sup>11</sup>  $I_c$  and  $V_c$  are the current and voltage at the charger ( $p^+ - i$  junction), while  $V_{gi}$  ( $i = 1, 2, 3$ ) are the various gate voltages.

The negative-resistance region has not been discussed because the physical mechanisms that cause it are not as yet well understood.

The constant-current region is of interest and will be discussed because the tetrode and pentode structures exhibit excellent constant-current characteristics<sup>11</sup> (see Figure 10).

Calculation of the transconductance of such a constant-current device is based on the following observed characteristic. Once the potential at the gate inside the intrinsic material,  $V_i(x=l)$ , exceeds the bias applied to the gate,  $V_g$ , the potential  $V_i(l)$  remains locked at  $V_g$  regardless of any variation in voltage  $V_c$  at the output. This means that the current is completely determined by the voltage applied to gate. This result is illustrated by Yu's potential-distance plots shown in Figure 11. Notice that not only is the potential  $V_i(l)$  constant and held at the gate bias voltage,  $V_g$ , independently of the output voltage,

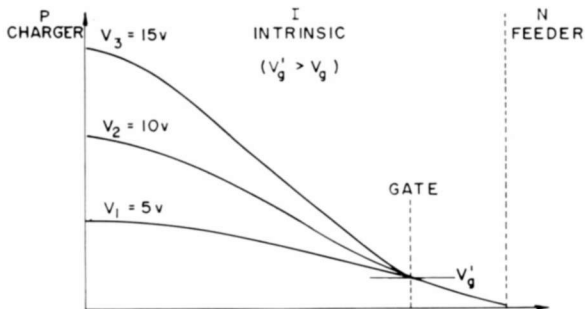


Fig. 11—Plot of variation in potential throughout the intrinsic region for a triode structure with the gate cut off as determined empirically by Yu.<sup>11</sup>

$V_c$ , but the potential variation  $V_i(x)$ , for  $l < x < c$ , is the same as when  $V_i(l) \rightarrow V_g$ .

This implies that the plane  $x = l$  is an equipotential plane and remains so after the onset of saturation. It should be clearly understood that this is not an attempt to explain the physical processes that result in saturation. The observation that  $V_i(x)$  for  $l < x < c$  is independent of  $V_c$  when  $V_i(l) = V_g$  is sufficient information to allow the transconductance to be calculated, because  $V_i(l)$  is given by Equation (26) with  $x = l$ .

The voltage at the gate  $V_g$  is then equal to  $V_i(x = l)$ , which is now given by Equation (26). Now  $F(\xi, \gamma, R; \lambda, l)$  is known, and in fact is given by Equation (25) with  $x = l$ . The hole density  $p(x = l)$  that appears in the last term of Equation (26) will be given by Equation (46) with  $\bar{P}_G = 0$ , i.e.,  $p(x = l) = \bar{P}(l)$ ;

$$p(x = l) = \bar{P}(x = l) = \operatorname{csch} \lambda \left[ \frac{I}{I_{ps}} \right]^{1/2} \left[ \frac{\sqrt{1 - \gamma}}{R} \sinh \left[ \frac{c - l}{L} \right] + \sqrt{1 - \xi} \sinh \left[ \frac{c + l}{L} \right] \right], \quad (55)$$

and

$$\frac{p_c}{p(x = l)} = \frac{p_c}{\bar{P}(x = l)} = \frac{n_i(1 - \xi)^{1/2}}{\operatorname{csch} \lambda \left[ \frac{\sqrt{1 - \gamma}}{R} \sinh \left[ \frac{c - l}{L} \right] + \sqrt{1 - \xi} \sinh \left[ \frac{c + l}{L} \right] \right]}, \quad (56)$$

where  $p_c$  is given by Equation (13). The ratio  $p_c/\bar{P}(x = l)$  is independent of current and depends on  $\xi$  and  $\gamma$ ,  $n_i$ ,  $R$ , and  $l$ .

Let

$$\left( \frac{b - 1}{b + 1} \right) \ln \left[ \frac{p_c}{\bar{P}(x = l)} \right] = h, \quad (57)$$

a constant independent of current. Then

$$\beta V_i(l) = \beta V_g = \frac{2LbI_{ns}^{1/2} \sinh \lambda}{D_n n_i (b + 1) (1 - \gamma)^{1/2}} F(\xi, \gamma, R; \lambda, l) I^{1/2} - h. \quad (58)$$

This can be put in the form

$$\beta V_g = \alpha F(\xi, \gamma, R; \lambda, l) \left[ \frac{I}{I_{ps}} \right]^{1/2} - \hbar, \quad (59)$$

where

$$\alpha = 2 \left[ \frac{I_{ps}}{D_n n_i} \right] \frac{b}{b+1} \frac{R}{(1-\gamma)^{1/2}} \sinh \lambda. \quad (60)$$

Solving Equation (59) for the current yields

$$I = I_{ps} \left[ \frac{\beta V_g + \hbar}{\alpha F} \right]^2. \quad (61)$$

The transconductance of the device  $g_m$  is defined by

$$g_m = \frac{\partial(qI)}{\partial V_g}. \quad (62)$$

Multiplying Equation (61) by  $q$ , the charge on a hole and differentiating the result with respect to  $V_g$  gives

$$g_m = \frac{2q\beta I_{ps}}{\alpha F} \left( \frac{\beta V_g + \hbar}{\alpha F} \right) = \frac{2q\beta I_{ps}}{\alpha F} \left( \frac{I}{I_{ps}} \right)^{1/2}. \quad (63)$$

When  $I = I_{ps}$ ,

$$g_m(I_{ps}) = g_{mps} = \frac{2q\beta I_{ps}}{\alpha F}, \quad (64)$$

and

$$g_m = g_{mps} \left( \frac{I}{I_{ps}} \right)^{1/2}. \quad (65)$$

Equation (64) shows that  $g_m$  is inversely proportional to the product  $\alpha F$ . If  $\alpha$  is evaluated from Equation (60) using  $I_{ps} = 10^{15}$  particles/cm<sup>2</sup>sec,  $b = D_n/D_p = 2.115$ ,  $L = 0.1092$  cm,  $n_i = 2.5 \times 10^{13}$ /cm<sup>3</sup>,  $D_n = 93$  cm<sup>2</sup>/sec, then

$$\alpha = \frac{4.125}{(1 - \gamma)^{1/2}}. \quad (66)$$

Then from Equation (64),

$$g_{mps} = \frac{1.938 \times 10^{-5} (1 - \gamma)^{1/2}}{F}. \quad (67)$$

As indicated earlier, when  $\xi = \gamma$ ,  $F$  is independent of injection parameters. Hence, the transconductance will depend on the injection parameters through  $\alpha$  which, from Equations (60) and (66), varies as  $(1 - \gamma)^{-1/2}$ . Hence,  $g_m$  varies as  $(1 - \gamma)^{1/2}$  as shown in Equation (67). Therefore, as the injection parameters decrease, the transconductance increases.

Equation (67) shows that  $g_m$  varies inversely as  $F$ , which causes it to increase as the gate approaches the n-i junction since

$$F(R; \lambda, x) \rightarrow 0 \text{ as } x \rightarrow c.$$

Figure 12 is a plot of  $g_m$  versus  $(I/I_{ps})^{1/2}$ . It can be seen that the closer the gate is to the n-i junction, the larger the  $g_m$ . Also, keeping the gate position constant but decreasing the injection parameter increases the  $g_m$ .

#### TRANSIT TIME

The triode transit time was calculated using Shockley and Prim's<sup>14</sup> definition;

$$t = \int_{-c}^c \frac{dx}{\mu_p E}. \quad (68)$$

This is evaluated in Appendix E, where it is shown that

$$t = \frac{\beta(b+1)L^2}{(b-1)\mu_p} \ln \left[ \frac{1 - \frac{D_n(b-1)}{bI} \left( \frac{dp}{dx} \right)_{x=-c}}{1 - \frac{D_n(b-1)}{bI} \left( \frac{dp}{dx} \right)_{x=c}} \right], \quad (69)$$

where  $dp/dx$  evaluated at  $x = \pm c$ , the junction interfaces, is obtained by differentiating Equation (18), which is the solution when  $P_G = 0$ .

Figure 13 is a plot of transit time versus particle density for the case of  $\xi = \gamma = 0.64$ . As the particle density increases, the transit

time settles in around the value of 10  $\mu$ sec, hence at these currents one would expect the device to oscillate at frequencies of the order of 100 kilocycles. This is what Yu<sup>11</sup> observed.

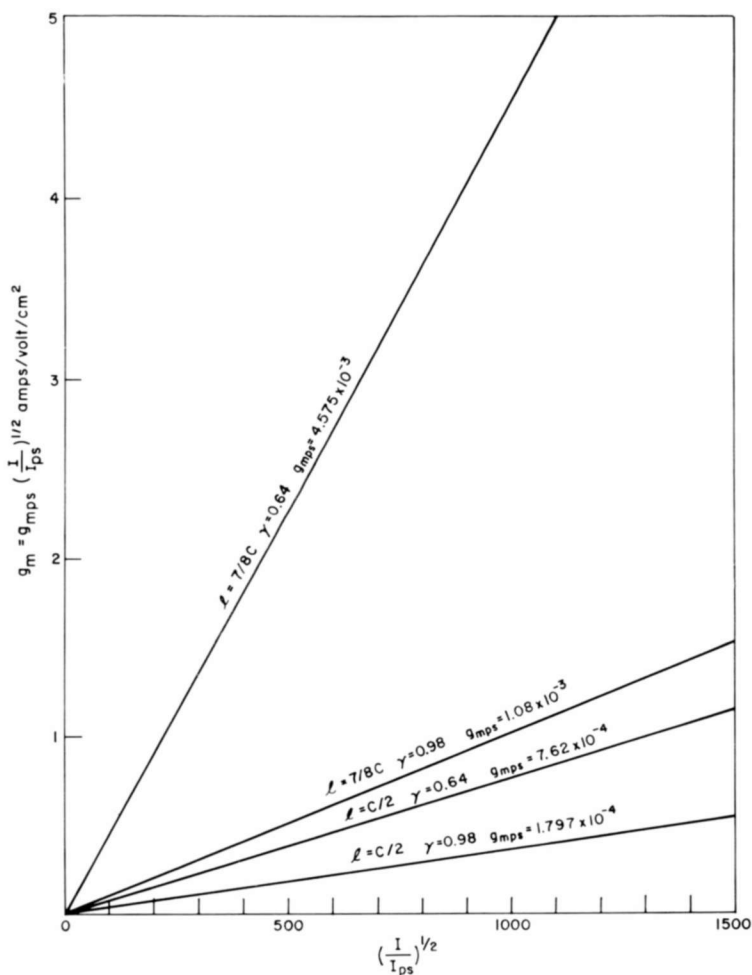


Fig. 12—Transconductance,  $g_m$ , versus  $(I/I_{ps})^{1/2}$  for various  $\gamma$ 's and gate positions.

#### ACKNOWLEDGMENTS

The author is deeply indebted to Harwick Johnson of these Laboratories for his encouragement.

## APPENDIX I

The question of whether  $\gamma$  or  $\xi$  can approach unity is considered. Suppose  $\gamma = 1$ ; then since  $I_p(-c) = \gamma I = I$ , all the current at  $x = -c$ , i.e., through the p-i (p<sup>+</sup>-N) junction, is carried by holes.

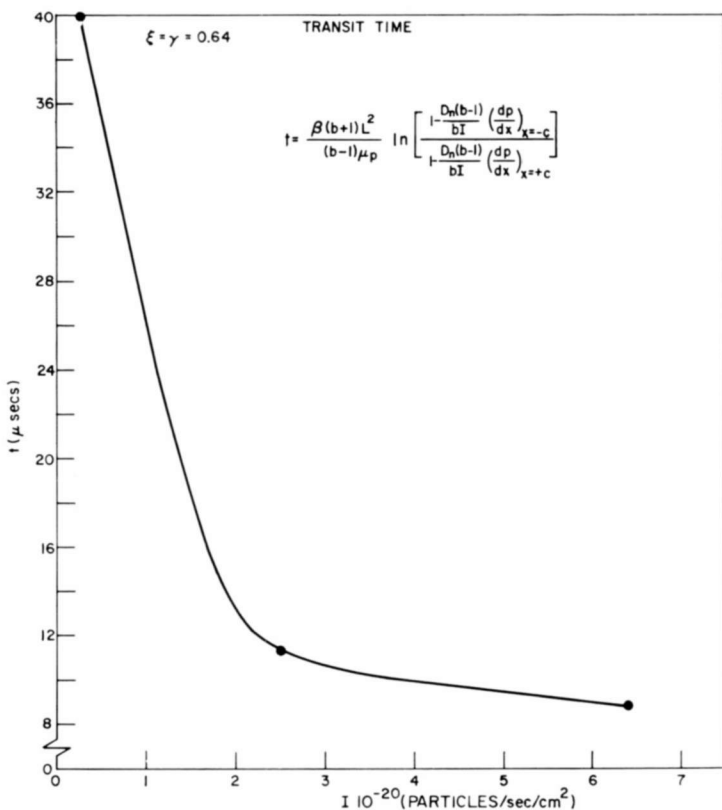


Fig. 13—Plot of the transit time across the i region versus  $I$ . For particle densities in excess of  $2 \times 10^{20}$ , the transit time is about 10  $\mu$ sec.

Equation (11) shows that if  $\gamma = 1$ ,

$$\exp\{2\beta V_{-c}\} = (1 - \gamma) \frac{I}{I_n} \left( \frac{n_N}{p_N} \right) = 0.$$

However,  $V_{-c}$  by definition is the forward bias across the p-i (p<sup>+</sup>-N) junction and of necessity is positive. But the only way  $\exp\{2\beta V_{-c}\}$  can vanish is if  $V_{-c}$  is large and negative—in other words if the

p-i (p<sup>+</sup>-N) junction is reverse biased, which is a contradiction.

Hence,  $\gamma$  cannot be unity. Similarly  $\xi$  cannot be unity.

## APPENDIX II

The integral

$$K = \int_x^c \frac{dx}{\left[ p_{-c} \sinh \left[ \frac{c-x}{L} \right] + p_c \sinh \left[ \frac{c+x}{L} \right] \right]}$$

is evaluated as follows. Let  $u = \frac{1}{2} \left[ 1 + \frac{x}{c} \right]$ . Then

$$K = L \int_{\frac{1}{2} \left[ 1 + \frac{x}{c} \right]}^1 \frac{\lambda du}{\left[ p_{-c} \sinh [\lambda(1-u)] + p_c \sinh \lambda u \right]} \quad (70)$$

$$K = \frac{2L}{\left[ 2p_c p_{-c} \cosh \lambda - p_c^2 - p_{-c}^2 \right]^{1/2}} \int_{\frac{\lambda}{2} \left( 1 + \frac{x}{c} \right)}^{\exp(\lambda)} \frac{dA\zeta}{\exp \left\{ \frac{\lambda}{2} \left( 1 + \frac{x}{c} \right) \right\}} \quad (71)$$

where

$$\zeta = e^{\lambda u} \quad \text{and} \quad A^2 = \frac{p_c - p_{-c} e^{-\lambda}}{p_{-c} e^{\lambda} - p_c}$$

For  $A^2 > 0$ ,

$$K = \frac{2L \left[ \arctan (A \exp \{\lambda\}) - \arctan \left( A \exp \left\{ \frac{\lambda}{2} \left( 1 + \frac{x}{c} \right) \right\} \right) \right]}{\left[ 2p_c p_{-c} \cosh \lambda - p_c^2 - p_{-c}^2 \right]^{1/2}} \quad (72)$$

From Equations (12) and (13)

$$p_c/p_{-c} = \left[ \frac{1-\xi}{1-\gamma} \right]^{1/2} \left[ \frac{I_{ns}}{I_{rs}} \right]^{1/2} = R \left[ \frac{1-\xi}{1-\gamma} \right]^{1/2} \quad (73)$$

where  $R^2 = I_{ns}/I_{ps}$ . Substituting  $(p_c/p_{-c})$  into the expression for  $A^2$  yields

$$A^2 = \frac{(p_c/p_{-c}) - e^{-\lambda}}{e^\lambda - (p_c/p_{-c})} = \frac{R\sqrt{1-\xi} - e^{-\lambda}\sqrt{1-\gamma}}{e^\lambda\sqrt{1-\gamma} - R\sqrt{1-\xi}}, \quad (74)$$

$$= \frac{R^2(1-\xi) - (1-\gamma) + 2R\sqrt{(1-\xi)(1-\gamma)} \sinh \lambda}{e^{2\lambda}(1-\gamma) - R^2(1-\xi)}. \quad (75)$$

Hence,  $A$  depends on the injection parameters  $\zeta$  and  $\gamma$  along with  $R$ , which is a saturation current ratio. These three parameters are junction parameters, while  $\lambda = 2c/L$  is a parameter characteristic of the intrinsic region.

If  $\zeta = \gamma$ , considerable simplification takes place;

$$A^2 = \frac{R^2 - 1 + 2R(1-\gamma) \sin h\lambda}{e^{2\lambda} - R^2}. \quad (76)$$

The evaluation of the surd in the denominator of  $K$  also requires the use of Equations (12) and (13);

$$[2p_cp_{-c} \cosh \lambda - p_c^2 - p_{-c}^2]^{1/2} = n_i \left[ \frac{I}{I_{ns}} \right]^{1/2} [1-\gamma]^{1/2}$$

$$\left[ 2 \left[ \frac{1-\xi}{1-\gamma} \right]^{1/2} R \cosh \lambda - \frac{(1-\xi)}{(1-\gamma)} R^2 - 1 \right]^{1/2}$$

which gives

$$K = \frac{2L}{n_i(1-\gamma)^{1/2}} \left[ \frac{I_{ns}}{I} \right]^{1/2}$$

$$\frac{\left\{ \arctan(A \exp\{\lambda\}) - \arctan \left( A \exp \left\{ \frac{\lambda}{2} \left( 1 + \frac{x}{c} \right) \right\} \right) \right\}}{\left[ 2 \left[ \frac{1-\xi}{1-\gamma} \right]^{1/2} R \cosh \lambda - \frac{(1-\xi)}{(1-\gamma)} R^2 - 1 \right]^{1/2}}$$

## APPENDIX III

The Green's function, Equation (45), which is a solution to Equation (43) subject to the boundary conditions given by Equation (44) is constructed according to Ince<sup>15</sup> as follows:

$$G(x, \zeta) = A\psi_1(x) + B\psi_2(x) \mp \frac{[\psi_1(x)\psi_2(\zeta) - \psi_2(x)\psi_1(\zeta)]}{2p_0(\zeta)[\psi_1(\zeta)\psi_2'(\zeta) - \psi_2(\zeta)\psi_1'(\zeta)]}, \quad (77)$$

where  $\psi_1(x)$  and  $\psi_2(x)$  are linearly independent solutions of the homogeneous Equation (43).  $p_0(x) = p_0(\zeta) = 1$  is the coefficient of the second derivative<sup>12</sup> in Equation (43) and  $A$  and  $B$  are determined by the boundary conditions of Equation (44). The upper sign (minus) is used for  $x < \zeta$  while the lower sign (plus) for  $x > \zeta$ .

The linearly independent solutions of the homogeneous Equation (43) are the p-i-n diode solutions obtained earlier:

$$\begin{aligned} \psi_1(x) &= \sinh \left[ \frac{c-x}{L} \right], \\ \psi_2(x) &= \sinh \left[ \frac{c+x}{L} \right]. \end{aligned} \quad (78)$$

The Wronskian that occurs in the denominator of the third term in Equation (77) is

$$W = \psi_1(\zeta)\psi_2'(\zeta) - \psi_2(\zeta)\psi_1'(\zeta) = \frac{1}{L} \sinh \lambda$$

when  $\psi_1(x)$  and  $\psi_2(x)$  are given by Equation (78). The Green's function becomes

$$\begin{aligned} G(x, \zeta) &= A \sinh \left[ \frac{c-x}{L} \right] + B \sinh \left[ \frac{c+x}{L} \right] \\ &= \frac{L}{2 \sinh \lambda} \left[ \sinh \left[ \frac{c-x}{L} \right] \sinh \left[ \frac{c+\zeta}{L} \right] \right. \\ &\quad \left. - \sinh \left[ \frac{c+x}{L} \right] \sinh \left[ \frac{c-\zeta}{L} \right] \right]. \end{aligned} \quad (79)$$

Evaluation of  $A$  and  $B$  by utilizing the boundary conditions of Equation (44) leads to the Green's function given by Equation (45).

<sup>15</sup> E. L. Ince, *Ordinary Differential Equations*, p. 257, Dover Publications, New York, N. Y., 1944.

## APPENDIX IV

The extended-gate solution is obtained in the following manner. Suppose the gate generates  $f(x)$  holes per length in the interval  $a \leq x \leq b$ . Then the delta function in Equations (37) and (39) is replaced by  $f(x)$ ;

$$\phi(x) = \frac{1}{L^2} \int_{-c}^{+c} G(x, \zeta) f(\zeta) d\zeta. \quad (80)$$

The Green's function  $G(x, \zeta)$  is given by Equation (45); thus once the spatial variation of the source intensity  $f(x)$  is specified Equation (80) can be evaluated. An interesting example is the case where the gate is of width  $2\epsilon$  centered about  $x=l$ , i.e.,  $b=l+\epsilon$ , and  $a=l-\epsilon$ . If the source is of constant intensity  $P_G$  over the interval  $l-\epsilon$  to  $l+\epsilon$ , the intensity  $f(x)$  is given by

$$f(x) = \overline{P}_G [S(x-l+\epsilon) - S(x-l-\epsilon)], \quad (81)$$

where  $S(x-a)$  is the Heaviside unit step function;

$$\begin{aligned} S(x-a) &= 0, & x < a, \\ S(x-a) &= 1, & x > a. \end{aligned} \quad (82)$$

Substituting Equation (81) into (80) yields

$$\phi(x) = \frac{\overline{P}_G}{L^2} \int_{l-\epsilon}^{l+\epsilon} G(x, \zeta) d\zeta = \frac{\overline{P}_G}{L^2} \int_{l-\epsilon}^x G(x < \zeta, \zeta) d\zeta + \frac{\overline{P}_G}{L^2} \int_x^{l+\epsilon} G(x > \zeta, \zeta) d\zeta. \quad (83)$$

Upon substituting Equation (45) into (83) and integrating,

$$\begin{aligned} \phi(x) &= \frac{\overline{P}_G}{\sinh \lambda} \left[ \sinh \left[ \frac{c+x}{L} \right] \cosh \left[ \frac{c+l+\epsilon}{L} \right] \right. \\ &\quad \left. + \sinh \left[ \frac{c-x}{L} \right] \cosh \left[ \frac{c-l+\epsilon}{L} \right] \right] - \overline{P}_G. \end{aligned} \quad (84)$$

The closed-form solution for an extended gate with constant source intensity over its extension is given by

$$p(x) = \bar{P}(x) + \phi(x), \quad (85)$$

where  $\bar{P}(x)$  is given by Equation (19) and  $\phi(x)$  by Equation (84). This procedure can be readily extended to cases where  $f(x)$  is a variable function over the extension of the source. In particular, suppose

$$f(x) = \bar{P}_G \sin \left[ \frac{\pi(x-l+\epsilon)}{2\epsilon} \right] [S(x-l+\epsilon) - S(x-l-\epsilon)], \quad (86)$$

where the functions  $S(x)$  are the Heaviside unit step-functions defined by Equation (82).

Substituting for  $f(\zeta)$  in Equation (80) yields

$$\begin{aligned} \phi(x) &= \frac{\bar{P}_G}{L^2} \int_{l-\epsilon}^{l+\epsilon} G(x, \zeta) \sin \left[ \frac{\pi(\zeta-l+\epsilon)}{2\epsilon} \right] d\zeta \\ &= \frac{\bar{P}_G}{L^2} \int_{l-\epsilon}^x G(x < \zeta, \zeta) \sin \left[ \frac{\pi(\zeta-l+\epsilon)}{2\epsilon} \right] d\zeta \\ &\quad + \frac{\bar{P}_G}{L^2} \int_x^{l+\epsilon} G(x > \zeta, \zeta) \sin \left[ \frac{\pi(\zeta-l+\epsilon)}{2\epsilon} \right] d\zeta. \end{aligned} \quad (87)$$

Substituting for the Green's function from Equation (45) yields

$$\begin{aligned} \phi(x) &= -\frac{\bar{P}_G \sinh \left[ \frac{c+x}{L} \right]}{L \sinh \lambda} \int_{l-\epsilon}^x \sinh \left[ \frac{c-\zeta}{L} \right] \sin \left[ \frac{\pi(\zeta-l+\epsilon)}{2\epsilon} \right] d\zeta \\ &\quad + \frac{\bar{P}_G \sinh \left[ \frac{c-x}{L} \right]}{L \sinh \lambda} \int_x^{l+\epsilon} \sinh \left[ \frac{c-\zeta}{L} \right] \sin \left[ \frac{\pi(\zeta-l+\epsilon)}{2\epsilon} \right] d\zeta. \end{aligned} \quad (88)$$

These integrals are elementary and can be evaluated, yielding

$$\begin{aligned} \phi(x) = & \frac{\bar{P}_G \left( \frac{\pi L}{2\epsilon} \right) \operatorname{csch} \lambda}{\left[ 1 + \frac{\pi^2 L^2}{4\epsilon^2} \right]} \left\{ \sinh \left[ \frac{c-l+\epsilon}{L} \right] \sinh \left[ \frac{c+x}{L} \right] \right. \\ & \left. + \sinh \left[ \frac{c+l+\epsilon}{L} \right] \sinh \left[ \frac{c-x}{L} \right] \right\} \\ & - \frac{\bar{P}_G \sin \left[ \frac{\pi(x-l+\epsilon)}{2\epsilon} \right]}{\left[ 1 + \frac{\pi^2 L^2}{4\epsilon^2} \right]}. \end{aligned} \quad (89)$$

The closed-form solution for an extended gate with a source intensity that varies as a half-period sinusoid, Equation (86), is given by

$$p(x) = \bar{P}(x) + \phi(x), \quad (90)$$

where  $P(x)$  is given by Equation (19) and  $\phi(x)$  by Equation (89).

#### APPENDIX V

The Shockley and Prim<sup>14</sup> definition of transit time is

$$t = \int_{-c}^c \frac{dx}{\mu_p E}.$$

When

$$E = \frac{bI}{\beta D_n (b+1) p(x)} - \left[ \frac{b-1}{b+1} \right] \frac{1}{\beta p(x)} \frac{dp(x)}{dx}, \quad (91)$$

$$t = \beta D_n \frac{(b+1)}{\mu_p} \int_{-c}^c \frac{p(x) dx}{bI - D_n (b-1) \frac{dp}{dx}}. \quad (92)$$

For a p-i-n diode, or a triode structure with the gate cut off, Equation (16) holds; hence

$$p(x) = L^2 \frac{d^2 p}{dx^2}. \quad (93)$$

Substituting for  $p(x)$  in Equation (92)

$$\begin{aligned} t &= \frac{\beta D_n (b+1) L^2}{\mu_p} \int_{-c}^c \frac{\frac{d^2 p(x)}{dx^2} dx}{bI - D_n (b-1) \frac{dp}{dx}} \\ &= \frac{\beta D_n (b+1) L^2}{\mu_p} \int_{-c}^c \frac{d\left(\frac{dp}{dx}\right)}{bI - D_n (b-1) \frac{dp}{dx}} \\ &= \frac{\beta (b+1) L^2}{(b-1) \mu_p} \int_{-c}^c \frac{du}{1-u}, \end{aligned} \quad (94)$$

where

$$u = \frac{D_n (b-1)}{bI} \frac{dp}{dx}. \quad (95)$$

Integrating Equation (94) and substituting for  $u$  in the result yields Equation (69).

#### APPENDIX VI

The saturation current for a p-n junction is given by Smith.<sup>16</sup> Let  $I_s(\pm c)$  be the saturation current for p<sup>+</sup>-N junction ( $-c$ ) and the N<sup>+</sup>-N junction ( $+c$ ). The conductivities  $\sigma_{N^+}$ ,  $\sigma_i$ ,  $\sigma_{p^+}$  are the conductivities of N<sup>+</sup>, N and p<sup>+</sup> regions, respectively.  $L_{hi}$ ,  $L_{ei}$ ,  $L_{ep^+}$ , and  $L_{hN^+}$  are, respectively, diffusion lengths of holes in the intrinsic (N)<sup>+</sup> region, of electrons in the intrinsic (N) region, of electrons in the p<sup>+</sup> region of the  $\pm$ N junction, holes in the N<sup>+</sup> region of the N<sup>+</sup>-N junction. According to Smith,

<sup>16</sup> R. A. Smith, *Semiconductors*, Cambridge University Press, 1959; p. 270.

$$I_s(-c) = \frac{b\sigma_i^2}{(1+b)^2} \left[ \frac{1}{\sigma_i L_{hi}} + \frac{1}{\sigma_p + L_{ep}^+} \right]$$

$$I_s(+c) = \frac{b\sigma_i^2}{(1+b)^2} \left[ \frac{1}{\sigma_N + L_{hN}^+} + \frac{1}{\sigma_i L_{ei}} \right].$$

Thus,

$$I_{ns}(-c) = \frac{b\sigma_i^2}{(1+b)^2} \frac{1}{\sigma_p + L_{ep}^+}$$

is the saturation current due to electrons in the p<sup>+</sup>-N junction.

$$I_{ps}(+c) = \frac{b\sigma_i^2}{(1+b)^2} \frac{1}{\sigma_N + L_{hN}^+}$$

is the saturation current due to holes in the N<sup>+</sup>-N junction.

$$R^2 = \frac{I_{ns}(-c)}{I_{ps}(+c)} = \frac{\sigma_N + L_{hN}^+}{\sigma_p + L_{ep}^+}$$

if  $L_{hN}^+ \sim L_{ep}^+$  is assumed.

$$R^2 = \frac{\sigma_N^+}{\sigma_p^+}.$$

The following data has been procured from G. Cody of RCA Laboratories for carrier contrations of 10<sup>18</sup>:

$$p_N^+ = 6 \times 10^{-3} \text{ ohm-cm}, \quad \sigma_N^+ = 167 \text{ (ohm-cm)}^{-1}$$

$$p_p^+ = 1.1 \times 10^{-2} \text{ ohm-cm}, \quad \sigma_p^+ = 91 \text{ (ohm-cm)}^{-1}$$

hence  $R^2 = 167/91 = 1.835$ , which yields  $R = 1.35$ .

# STABLE DIVALENT RARE EARTHS IN ALKALINE EARTH HALIDES BY SOLID-STATE ELECTROLYSIS\*

BY

FRANCIS K. FONG

*Summary*—An electrolytic process for the reduction of rare-earth ions in alkaline-earth halides is described. Trivalent dysprosium and thulium in calcium fluoride have been successfully reduced to the divalent state. These reduced samples are stable with respect to optical bleaching, and thermoluminescence accompanying the thermal reoxidation of the rare-earth ions has not been observed.

THE RARE-EARTH elements are characterized by the uniform stable trivalent oxidation state, which is expected of members of Periodic Group IIIa. The existence of the well-characterized divalent samarium, europium, and ytterbium ions has been attributed to the tendency of the elements to attain or approach the electronic configurations of the ions  $\text{La}^{2+}(4f^05s^25p^6)$ ,  $\text{Gd}^{2+}(4f^75s^25p^6)$  and  $\text{Lu}^{2+}(4f^{14}5s^25p^6)$ , where the  $4f$  orbitals are empty, half-filled, and completely filled, respectively.<sup>1</sup> Recently, divalent rare earths have been obtained<sup>2-4</sup> in the alkaline-earth fluorides by subjecting the trivalent rare-earth-doped crystals to ionizing radiation such as x-rays<sup>2</sup> and gamma-rays.<sup>3,4</sup> This radiation-induced reduction process, however, is rather inefficient in that only a small fraction of the trivalent ions are converted to the divalent state.<sup>4</sup> In addition, the radiation-induced divalent rare-earth ions are metastable in nature, being readily bleached (or reoxidized) by heat and light.<sup>4</sup> In the present publication, we wish

\* The research reported in this paper was sponsored by Air Force Materials Laboratory Research and Technology, Air Force Systems Command, Wright-Patterson Air Force Base, Ohio, under Contract Number AF33 (657) 11221.

<sup>1</sup> F. D. S. Butement, "Absorption and Fluorescence Spectra of Bivalent Samarium, Europium, and Ytterbium," *Trans. Faraday Soc.*, Vol. 44, Pt. 9, p. 617, Sept. 1948.

<sup>2</sup> W. Hayes and J. S. Twidell, "Paramagnetic Resonance of X-Irradiated  $\text{CaF}_2:\text{Tm}$  and of  $\text{CaF}_2:\text{Yb}$ ," *Jour. Chem. Phys.*, Vol. 35, No. 4, p. 1521, Oct. 1961.

<sup>3</sup> D. S. McClure and Z. J. Kiss, "Survey of the Spectra of the Divalent Rare-Earth Ions in Cubic Crystals," *Jour. Chem. Phys.*, Vol. 39, No. 12, p. 3251, Dec. 1963.

<sup>4</sup> F. K. Fong, "Gamma-Induced Divalent Dysprosium in Calcium Fluoride," *Jour. Chem. Phys.*, Vol. 41, No. 1, July 1964.

to report the first results of a solid-state electrolytic process that has been successfully employed for the production of stable divalent rare-earth ions.

The experimental arrangement for the electrolytic reduction of rare-earth ions in alkaline-earth halides is shown in Figure 1. A section

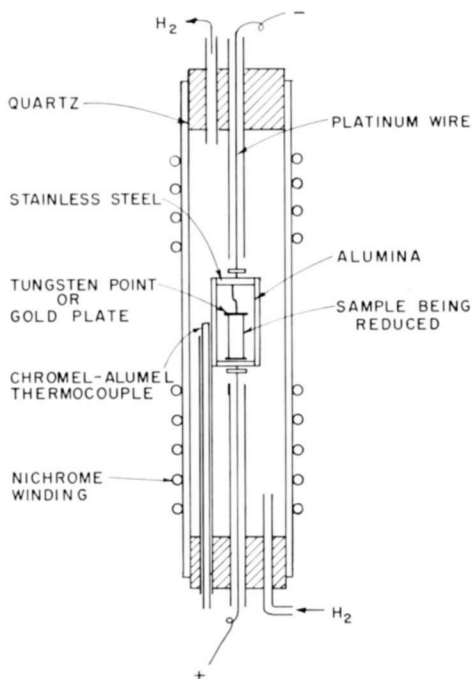


Fig. 1—Schematic diagram of the apparatus for the electrolytic reduction process.

of the quartz container was left free of furnace winding so as to allow observation of the sample during the reduction. A 400-volt d-c power supply was employed to provide voltage in the range 150-300 volts for the electrolytic process. The reductions were carried out at temperatures above 300° and up to 700°C. A gentle flow of dry hydrogen was employed to maximize the uniformity of temperature in the reaction cell. Either a tungsten point or a gold plate may be used as the cathode in the electrolytic reduction. Reduction of the rare-earth ions occurred readily at temperatures above 600°C, the reduced sample being uniformly tinted by the characteristic color of the divalent rare-earth ions (i.e., blue for dysprosium and green for thulium). A current as high

as 2 milliamperes was detected through the system at  $480^\circ$  with 200 volts. Occasionally, the current achieved was so high that the sample shattered. To avoid this, a current-limiting resistor (10,000-100,000 ohms) was connected in series with the electrolytic cell. The reduced samples were not quenched.

The absorption spectrum of an electrolytically reduced  $\text{CaF}_2$  sample containing  $10^{-1}$  mole percent dysprosium is compared in Figure 2 with that of another sample containing the same concentration of dysprosium, but gamma-irradiated (at  $10^7$  rad) to contain the highest attainable<sup>4</sup> concentration of gamma-induced divalent dysprosium ions. When appreciable concentrations of trivalent rare-earth ions are doped in calcium fluoride, most of the trivalent ions are compensated by interstitial fluoride ions, the presence of which has recently been established.<sup>5</sup> A certain fraction of the  $3+$  ions, however, may be incorporated into the  $\text{CaF}_2$  lattice without any local charge compensation due, in part at least, to the imperfections of crystal growth and the nonideal nature of the solution. Such locally uncompensated  $3+$  ions possess an effective charge of  $1+$  each, and constitute efficient electron traps. Gamma-irradiation of such a crystal results in the photochemical reduction of these locally uncompensated ions to the divalent state.<sup>4</sup> The fact that the concentration of  $\text{Dy}^{2+}$  ions attainable by electrolytic reduction is severalfold higher than that attainable by gamma irradiation (Figure 2) suggests that locally compensated  $3+$  ions as well as the locally uncompensated ones are reducible by the electrolytic technique. Evidently, application of the electrical field causes migration of the interstitial fluoride ions towards the anode, leaving the  $3+$  ions essentially uncompensated and therefore reducible. This mechanism is not unlike that postulated<sup>6</sup> for the electrolytic coloration of alkali halide crystals.

Since the charge-compensating interstitial fluoride ions migrate toward the anode where they are oxidized to the neutral state and presumably escape from the crystal lattice, no hole centers should be present in the reduced sample. This is evidenced by the finding that these samples are optically stable as contrasted with the metastable gamma-reduced samples, which are readily bleached by light absorbed at the sharp band peaking at  $458 \text{ m}\mu$ .<sup>4</sup> Also, thermoluminescence accompanying the thermal excitation of holes into the valence band,<sup>4</sup> with

---

<sup>5</sup> J. Short and R. Roy, "Confirmation of Defect Character in Calcium Fluoride-Yttrium Fluoride Crystalline Solutions," *Jour. Phys. Chem.*, Vol. 67, p. 1860, Sept. 1963.

<sup>6</sup> J. H. Schulman and W. D. Compton, *Color Centers in Solids*, p. 65, Pergamon Press, McMillan Co., New York, 1962.

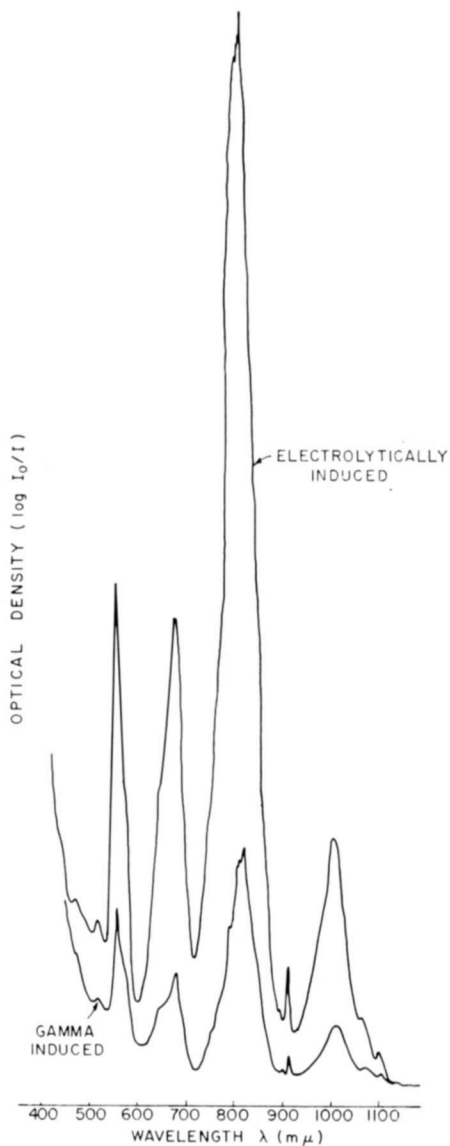


Fig. 2—The 4f-5d absorption spectra of  $Dy^{2+}$  ions induced in  $CaF_2$  containing  $10^{-1}$  mole percent dysprosium by the electrolytic process and by gamma irradiation. Both samples were  $10^{-1}$  inch thick.

subsequent reoxidation of the divalent rare-earth ions, has not been observed. The thermal and optical stabilities of these samples are of paramount importance in the employment of these materials as lasers. In this respect, the electrolytic process is evidently of a greater value than the gamma-irradiation technique as a procedure for producing these laser materials.

In the case of the gamma-irradiation process, the remarkable similarities of the redox reactions with the formation by irradiation with ionizing particles, and the optical and thermal bleachings of  $F$  and  $V_1$  centers in alkali halides are manifested by the similarities of the models and mechanisms proposed for these processes.<sup>4</sup> On a broader basis, the phenomena associated with the redox reaction of rare-earth ions in crystalline solids resemble in a remarkable manner those associated with the formation and bleaching of the color centers in alkali halides or alkaline earth halides.<sup>7</sup> Indeed, all the known techniques for the coloration of the undoped crystals have been found to be applicable to the reduction of trivalent rare-earth ions in the doped crystals, and the science of the solid-state reduction of rare-earth ions may well be considered as a special chapter in the study of color centers.

#### ACKNOWLEDGMENT

The author wishes to acknowledge the helpful discussions with E. Sabisky, G. Goldsmith and H. Pinch. He is especially grateful to S. Larach and P. N. Yocom for their interest and encouragement throughout the course of the work. He is indebted to J. Gannon for the construction of the apparatus shown in Figure 1, and to H. Temple for the growth of crystals.

---

<sup>7</sup> F. K. Fong and P. N. Yocom, "Crystal Growth and Color Centers of Alkaline Earth Halides," *Jour. Chem. Phys.* (to be published).

# WIDE-TEMPERATURE-RANGE FERRITE CORES FOR COMPUTER MEMORIES

BY

H. P. LEMAIRE, H. LESSOFF, AND E. FORTIN

RCA Electronic Components and Devices,  
Needham, Mass.

*Summary*—The operating temperature range of a ferrite memory is determined primarily by the temperature coefficients of the break current and the output of the cores. The break-current and output characteristics of the new lithium-ferrite cores are relatively independent of temperature, and the use of these types of cores will substantially increase the operating range of memory devices over that obtainable with conventional types. Experimental data are given to show, as a function of temperature, the typical response characteristics of practical wide-temperature-range cores of two different sizes; one has an outside diameter of 50 mils and an inside diameter of 30 mils, the other an outside diameter of 30 mils and an inside diameter of 18 mils. The techniques used to design a core for operation in a specific temperature range are described. The performance characteristics of a memory plane that consists of a square array of 4096 wide-temperature-range cores are summarized.

## INTRODUCTION

THE SWITCHING properties of the ferrite cores are a major consideration in the design of a coincident-current memory. The effect of temperature on these properties is of prime importance in determining the operating range of the memory and of the computer. The operating characteristics of the cores that have been in general use change rapidly with small variations in temperature. As a result, computer memory devices have been generally restricted to operation over a relatively narrow temperature range (15° to 45°C). Core limitations have frequently necessitated the use of current compensation in driver circuits, or of expensive temperature controls involving thermostatic heating or air conditioning.

Recently, cores with switching properties that are relatively insensitive to temperature variations have become available. Memories constructed from these cores are capable of operating over temperature ranges greater than 100 centigrade degrees without the need for current compensation in the driver circuits.

The improvement in core performance has been brought about by the use of materials that have high Curie temperatures and have

square-loop properties that are relatively insensitive to temperature variations. Several materials are available. Lithium ferrite<sup>1</sup> and substituted lithium ferrites have Curie temperatures generally above 600°C as compared with conventional magnesium-manganese and manganese-copper systems that have Curie temperatures between 200° and 300°C. Weisz<sup>2</sup> achieved comparatively good temperature stability of square-loop behavior using nickel ferrite ( $T_c = 585^\circ\text{C}$ ). Baltzer,<sup>3</sup> Vinal,<sup>4</sup> and Corter<sup>5</sup> prepared substituted lithium ferrites with excellent square-loop properties.

The present paper describes the specific operating characteristics of cores prepared from substituted lithium ferrite compositions. Also discussed are the basic considerations in the design of coincident-current memories using these cores and design information that relates core properties to memory-plane operation.

#### WIDE-TEMPERATURE-RANGE CORES VERSUS CONVENTIONAL CORES

The temperature range of operation of a core in a coincident-current memory is basically determined by the temperature coefficients of the break current ( $I_b$ ) and of the core output ( $nV_1$ ).<sup>\*</sup> Figure 1 illustrates the temperature dependence of the break current and the output for two types of cores. One type, designated A, is a conventional core; the other, designated B, is a core capable of operation over a wide temperature range in a coincident-current context. To simplify the comparison, all operating conditions were idealized, and current margins, plane noise, and limit considerations were ignored.

In the hypothetical case chosen, the two cores, A and B, have identical outputs and break-current levels at 25°C. Core A, made of conventional ferrite, has a greater output and break-current coefficient than core B. It is this fact that causes the operation of core A to be limited to a narrower temperature range than that of core B. As the temperature increases, the break current of core A drops rapidly—at 45°C it has decreased to 50% of the full drive current ( $I_m$ ) and the

<sup>1</sup> J. Smit and H. P. J. Wijn, *Ferrites*, p. 157, John Wiley and Sons, New York, N. Y., 1959.

<sup>2</sup> R. S. Weisz, "Square-Loop Ferrite with Temperature-Independent Properties and Improved Disturb Ratio," *Jour. Appl. Phys.*, Vol. 32, p. 1152, June 1961.

<sup>3</sup> P. K. Baltzer, "Sintered Spinel Magnetic Cores," U.S. Patent 3,034,987, May 15, 1962.

<sup>4</sup> F. E. Vinal and D. L. Brown, "Lithium-Nickel Ferrites," U.S. Patent 3,038,860, June 12, 1962.

<sup>5</sup> E. W. Gorter and C. J. Esveldt, "Magnetic Cores," Dutch Patent 82,272, August 15, 1962.

<sup>\*</sup> Refer to Appendix I for definitions of all terms describing pulse and output characteristics.

core cannot operate in a coincident-current memory above this temperature. By contrast, the break current for core B does not decrease to the 50%  $I_m$  limit until the temperature is 75°C.

The lower temperature limit is defined, somewhat arbitrarily in this case, as that temperature at which the signal-to-noise ratio falls to a value of 3 to 1. It is evident from Figure 1 that this limit is much higher for core A than for core B. The bars at the bottom of the figure

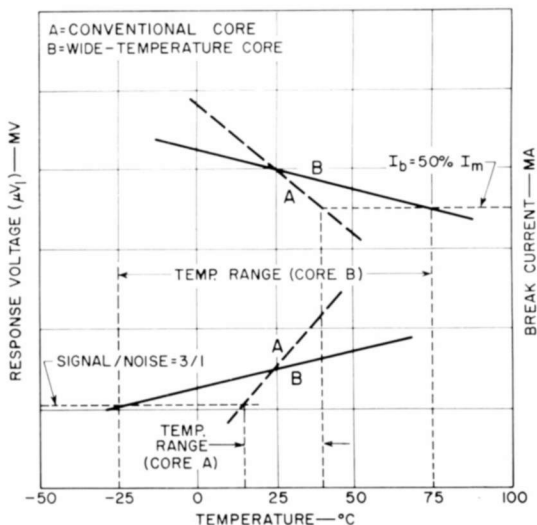


Fig. 1—Pulse properties as a function of temperature for a conventional memory core and a wide-temperature-range memory core.

are projected from the plot above, and simply represent the temperature range of operation for each of the core types.

It should be noted that the case described is a hypothetical one, idealized in all respects for the sake of simplicity. When an estimate of the temperature-range potential of a core is made for specific applications, several other factors affect the outcome and must be taken into account.

#### WIDE-TEMPERATURE-RANGE CORES

Table I summarizes the pulse properties of seven new wide-temperature-range cores. These cores, which cover a wide range of drive currents and switching speeds, are arranged in the table in order of decreasing drive currents or increasing switching times. The drive currents vary between 300 and 800 milliamperes, and the switching

Table I—Pulse Properties of Wide-Temperature-Range Memory Cores

Drive Parameters						Operating Characteristics					
Core Type	Size OD/ID (mils)	$I_m$ (ma)	$I_{pw}$ (ma)	$t_r$ ( $\mu$ sec)	$t_d$ ( $\mu$ sec)		$uV_1$ (mv)	$dV_z$ (ma)	$t_p$ ( $\mu$ sec)	$t_s$ ( $\mu$ sec)	$I_b$ (ma)
233M1	50/30	800	500	0.5	4.0	typical	64	6	.69	1.15	540
						limits	55	8	.75	1.25	500
264M1	50/30	580	350	0.4	3.0	typical	55	8	.67	1.25	355
						limits	45	10	.72	1.35	350
0140M5	50/30	450	270	0.4	2.0	typical	48	6	.78	1.48	285
						limits	42	8	.83	1.50	270
0146M5	30/18	800	480	0.1	0.5	typical	65	7	.20	.45	490
						limits	55	9	.24	.50	480
266M1	30/18	600	360	0.3	2.0	typical	42	4	.46	.85	360
						limits	35	5	.50	.90	360
0135M5	30/18	380	230	0.4	2.0	typical	26	3	.70	1.2	247
						limits	20	4	.74	1.25	230
0138M5	30/18	310	186	0.4	2.0	typical	22	3	.80	1.48	200
						limits	18	4	.83	1.50	186

speeds range from 0.5 to 1.5 microseconds, corresponding to memory-cycle times of approximately 2.0 to 6.0 microseconds.

Figures 2 and 3 illustrate, in more detail, the pulse properties of one of the cores. Figure 2 relates pulse properties to drive-current variations at a fixed temperature of 25°C; Figure 3 relates pulse properties to temperature changes at a fixed drive current.

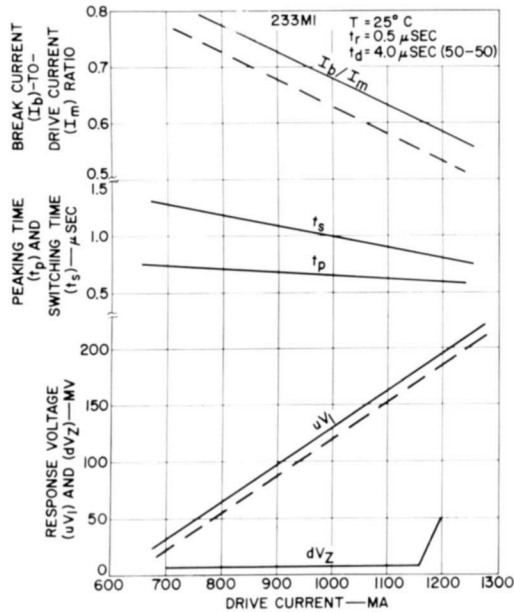


Fig. 2—Characteristics of the 233M1 core as a function of the drive current at a constant temperature (25°C).

#### MEMORY DESIGN—TEMPERATURE RANGE OF OPERATION

The pulse characteristics plotted in Figures 2 and 3 represent typical operation and serve as a guide in evaluating core performance. A core may be chosen to fulfill a variety of specific needs with emphasis on any of several factors including drive current, output level, and memory-cycle time.

The temperature-range capabilities of any specific type of core can be accurately determined from the two graphs for that core and the corresponding limit characteristics given in Table I. The method is simply an extension of the reasoning that was applied in Figure 1 to illustrate the performance of temperature-stable cores in general. If drive-current variations and limit values are considered, worst-case

conditions can be determined, and a reasonably accurate estimate of the temperature range of operation can be made. To demonstrate the technique, a specific example using core type 233M1 will be given.

To determine the *lower temperature limit*, it is necessary to consider the changes in the output voltage of the core in its "undisturbed 1" state ( $uV_1$ ) as both current and temperature are varied. Table I shows that the typical output for a drive of 800 milliamperes is 64 millivolts;

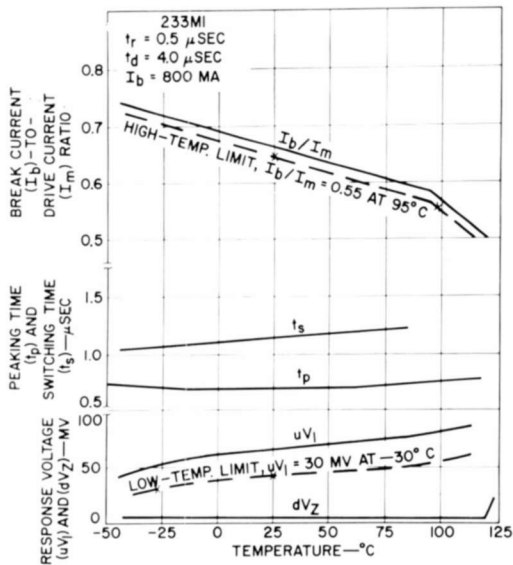


Fig. 3—Characteristics of the 233M1 core as a function of temperature for a constant drive current of 800 milliamperes.

the limit output is actually only 55 millivolts. If  $\pm 5\%$  margins on the drive-current variations are assumed, the worst-case full drive current is 760 milliamperes. The output at this current can be determined from Figure 2. A line is drawn parallel to the  $uV_1$  plot but shifted downward by 9 millivolts to take into account the 9-millivolt differences between typical- and limit-core outputs. This line shows that, at 760 milliamperes, the limit core would have an output of 40 millivolts (at  $25^\circ\text{C}$ ). This information is then applied in Figure 3 to determine the lower temperature limit of operation. A curve is drawn parallel to the existing  $uV_1$  curve but passing through the 40-millivolt point at  $25^\circ\text{C}$ . If the minimum acceptable discrimination is assumed to be 3 to 1, the lower temperature limit is obtained by observing the temperature at

which the output falls below 30 millivolts. In this case, this temperature is approximately  $-30^{\circ}\text{C}$ .

The *upper temperature limit* is obtained in similar fashion from the  $I_b/I_m$  curve. If, once again, maximum drive-current variations of  $\pm 5\%$  are assumed and the inhibit-current variations are ignored, the worst-case disturb conditions of a core correspond to a  $I_b/I_m$  ratio of 0.55 (420 to 760 milliamperes). Table I indicates that, at  $25^{\circ}\text{C}$ , the limit of the  $I_b/I_m$  ratio is 500/800, or 0.625.

A line is drawn parallel to the existing  $I_b/I_m$  curve in Figure 2, through the 0.625 point at 800 milliamperes. At 760 milliamperes, the  $I_b/I_m$  ratio is 0.645. A line is then drawn in Figure 3 parallel to the existing  $I_b/I_m$  line, but passing through the 0.645  $I_b/I_m$  point at  $25^{\circ}\text{C}$ . This line shows the temperature at which the  $I_b/I_m$  ratio falls below 0.55. This point occurs at about  $95^{\circ}\text{C}$  which is, therefore, the upper temperature limit of the core. The complete operating range of the core is thus  $-30^{\circ}\text{C}$  to  $+95^{\circ}\text{C}$ . If inhibit-current margins are included in the calculations, the upper temperature limit is reduced because the worst-case  $I_b/I_m$  ratio then becomes somewhat greater than 0.55.

The rate of change of  $uV_1$  and break current with temperature for the other types of cores listed in Table I is less than that for the 233M1 core. Therefore, the temperature range of operation for these other types would be correspondingly greater than that for the 233M1.

#### TEMPERATURE COEFFICIENTS OF OUTPUT AND $I_b/I_m$ RATIO

It has been shown how the rates of change of the  $I_b/I_m$  ratio and output with temperature determine the operating range of a core. Table II summarizes the temperature coefficient of output and  $I_b/I_m$  ratio for the wide-temperature cores described earlier. For the sake of contrast, similar data are included in the table for two cores that are *not* temperature-stable—types 244M1 and 254M1. This tabular information is general, but it provides a rough comparison between core types having the same dimensions and is of value in estimating the relative temperature-range capabilities of a core. The significant difference between the conventional cores and the lithium-ferrite cores is obvious. Even within the temperature-stable family, however, core types differ appreciably in respect to  $uV_1$  or  $I_b/I_m$  coefficient, or both. Some types have unusually stable  $uV_1$  characteristics; others are more stable with respect to  $I_b/I_m$  coefficients. Core types 0140M5, 0146M5, and 0138M5 are outstanding in that both the  $uV_1$  and  $I_b/I_m$  ratio are extremely stable. Such cores have a potential of operating over a temperature range substantially greater than 100 centigrade degrees.

Table II—Temperature Coefficients of Output and  $I_b/I_m$  Ratio

Core Type	Size OD/ID (mils)	Drive Current (ma)	$uV_1$ (mv)	Temperature Coefficient	
				$\frac{uV_1}{(mv/^\circ C)}$	$I_b/I_m$ at 25°C
233M1	50/30	800	64	0.20	$1.2 \times 10^{-3}$
264M1	50/30	580	55	0.34	$0.5 \times 10^{-3}$
0140M5	50/30	450	48	0.08	$0.3 \times 10^{-3}$
0146M5	30/18	800	65	0.08	$0.2 \times 10^{-3}$
266M1	30/18	600	42	0.12	$0.9 \times 10^{-3}$
0135M5	30/18	380	26	0.11	$0.8 \times 10^{-3}$
0138M5	30/18	310	22	0.03	$0.18 \times 10^{-3}$
224M1	50/30	460	60	0.70	$2.0 \times 10^{-3}$
254M1	30/18	440	45	0.75	$3.2 \times 10^{-3}$

## MEMORY-PLANE DATA

Plane or stack operation, rather than individual core performance, is the prime and ultimate concern of the memory-system designer. Table III summarizes the performance of a memory plane that consists of an array (64 by 64) of 4096 of the 233M1 cores at temperatures between  $-50^\circ\text{C}$  and  $+100^\circ\text{C}$ . These data were obtained using drive currents of 400 to 800 milliamperes, a pulse width of 3.0 microseconds, and a rise time of 0.5 microsecond. The information pattern in the plane was the usual worst-case double-checkerboard pattern. The data illustrate, in a clear-cut way, the unusually high degree of stability of the core characteristics in the temperature range examined.

Table III—Plane Data

Characteristics	Temperature						
	-50	-25	0	+25	+50	+75	+100
Max. (0) mv	10	12	12	14	14	14	16
$dV_1$ min. mv	38	44	48	52	52	54	56
$dV_1$ max. mv	56	64	68	72	72	72	76
$T_p(1)$ min. $\mu\text{sec}$	1.00	1.00	.98	.98	.98	.98	.98
$T_p(1)$ max. $\mu\text{sec}$	1.08	1.06	1.04	1.04	1.04	1.04	1.04
$T_s(1)$ min. $\mu\text{sec}$	1.38	1.40	1.44	1.52	1.52	1.52	1.52
$T_s(1)$ max. $\mu\text{sec}$	1.46	1.52	1.58	1.64	1.64	1.66	1.66

## CONCLUSIONS

The wide-temperature-range cores described in this paper offer significant advantages and opportunities to the computer designer. A range of memory-cycle times from 2 to 6 microseconds is possible at full drive currents ranging from 300 to 800 milliamperes. The inherently stable switching characteristics of the core permit operation over temperature ranges greater than 100 centigrade degrees without current compensation in the driver circuits. As a result, costly temperature controls or air-conditioning in stack design are not required. There are obvious cost advantages to be realized here; at the same time reliability is increased.

Another advantage of the temperature-stable core is its high Curie point (above 600°C). It would, thus, appear possible to operate memories at temperatures in the order of 500°C which is beyond, or at least equal to, the existing temperature capabilities of related memory-system gear and devices.

## APPENDIX I—DEFINITIONS

This appendix defines the terms used to describe the pulse and output characteristics of the memory cores. Figure 4 illustrates these terms in relation to the driving-current and output-voltage waveforms.

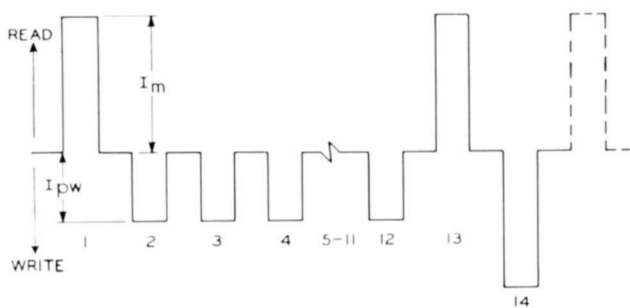
*Full driving current* ( $I_m$ ) is the peak value of the current pulse required to switch a core from its "1" state to its "0" state, or vice versa. A core in the "1" state or "0" state that has been switched by a full-driving-current pulse and has not subsequently been subjected to other pulses is said to be in the "undisturbed 1" or "undisturbed 0" state.

*Partial-write current* ( $I_{pw}$ ) as used in this paper is any value of driving current which disturbs the magnetization of a core in the "0" state, but does not switch the core to the "1" state. A core which has been subjected to one or more partial-write-current pulses is said to be in the "disturbed 0" state.

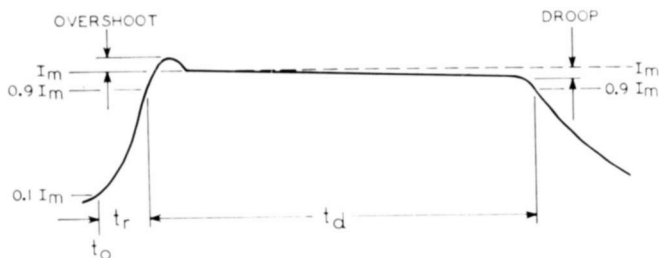
*Pulse rise time* ( $t_r$ ) is the time interval between the instant the driving current rises to 10% of its peak value and the instant it rises to 90% of its peak value.

*Pulse duration* ( $t_d$ ) is the time interval between the instant the driving current rises to 90% of its peak value and the instant it falls to 90% of its peak value.

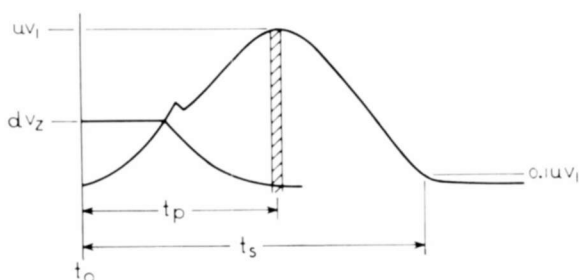
*"Undisturbed 1" response voltage* ( $uV_1$ ) is the peak value of the output voltage produced when a core that is in its "undisturbed 1" state is subjected to a "READ" current pulse having a peak value  $I_m$ .



(a) Driving-current pulse sequence used to test performance characteristics.



(b) Waveform of driving-current pulses.



(c) Approximate waveforms of "undisturbed 1" and "disturbed 0" response voltages.

Fig. 4—Drive-current and output-voltage waveforms in the coincident-current type of memory core.

"Disturbed 0" response voltage ( $dV_z$ ) is the peak value of the output voltage produced when a core which is in its "disturbed 0" state is subjected to a "READ" current pulse having a peak value of  $I_m$ .

Switching time ( $t_s$ ) is the time interval between the instant the driving current rises to 10% of its peak value and the instant the "undisturbed 1" response voltage ( $uV_1$ ) decays to 10% of its peak value.

Peaking time ( $t_p$ ) is the time interval between the instant the driving current rises to 10% of its peak value and the instant the "undisturbed 1" response voltage reaches its peak value.

Break current ( $I_b$ ), also called "threshold current," is the maximum partial-write current ( $I_{pw}$ ) at a given full-driving current ( $I_m$ ) which a core in the "0" state will tolerate without any substantial increase in the amplitude of the "disturbed 0" response voltage ( $dV_z$ ).

## CORRECTION

In the paper entitled "Introductory Statistics and Sampling Concepts Applied to Radar Evaluation," by R. J. D'Ortenzio, which appears in the March 1964 issue, there is a transposition of subscripts in Equations (28)-(30), page 125. The equations should have been written:

$$\sum r_i t_i^2 = A_2 \sum t_i^4 + A_1 \sum t_i^3 + A_0 \sum t_i^2, \quad (28)$$

$$\sum r_i t_i = A_2 \sum t_i^3 + A_1 \sum t_i^2 + A_0 \sum t_i, \quad (29)$$

$$\sum r_i = A_2 \sum t_i^2 + A_1 \sum t_i + A_0 n, \quad (30)$$

# RCA Technical Papers†

First Quarter, 1964

Any request for copies of papers listed herein should be addressed to the publication to which credited.

"Anomalous Band Gap in Superconducting Nb <sub>3</sub> Sn," Y. Goldstein, <i>Rev. Mod. Phys.</i> , Part 1 (January) .....	1964
"Construction of a Promethium-147 Atomic Battery," H. Flicker, J. J. Loferski, and Coauthor, <i>Trans. IEEE PTGED</i> (January) .....	1964
"Cuprous Chloride Light Modulators," F. Sterzer, D. Blattner, and S. Minitzer, <i>Jour. Opt. Soc. Amer.</i> (January) .....	1964
"Dielectric Behavior of Non-Rigid Molecules I. The Simultaneous Relaxation Mechanisms of Diphenyl Ethers and Analogous Compounds," F. K. Fong, <i>Jour. Amer. Chem. Soc.</i> (January) .....	1964
"Effect of Ion Engine Exhaust on Telemetry Systems," P. Parzen, <i>Trans. IEEE PTGNS</i> (January) .....	1964
"Energy Distribution of Ions Formed in the R-F Spark Source," J. R. Woolston and R. E. Honig, <i>Rev. Sci. Instr.</i> (January) .....	1964
"Engineer's Notebook #70—Power Tube Equations," R. A. Henderson, <i>Electronic Industries</i> (January) .....	1964
"Field and Angular Dependence of Critical Currents in Nb <sub>3</sub> Sn II," G. D. Cody, G. W. Cullen, and J. P. McEvoy, Jr., <i>Rev. Mod. Phys.</i> , Part 1 (January) .....	1964
"Further Discussion of Aperture-to-Medium Coupling Loss," H. Staras, <i>Proc. IEEE</i> (Correspondence) (January) .....	1964
"Gaseous (HeNe) 'Cascade' Laser," H. J. Gerritsen and P. V. Goedertier, <i>Appl. Phys. Letters</i> (January) .....	1964
"Ge-Si Thermoelectric Power Generator," B. Abeles and R. W. Cohen (Communications), <i>Jour. Appl. Phys.</i> (January) .....	1964
"Impedance Characteristics of an AC MHD Generator," L. J. Kijewski, J. B. Fanucci, and N. Ness, <i>Trans. IEEE PTGED</i> (January) .....	1964
"Measurement of Distortions Due to Vertical Tracking Angle Errors in Sterodisk Systems," J. B. Halter and J. G. Woodward, <i>Jour. Audio Eng. Soc.</i> (January) .....	1964
"On the Narrow Beam Communication System Acquisition Problem," J. S. Greenberg, <i>Trans. IEEE PTGME</i> (January) .....	1964
"Some Properties of a Group of Co-Phased Wave Antennas," B. E. Keiser, <i>Proc. IEEE</i> (Correspondence) (January) .....	1964
"The Stratoscope II Television System," L. E. Flory, W. S. Pike, J. M. Morgan, and L. A. Boyer, <i>Jour. S.M.P.T.E.</i> (January) .....	1964
"Superconductive Memories," R. W. Ahrons and L. L. Burns, <i>Computer Design</i> (January) .....	1964
"Thermal Conductivity of Nb <sub>3</sub> Sn," G. D. Cody and R. W. Cohen, <i>Rev. Mod. Phys.</i> , Part 1 (January) .....	1964
"Unitized Stereophonic Loudspeaker with Acoustically Augmented Separation of the Sound Sources," H. F. Olson, <i>Jour. Aud. Eng. Soc.</i> (January) .....	1964
"Dielectric Behavior of Nonrigid Molecules. II. Intramolecular Interactions and Dielectric Relaxation," F. K. Fong, <i>Jour. Chem. Phys.</i> (January 1) .....	1964

† Report all corrections to *RCA Review*, RCA Laboratories, Princeton, N. J.

"Evidence of Refrigerating Action by Means of Photon Emission in Semiconductor Diodes," G. C. Dousmanis, C. W. Mueller, H. Nelson, and K. G. Petzinger, <i>Phys. Rev.</i> (January 6) . . . . .	1964
"Interaction of Optical and Infrared Radiation with Metastable Hydrogen Atoms," W. Zernik, <i>Phys. Rev.</i> (January 6) . . . . .	1964
"Current and Voltage Saturation in Semiconducting CdS," A. R. Moore, <i>Phys. Rev. Letters</i> (January 13) . . . . .	1964
"Relationship of Electron Spin Resonance and Semiconduction in Phthalocyanines," S. E. Harrison and J. M. Assour, <i>Jour. Chem. Phys.</i> (January 15) . . . . .	1964
"Giant Quantum Oscillations of the Attenuation of Transverse Acoustic Waves in a Longitudinal Magnetic Field in Metals," J. J. Quinn and Coauthors, <i>Phys. Rev. Letters</i> (January 27) . . . . .	1964
"Microwave Surface Impedance of Superconductors of the Second Kind: In-Bi Alloys," M. Cardona, G. Fischer, and B. Rosenblum, <i>Phys. Rev. Letters</i> (January 27) . . . . .	1964
"Ampliphase for Economical Super-Power AM Transmitters," D. R. Musson, <i>Broadcast News</i> (February) . . . . .	1964
"Demodulation of Low-Level Broad-Band Optical Signals with Semiconductors: Part II—Analysis of the Photoconductive Detector," H. S. Sommers, Jr. and W. B. Teutsch, <i>Proc. IEEE</i> (February) . . . . .	1964
"An Evaluation of Photographic Image Quality and Resolving Power," O. H. Schade, Sr., <i>Jour. S.M.P.T.E.</i> (February) . . . . .	1964
"Frequency Dependence of the Resistivity of a Fully Ionized Plasma," D. A. DeWolf, <i>Proc. IEEE</i> (Correspondence) (February) . . . . .	1964
"Helicon-Phonon Interaction in Metals," J. J. Quinn and S. Rodriguez, <i>Bull. Amer. Phys. Soc.</i> (February) . . . . .	1964
"A High Intensity Carbon-Arc Image Furnace and Its Application to Single Crystal Growth of Refractory Oxides," M. Kestigian, G. J. Goldsmith, and M. Hopkins, <i>Jour. Electrochem. Soc.</i> (February) . . . . .	1964
"Majority Gate Networks," S. Amarel, G. Cooke, and R. O. Winder, <i>Trans. IEEE PTGEC</i> (February) . . . . .	1964
"Measurement Errors: Undetected Defects and False Alarms," W. D. Moon, <i>Trans. IEEE PTGA</i> (February) . . . . .	1964
"Modulator Crystals for Lasers," L. A. Murray, <i>Electronic Industries</i> (February) . . . . .	1964
"Precipitation in Large Single Crystals of Pure CdS," A. B. Dreeben, <i>Jour. Electrochem. Soc.</i> (February) . . . . .	1964
"RCA Color Seminar, Part III: Handling the Color TV Signal," J. W. Wentworth, <i>Broadcast News</i> (February) . . . . .	1964
"RCA Color Seminar, Part IV: Microwave Relaying of Color TV Signals," J. B. Bullock, <i>Broadcast News</i> (February) . . . . .	1964
"RCA Color Seminar, Part V: Getting the Color Signal On-the-Air," R. B. Marye and H. E. Small, <i>Broadcast News</i> (February) . . . . .	1964
"Reducing Distortion in Stereo Phonograph Systems, Part I," J. G. Woodward, <i>Audio</i> (February) . . . . .	1964
"Some Effects on Horizontal Radiation Patterns of Sidemounted FM Antennas," M. R. Johns, <i>Broadcast News</i> (February) . . . . .	1964
"Speech Processing Systems," H. F. Olson, <i>IEEE Spectrum</i> (February) . . . . .	1964
"300-Mc Tunnel-Diode Logic Circuits," M. Cooperman, <i>Trans. IEEE PTGEC</i> (February) . . . . .	1964
"Transient Analysis of Transmission Lines with Nonlinear Terminations," C. R. Pendred, <i>Proc. IEEE</i> (Correspondence) (February) . . . . .	1964
"Traveling-Wave-Tube Noise Figures of 1.0 db at S-Band," J. M. Hammer and E. E. Thomas, <i>Proc. IEEE</i> (Correspondence) (February) . . . . .	1964
"Graphs Aid Deflection System Design," K. W. Angel, <i>Electronics</i> (February 7) . . . . .	1964

- "An All-Electronic Method of Tuning Organs and Pianos, Part III," A. M. Seybold, *Audio* (March) ..... 1964
- "Design and Performance of an Electrostatically Focused 5-kw X-Band Traveling-Wave Tube," E. F. Belohoubek, W. W. Siekanowicz, and F. E. Vaccaro, *Trans. IEEE PTGED* (March) ..... 1964
- "Diffusion in GaAs," L. R. Weisberg, *Trans. Metallurgical Soc. AIME* (March) ..... 1964
- "Electromagnetic Properties of Finite Plasmas," M. P. Bachynski and K. A. Graf, *RCA Review* (March) ..... 1964
- "Ellipsometry—A Valuable Tool in Surface Research," K. H. Zaininger and A. G. Revesz, *RCA Review* (March) ..... 1964
- "Evaporated Metallic Contacts to Conducting Cadmium Sulfide Single Crystals," A. M. Goodman, *Jour. Appl. Phys.* (Part 1) (March) ..... 1964
- "The Field-Effect Transistor—an Old Device with New Promise," J. T. Wallmark, *IEEE Spectrum* (March) ..... 1964
- "High-Temperature Heat Capacity of Ferromagnets Having 1st- and 2nd-Neighbor Exchange: Application to EuS," P. J. Wojtowicz, *Jour. Appl. Phys.* (Part 2) (March) ..... 1964
- "Introductory Statistics and Sampling Concepts Applied to Radar Evaluation," R. J. D'Ortenzio, *RCA Review* (March) ..... 1964
- "Magnetization of Superconducting Niobium-Zirconium Alloys," J. P. McEvoy, Jr. and R. F. Decell, *Jour. Appl. Phys.* (Part 2) (March) ..... 1964
- "Microwave Tunnel-Diode Amplifiers with Large Dynamic Range," R. Steinhoff and F. Sterzer, *RCA Review* (March) ..... 1964
- "Monte Carlo Calculation of Noise Transport in a Two-Dimensional Diode," C. P. Wen and Coauthor, *Trans. IEEE PTGED* (March) ..... 1964
- "A Rapid Volumetric Method for Determining Sulfur in Acid-Soluble Sulfides," R. Nitsche and P. Wild, *Helvetica Chimica Acta* (March) ..... 1964
- "Reducing Distortion in Stereo Phonograph Systems," Part II, J. G. Woodward, *Audio* (March) ..... 1964
- "A Simplified Routine Method for X-Ray Absorption Edge Spectrometric Analysis," E. P. Bertin, R. J. Longobucco, and R. J. Carver, *Anal. Chem.* (March) ..... 1964
- "Stress Effects in Evaporated Permalloy Films," H. L. Pinch and A. A. Pinto, *Jour. Appl. Phys.* (Part 2) (March) ..... 1964
- "A Study of Noise in Television Camera Preamplifiers," K. Sadashige, *Jour. S.M.P.T.E.* (March) ..... 1964
- "Techniques for Digital Communication via Satellites," F. Assadourian and E. M. Bradburd, *RCA Review* (March) ..... 1964
- "Classical Impulse Approximation for Inelastic Electron-Atom Collisions," R. C. Stabler, *Phys. Rev.* (March 2) ..... 1964
- "Helicon-Phonon Interaction in Metals," J. J. Quinn and Coauthor, *Phys. Rev.* (March 16) ..... 1964
- "Optical Properties and Band Structure of Group IV-VI and Group V Materials," M. Cardona and D. L. Greenaway, *Phys. Rev.* (March 16) ..... 1964
- "Thermal Conductivity and Seebeck Coefficient of InP," I. Kudman and E. F. Steigmeier, *Phys. Rev.* (March 16) ..... 1964
- "Transport Properties of Organic Semiconductors," L. Friedman, *Phys. Rev.* (March 16) ..... 1964
- "A New Look for the Old Telegraph," R. K. Andres and L. P. Correard, *Electronics* (March 23) ..... 1964

## AUTHORS

MORREL P. BACHYNSKI (see *RCA REVIEW*, Vol. XXV, No. 1, March 1964, p. 152.)



MANUEL CARDONA received the MS in Physics from the University of Barcelona in 1955. He was a lecturer in electronics at the University of Madrid from 1955 to 1956 and received the DSc in Physics from the University of Madrid in 1958. He attended Harvard University, receiving the MS degree in 1957 and PhD degree in Applied Physics in 1959. He has been a member of the technical staff at RCA Laboratories since 1959, from 1959 to 1961 at the Zurich Laboratories and since 1961 at the David Sarnoff Research Center in Princeton. Dr. Cardona has studied the transport and optical properties of a large number of semiconductors and has provided substantial contributions to the knowledge of the band structure in these materials. He has recently been studying the properties of solid-state plasmas in a magnetic field and the microwave properties of hard superconductors. Dr. Cardona is a member of the American Physical Society.

GILLES G. CLOUTIER received a B.A. degree from Laval University in 1949 and a B.A. Sc. degree (Physics) in 1953. He then joined C.A.R.D.E. (DRB) where he engaged in research on physical properties of rocket propellants. In the fall of 1954, he joined the Eaton Electronics Research Laboratory, McGill University, where he received an M.Sc. (Physics) degree in 1956 for his research in the field of microwave optics and antennas. In 1959 he received the PhD degree from McGill for his work in the field of mass spectrometry. After graduation, Dr. Cloutier joined the Microwave and Plasma Physics Laboratory of the RCA Victor Co., where he has contributed to several research programmes on microwave interaction with plasmas and on ionic propulsion. In September 1963, Dr. Cloutier became Associate Professor in the Department of Physics at the University of Montreal. He is responsible for the new laboratory which is being set up for research in the field of plasma physics.



Dr. Cloutier is a member of the Canadian Association of Physicists, the Institute of Electrical and Electronics Engineers, the American Physical Society, the American Institute of Aeronautics and Astronautics and the Society of Sigma Xi. Dr. Cloutier is also a member of the Associate Committee of Space Research of the National Research Council.



ALBRECHT G. FISCHER received the Ph.D. degree in experimental physics from the University of Giessen, Germany, in 1957. After one year with the Lamp Division of General Electric Company, he joined RCA Laboratories in 1959. He has worked on various aspects of electroluminescence in powders and single crystals of II-VI and III-V compounds and is now mainly engaged in research on injection electroluminescence in II-VI crystals. Dr. Fischer is a member of the Electrochemical Society, the German Physical Society, Sigma Xi, and the Academy of Model Aeronautics.

FRANCIS K. FONG received the degrees of A.B. and Ph.D. (physical chemistry) from Princeton University in 1959 and 1962, respectively. From 1962 to 1963, he worked as a Research Associate in Princeton University on an extension of his thesis which dealt with microwave absorption in liquids and dielectric relaxation of polar molecules. In 1963, he joined the technical staff of the RCA Laboratories where he has been engaged in research on divalent rare earth ions in alkaline earth halides as laser materials, the solid state redox reactions of the rare earths, the color centers in alkaline earth halides, and the crystal growth of these materials. Dr. Fong is a member of Sigma Si, the American Chemical Society and the American Physical Society.





E. G. FORTIN received a B.A. degree in Chemistry from St. Anselm's College in 1954. In 1959, after his tour in the Army, he joined the Memory Products Activity of Electronic Components and Devices in Needham, Mass. He worked for four years on the development of square loop materials and particularly on temperature stable materials. He is presently working on application and development of ferrite memory cores and other square-loop devices. Mr. Fortin is currently a part-time faculty member of Lincoln College, Northeastern University.

J. D. KIESLING received the BEE degree in 1953 and the MEE degree in 1958 from Polytechnic Institute of Brooklyn. In 1953, he joined the Brookhaven Laboratory where he helped design a 50 MEV proton linear accelerator. He was also co-inventor of a high-energy particle separator. Mr. Kiesling joined ACF Industries as a research consultant in 1959, specializing in the design of microwave circuits. In 1960, he joined the Astro-Electronics Division of RCA as a systems engineer working on communications problems connected with space programs. He was assigned to Project Relay as project engineer for wideband television repeaters. He is presently Project Leader for the communications subsystem for Project Relay.



H. P. LEMAIRE received the Ph.D. degree in Physical Chemistry from Purdue University in 1950. His previous studies were conducted at the University of Manitoba, where he received the B.Sc. and M.Sc. degrees. After graduation he was appointed to the staff of St. Michael's College in Vermont where he taught chemistry. Dr. Lemaire came to the Memory Products Activity of Electronic Components and Devices in 1959. He is presently in charge of advanced development, having general supervision of the development of ferrites for new applications, high-temperature ferrites, and microferrites.

HOWARD LESSOFF received the B.S. degree in 1953 and the M.S. degree in 1957, both in Chemistry, from Northeastern University. He was a chemist with the Quartermaster Corps working on petroleum quality control from 1953 to 1955. From 1955 to 1957, he was a Research and Teaching Associate at Northeastern University, where he did fluoro carbon research. From 1956 to 1960, he was an instructor in the Lincoln Institute at Northeastern University. He joined RCA Electronic Components and Devices in the Needham facility in 1957, working on ceramic and tantalitic capacitors, thin films, low-loss ferrites, and thermoelectric materials. He spent a year at Bell Telephone Laboratories from 1960 to 1961, working on ferrite switching materials, and returned to RCA in 1961. He is presently engaged in ferrite material development and is Project Leader of a group working on magnetic thin sheet memory. Mr. Lessoff is a member of the American Chemical Society and the Electrochemical Society.



FREDERICK H. NICOLL received the B.Sc. degree in Physics from Saskatchewan University, Canada, in 1929 and the M.Sc. degree in 1931. He held an 1851 Exhibition Scholarship to Cambridge University, England for three years research and received the Ph.D. degree from that university in 1934. He was a research physicist with Electric and Musical Industries, Ltd. in London from 1934 to 1939. From 1939 to 1941 he was with the RCA Victor Division at Camden, N. J. as a research engineer. Since 1942 he has been with the RCA Laboratories in Princeton, N. J., engaged in research on cathode-ray tubes and electron optics and, more recently, photoconduction, electroluminescence, and solid-state devices. In 1963-64 Dr. Nicoll spent a year of study at the Cavendish Laboratory, Cambridge, England, sponsored by RCA Laboratories.

Dr. Nicoll is a Fellow of the Institute of Electrical and Electronics Engineers and a Member of the American Physical Society and of Sigma Xi.

C. C. WANG received the B.S. in Chemical Engineering at the National Taiwan University, Taiwan, China, in 1955. From 1956 to 1958 he was an assistant engineer in the Taiwan Alkali Company. He received the M.S. in Chemical Engineering from the Kansas State University in 1959, and Ph.D. in Physical Chemistry from the Colorado State University in 1962. From 1962 to 1963 he was a post-doctoral research associate in the high temperature chemistry group of the University of Kansas. His research has been in the fields of inorganic synthesis, crystal growth, thermodynamics, phase equilibrium studies, x-ray crystallography, and mass spectrometry of high temperature materials. He joined RCA Laboratories, Princeton, in 1963 and has been doing research work on the synthesis and characterization of III-V compounds, as well as ferromagnetic substance.

Dr. Wang is a member of the American Chemical Society, Electrochemical Society, Sigma Xi, Sigma Pi Sigma, and Phi Lambda Upsilon.





ROSCOE C. WILLIAMS graduated from the University of Manitoba in 1951 with an Honours Bachelor of Science in both Physics and Mathematics. He received the Master's degree in Theoretical Physics from McGill University in 1953, and the Ph.D. in Experimental Physics at the University of Manitoba in 1958. He joined Bell Telephone Laboratories in 1956, where he worked on magnetostrictive delay lines. Since joining RCA Laboratories in 1958, he has been engaged in cyclotron resonance studies in semiconductors and research in lasers and space-charge-limited emission. Dr. Williams was awarded

the I.R.E. Best Paper Award of 1959 for his paper entitled, "Theory of Magnetostrictive Delay Lines for Pulse and Continuous Wave Transmission." Dr. Williams was a Guest Lecturer in the Electrical Engineering Department of Princeton University in 1963.

N. E. WOLFF received the B.Sc. degree from the Institute of Technology, Munich, Germany in 1948 and the M.A. and Ph.D. degrees in chemistry from Princeton University in 1951 and 1952. During his graduate work, he was a part time teacher at Princeton University and became a full member of the faculty upon receiving his doctorate. From 1953 through 1959, he was associated with the Organic Chemicals Department, E. I. du Pont de Nemours and Company, Inc., Wilmington, Delaware. In 1959, Dr. Wolff joined the staff of the David Sarnoff Research Center, RCA Laboratories, where he was engaged in conducting research on the electronic behavior of organic materials, particularly in the field of organic photoconductors and laser materials. In the fall of 1963, he transferred to the newly established Process Research and Development Laboratory where he is in charge of Materials Processing Research. In his new capacity, he is concerned with materials problems related to new manufacturing processes.



Dr. Wolff is a member of the American Physical Society, the American Chemical Society, the American Association for the Advancement of Science, and the Society of Sigma Xi.









